UNIVERSITY OF CALIFORNIA SAN DIEGO

Spatio-temporal resolution of regional cardiac function assessment with four-dimensional computed tomography

A dissertation submitted in partial satisfaction of the
requirements for the degree
Doctor of Philosophy

in

Engineering Sciences (Mechanical Engineering)

by

Ashish Manohar

Committee in charge:

Professor Elliot R. McVeigh, Chair
Professor Tania Morimoto, Co-Chair
Professor Francisco Contijoch
Professor Juan Carlos del Alamo
Professor Andrew M. Kahn
Professor Stephanie Lindsey

2022

The dissertation of Ashish Manohar is approved, and it is acceptable in quality and form for publication on microfilm and electronically.

University of California San Diego

2022

DEDICATION

To my parents, Dr. S Manohar and Aparna Manohar

EPIGRAPH

You can lie to yourself, but you can't lie to The Council

–The Council

TABLE OF CONTENTS

LIST OF FIGURES

LIST OF TABLES

ACKNOWLEDGEMENTS

I was very fortunate for being supported in many different capacities by the numerous people I have had the privilege of encountering during my doctoral studies; without their support, this work would not have been possible.

First and foremost, I'd like to thank my advisor Dr. Elliot McVeigh for arguably being the best PhD advisor I could've asked for. I remember the very first interaction with him via email, where he addressed Juan Carlos and I as "Gents", and I knew from that very moment on that I would be extremely lucky if I got a chance to work with him. Even more important than my growth and development as a scientist, I think my key takeaways from working with Elliot was my growth and development as an individual; he has always encouraged us to be passionate about our work but without even for a second forgetting to enjoy life while doing so. I am truly grateful for having this opportunity of completing my doctoral studies with him, and no matter what I decide to pursue further in life, I will always strive to reach his perfect balance of fun and work.

My path into academia all began with Juan Carlos. He provided me with my very first opportunity of getting acquainted with academic research and was also responsible for introducing me to Elliot, so a big thank you! Since then, we have discussed a whole lot of tennis together and I would silently like to think that I converted him into a Rafa fan from a Federer fan! A big shout out to Lorenzo as well, for being an awesome office mate and patiently teaching me the A-B-C-D of writing code.

I have been fortunate to have excellent mentors along the way. I am very grateful to have had the opportunity to work with Jed Pack. The weekly Wednesday morning meetings have been such a tremendous source of knowledge for everything from CT physics to AI and segmentation

routines. I would also like to thank Maria Ledesma-Carbayo for teaching me the basics of strain estimation from MR tagged data, and not to forget the wonderful sailing experience we had together! Lastly, I'd like to thank Mads Kronborg, Anders Sommer, Bjarne Nørgaard, and Jens Nielsen for the gold-mine CRT data and teaching me so much about the clinical relevance of the technologies I helped develop.

The five years I have spent at the Cardiovascular Imaging Lab (CViL) was such an amazing experience thanks to my wonderful lab members including Gabby, Davis, Andrew, Zhennong, Brendan, James, Kyle, Lauren, Katherine, and Aditi. Also special shout out to my friends from SME including Brato, Ernesto, Shun, Cat, Marissa, Maria, Ricardo, Achal, Mickey, and Miriam.

Grad school would not have been the same if it wasn't for the wonderful memories and experiences I shared with so many people along the way. The Council (Dan and Lennart) for being the coolest council on earth, and making so many great travel memories along with the wonderful Katy and Ian. Ritvik, and Erol for being dope housemates and nerding out on game theory while trying to explain human relationships! The extraordinary Pergofam including Nima, Kyle, April, Austin, and Co. Na, Henry, and Paula for being the coolest fellow brewery explorers. Vicky, Nate, Suganth, and Margarita for the awesome board game nights. Erica, Marty, Chris, Dayna, and Vish for the many super fun bike rides, and Eddie for being my very first friend in San Diego! Also a big shout out to my friends back home in India: Dheeraj, Kishan, Naveen, Shivani, and Anush.

Lastly, I would like to thank my family. My brother and his wife, together with their adorable puppy for being such tremendous pillars of support for me in the United States. I am eternally indebted to my mom and dad for all the sacrifices they've made to help me advance my

career. They've showered me with nothing but love and have been the most supportive parents I could've asked for!

Chapter 2 is a reprint of the material: **Ashish Manohar**, Gabrielle M. Colvert, Andrew J. Schluchter, Francisco Contijoch, and Elliot R. McVeigh. "Anthropomorphic left ventricular mesh phantom: a framework to investigate the accuracy of SQUEEZ using Coherent Point Drift for the detection of regional wall motion abnormalities" *Journal of Medical Imaging* **6**, 2019. The dissertation author is the primary author.

Chapter 3 is a reprint of the material: **Ashish Manohar**, Jed D. Pack, Andrew J. Schluchter, and Elliot R. McVeigh. "Four-dimensional computed tomography of the left ventricle, Part II: Estimation of mechanical activation times" *Medical Physics* **49**, 2022. The dissertation author is the primary author.

Chapter 4 is a reprint of the material: **Ashish Manohar**, Gabrielle M. Colvert, James Yang, Zhennong Chen, Maria J. Ledesma-Carbayo, Mads Brix Kronborg, Anders Sommer, Bjarne L. Nørgaard, Jens Cosedis Nielsen, and Elliot R. McVeigh. "Prediction of CRT response using a lead placement score derived from 4DCT" *medRxiv*, DOI:10.1101/2022.03.23.22272846, 2022. The dissertation author is the primary author.

Chapter 5 is a reprint of the material: **Ashish Manohar**, James Yang, Jed D. Pack, and Elliot R. McVeigh. "Estimation of left ventricular mechanical activation times from motion-corrected cardiac 4DCT images" *bioRxiv*, DOI:10.1101/2022.04.12.488106, 2022. The dissertation author is the primary author.

VITA

2015	Bachelor of Engineering in Mechanical Engineering, R.V. College of Engineering, Bangalore, India
2017	Master of Science in Mechanical Engineering, University of California San Diego
2022	Doctor of Philosophy in Mechanical Engineering, University of California San Diego

PUBLICATIONS

Ashish Manohar, Gabrielle M. Colvert, Andrew J. Schluchter, Francisco Contijoch, and Elliot R. McVeigh. "LV systolic point-cloud model to quantify accuracy of CT derived regional strain", *Medical Imaging 2019: Image-Guided Procedures, Robotic Interventions, and Modeling*, February 2019, San Diego, USA.

Gabrielle M. Colvert, **Ashish Manohar**, Brendan Colvert, Andrew J. Schluchter, Francisco Contijoch, and Elliot R. McVeigh. "Novel measurement of LV twist using 4DCT: quantifying accuracy as a function of image noise", *Medical Imaging 2019: Biomedical Applications in Molecular, Structural, and Functional Imaging*, February 2019, San Diego, USA.

Ashish Manohar, Lorenzo Rossini, Gabrielle M. Colvert, Davis Vigneault, Francisco Contijoch, Marcus Chen, Juan Carlos del Alamo, and Elliot R. McVeigh. "Regional dynamics of fractal dimension of the left ventricular endocardium from cine computed tomography images", *Journal of Medical Imaging*, 2019.

Ashish Manohar, Gabrielle M. Colvert, Andrew J. Schluchter, Francisco Contijoch, and Elliot R. McVeigh. "Anthropomorphic left ventricular mesh phantom: a framework to investigate the accuracy of SQUEEZ using Coherent Point Drift for the detection of regional wall motion abnormalities", *Journal of Medical Imaging*, 2019.

Gabrielle M. Colvert, **Ashish Manohar**, Francisco Contijoch, James Yang, Jeremy Glynn, Philipp Blanke, Jonathan Leipsic, and Elliot R. McVeigh. "Novel 4DCT method to measure regional left ventricular endocardial shortening before and after transcatheter mitral valve implantation", *Structural Heart*, 2021.

Jed D. Pack, **Ashish Manohar**, Sathish Ramani, Bernhard Claus, Zhye Yin, Francisco Contijoch, Andrew J. Schluchter, and Elliot R. McVeigh. "Four-dimensional computed tomography of the left ventricle, part I: motion artifact reduction", *Medical Physics*, 2021.

Ashish Manohar, Jed D. Pack, Andrew J. Schluchter, and Elliot R. McVeigh. "Four-dimensional computed tomography of the left ventricle, part II: estimation of mechanical activation times", *Medical Physics*, 2021.

Ashish Manohar, Gabrielle M. Colvert, James Yang, Zhennong Chen, Maria J. Ledesma-Carbayo, Mads Brix Kronborg, Anders Sommer, Bjarne L. Nørgaard, Jens Cosedis Nielsen, and Elliot R. McVeigh. "Prediction of CRT response using a lead placement score derived from 4DCT" *medRxiv*, DOI:10.1101/2022.03.23.22272846, 2022.

Ashish Manohar, James Yang, Jed D. Pack, and Elliot R. McVeigh. "Estimation of left ventricular mechanical activation times from motion-corrected cardiac 4DCT images" *bioRxiv*, DOI:10.1101/2022.04.12.488106, 2022.

ABSTRACT OF THE DISSERTATION

Spatio-temporal resolution of regional cardiac function assessment with four-dimensional computed tomography

by

Ashish Manohar

Doctor of Philosophy in Engineering Sciences (Mechanical Engineering)

University of California San Diego, 2022

Professor Elliot R. McVeigh, Chair
Professor Tania Morimoto, Co-Chair

Assessment of regional cardiac function has implications in the diagnosis and management of cardiac diseases such as myocardial ischemia, heart failure, dyssynchrony, and cardiotoxicity. Over the past 30 years, significant effort has been focused on developing methods for estimating regional cardiac function; however, there remains an urgent unmet clinical need for a method that is easily available, accurate, reproducible, and operator independent. Modern four-dimensional computed tomography (4DCT) imaging systems can acquire highly detailed full 3D images of the heart across the entire cardiac cycle from a single table position and within a single heartbeat;

no other non-invasive cardiac imaging modality comes close to this capability. Additionally, the images are now routinely acquired with low patient exposure to ionizing radiation. While 4DCT is proving to be a promising modality, its spatio-temporal resolution in the context of regional cardiac function assessment has neither been previously explored nor well understood. This dissertation aims to investigate the spatio-temporal capabilities of 4DCT and develop methods that leverage the high fidelity of 4DCT for the accurate and reproducible estimation of regional cardiac function. First, we develop anthropomorphically accurate phantoms of the human left ventricle (LV) and use these phantoms to develop and optimize methods for the high spatial-resolution assessment of regional LV function. Second, we use the developed phantoms to understand and improve the temporal resolution of 4DCT; higher temporal resolution permits the accurate and reproducible estimation of mechanical activation times of LV wall motion which have previously been shown to be a strong predictor of patient response to cardiac resynchronization therapy (CRT). Lastly, we apply the developed methods to subject cohorts with routinely acquired clinical 4DCT scans and investigate their potential effect on the planning and management of cardiac diseases, using CRT as an example. In conclusion, this dissertation has broadened our understanding of the spatio-temporal resolution of 4DCT and potentially fulfils the unmet clinical need for an accurate and reproducible method to estimate regional cardiac function.

Chapter 1

Introduction

Significant effort has been focused on the development of robust non-invasive imaging techniques for the assessment of regional cardiac function, which has implications in the diagnosis and management of diseases such as myocardial ischemia [1, 2], heart failure [3], cardiotoxicity [4], and dyssynchrony [5–7]. Global function metrics such as left ventricular ejection fraction (LVEF) and global longitudinal strain (GLS) have prognostic value in patients with heart disease [8]; however, global function metrics are less sensitive to local changes in heart function and are typically only detected in advanced disease stages, with localized dysfunction often preceding global dysfunction. This dissertation investigates the potential clinical utility of four-dimensional computed tomography (4DCT) for the accurate and reproducible estimation of regional cardiac function.

The most prevalent clinical modality used for assessing both regional and global cardiac function is two-dimensional (2D) echocardiography, a method that often relies on an observer's visual assessment of myocardial contractility; however, concerns with the inter- and intra-observer variability together with inter-vendor differences [9–11] have limited its widespread clinical appli-

cation for the quantitative evaluation of cardiac deformation parameters. Despite the advent of real-time three-dimensional (3D) echocardiography, its limited spatial resolution and long acquisition times (multiple heartbeats required to produce a 3D model of the heart) have hindered the reproducible detection of endocardial and epicardial borders and has led to poor overall adoption of this method.

Cardiac magnetic resonance (CMR) is a proven modality for the assessment of regional cardiac function [12]. In particular, CMR tagging is the gold-standard modality for the quantitative assessment of regional myocardial function [13–15]. Cine CMR [16, 17] and cine displacement encoding with stimulated echoes (DENSE) [18] have also been used to successfully quantify regional myocardial function. Unfortunately, the long acquisition times spanning multiple heartbeats, limited spatial resolution in the slice direction, and the requirement of highly-skilled image acquisition and image analysis personnel are some of the factors that have impeded the adoption of CMR techniques for the routine clinical assessment of regional cardiac function.

Advances in 4DCT have permitted the acquisition of 3D images of the full heart volume spanning the entire cardiac cycle within a single heartbeat and from a single table position; this is a tremendous advantage over echocardiography and CMR especially when imaging patients with arrhythmia/irregular heartbeats. Additionally, the 4DCT cardiac images have unmatched spatial resolution [19–21], delineating the rich endocardial texture of the heart [22]. The drawback with 4DCT is patient exposure to ionizing radiation; however, recent technological developments have permitted the acquisition of an entire functional series of 4D images of the heart across the cardiac cycle with radiation doses in the range of [0.5, 4] mSv, which is considered to be low dose [23]. In the United States, the average annual exposure to natural sources of radiation is 3 mSv (range 1-10 mSv depending on geographical location). Since there has been no established geographic

correlation with cancer risk, the consensus adopted at the Summit on Management of Radiation Dose (Bethesda, Maryland, 24-25 February 2011) was that long-term risk of radiation dose from CT can be considered negligible if the radiation dose is limited to less than the background radiation [24]. In addition, the radiation dose from CT will further continue to be lowered with the advent of photon-counting detectors, more powerful x-ray tube generators at low peak kilovoltage (kVp), and deep learning for image reconstruction, image denoising, and artifact reduction.

4DCT is not routinely used for regional cardiac function assessment. Additionally, the spatio-temporal resolution of 4DCT in the context of regional cardiac function assessment has neither been previously explored nor well understood. This thesis aims to bridge that gap in knowledge and develop tools that leverage the high fidelity of 4DCT for the accurate and reproducible assessment of regional cardiac function. The ability to derive accurate and reproducible estimates of regional cardiac function easily and in a wide group of patients would likely drive a paradigm shift in quantitative functional cardiac imaging.

1.1 Spatial resolution of regional cardiac function assessment

4DCT systems offer 3D full heart volume images across the cardiac cycle with very high spatial resolution [19–21]; the resolution can be easily appreciated by visualizing a simple surface rendering of the left ventricular (LV) endocardium as shown in Fig. 1.1. The LV endocardium is rich in texture comprising the trabeculae carneae and the papillary muscles; these high-frequency spatial features can be used as fiducial markers for tracking the contraction of local regions of the endocardium. Currently, the American Heart Association (AHA) 17-segment model [25] is the standard model for quantifying regional LV function; however, with the superior spatial

resolution of 4DCT, we sought to develop tools that facilitate the estimation of regional LV function at a higher resolution than the AHA 17-segment model; we need a model that more closely corresponded with the true resolution yielded by 4DCT (1 x 1 x 1 mm^3). These higher resolution estimates of regional LV function could be more sensitive to subtle changes in functional states of the LV (eg. between pre- and post-therapy), and could also be earlier detectors of local LV dysfunction.

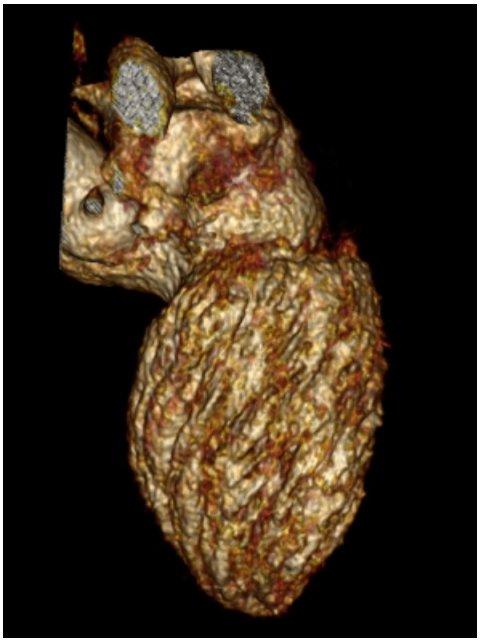

Figure 1.1: 3D rendering of the LV endocardial surface. The lateral wall is in view, depicting the detailed endocardial texture. LV: left ventricle

1.2 Temporal resolution of regional cardiac function assessment

The temporal resolution of 4DCT is complex; the temporal resolution does not increase by reconstructing a large number of time frames in a 4D series. It actually depends on the rotation speed of the gantry and the position of the gantry with respect to the direction of motion of the object being imaged [21]. 4DCT images are not simple temporal averages of the

object within the acquisition window; the motion artifacts seen in 4DCT images are actually a mathematical image reconstruction problem. Spatial frequencies within a radial sample in the Fourier domain of the object are acquired by sub-millisecond x-rays associated with a particular gantry view-angle (Fourier slice theorem); therefore, these radial samples of spatial frequencies have excellent temporal resolution. Different spatial frequencies are sampled radially at different view-angles thereby completing the full Fourier representation of the object; thus, these radial samples are merely phase shifted with respect to one another (the magnitude remains unchanged with respect to the original object). Therefore, motion correction can be achieved by accurately modeling the phase shifts.

High temporal resolution is important for cardiac applications such as the assessment of timing of LV mechanics and dyssynchrony [5–7]. The estimates of LV mechanical activation times have been shown to have a strong correlation with cardiac resynchronization therapy (CRT) response [16, 26, 27]. Therefore, the accurate and reproducible estimation of timing of mechanical events of interest of the LV may have significant implications in patient selection for CRT.

The temporal resolution of 4DCT is ∼65 ms for dual-source scanners and ∼140 ms for single-source scanners; thus, motion correction is especially important for single-source scanners. While dual-source scanners (e.g., Somatom Force, Siemens Healthcare) have higher temporal resolution, they have limited detector coverage in the z-axis direction (< 60 mm); therefore, the entire inferior-superior extent of the heart can be imaged only in helical mode, or with two table positions in "step and shoot" mode. This may yield step-artifacts due to beat-to-beat irregularities during the acquisition, especially in patients with arrhythmia; thus, rendering the images unanalyzable for mechanical dyssynchrony analysis. Therefore, wide detector scanners (e.g., Revolution CT, GE Healthcare with 256 detector-rows or Aquilion ONE, Canon Medi-

cal Systems with 320 detector-rows) with full heart coverage from a single table position (160 mm z-axis coverage) may be better suited for this application, especially with the significant advancements made in the field of motion correction [28, 29].

1.3 Outline of the dissertation

The dissertation is structured as follows:

- Chapter 2 investigates the spatial resolution limits of a 4DCT-derived regional endocardial strain estimation method for the assessment of regional cardiac function. The chapter describes the development of an anthropomorphically accurate LV phantom that served as ground-truth for strain estimation. Using the phantom, guidance was obtained on the sizes of wall motion abnormalities that can be accurately detected with 4DCT: wall motion abnormalities greater than 19 mm in diameter were detected with high accuracy to within ±5% error, with the threshold for the detection of a dysfunctional region lying between 14 and 19 mm.

- Chapter 3 investigates the temporal resolution of 4DCT for the estimation of LV mechanical activation times. Activation times of LV wall motion have previously been shown to be a strong predictor of response to CRT. An anthropomorphically accurate dyssynchronous LV phantom was developed. The phantom was used as ground-truth to understand motion artifacts in 4DCT images as well as their effects on estimating timing of LV mechanical activation. A newly developed cardiac motion correction algorithm called ResyncCT was used to produce motion artifact-free images. With motion correction, 4DCT yielded estimates of LV mechanical activation with significantly improved accuracy and precision over

the estimates derived from the motion-corrupted images. The results from this chapter highlight the potential utility of 4DCT in estimating activation times of LV wall motion for CRT planning and management.

- Chapter 4 employs the tools developed in chapters 2 and 3 with the goal of defining a patient-specific metric that predicts the probability of a patient responding to CRT. Despite CRT being a proven treatment for heart failure, 30-50% of patients who undergo CRT do not respond to the treatment; thus, more accurate patient selection for CRT remains an urgent unmet clinical need. Eighty-two subjects, each with 4DCT scans acquired both before and 6-months after CRT implantation, were used in this study. Eight features of LV mechanics, which were derived from the pre-CRT 4DCT scans of the subjects, were used to train a model using a support vector machine. The model called the *lead placement score* yields a patient-specific metric that is correlated with the probability of a patient responding to CRT. The *lead placement score* effectively reclassified the 82 subjects into three groups: low-probability of responding to CRT, high-probability of responding to CRT, and a probability of responding to CRT that was unchanged from the pretest probability. The encouraging results reported in this chapter highlight the potential utility of 4DCT in patient selection for CRT.

- Chapter 5 investigates the clinical utility of estimating mechanical activation times of the LV from motion-corrected cardiac 4DCT images. Chapter 3 describes and validates the newly developed cardiac motion correction algorithm called ResyncCT using controlled phantom experiments; this chapter investigates its applicability to routinely acquired clinical cardiac 4DCT images and quantifies its effect on the estimates of LV mechanical activation times. Twenty-four subjects with full heart volume full cardiac cycle images were used and the

images were processed with ResyncCT to yield motion corrected images. The effect of ResyncCT on the estimation of LV mechanical activation times was profound; ResyncCT could potentially reclassify 96% of the subjects used in this study based on their probabilities of responding to CRT. Additionally, the differences in activation times between the motion-corrected ResyncCT images and the motion-corrupted images were heterogeneous and subject specific. The results reported in this study highlight the potential utility of ResyncCT in estimating timing of mechanical events of interest of the LV for CRT planning.

- Chapter 6 summarizes the results of this dissertation in the broader context of 4DCT and its potential utility in advancing cardiac imaging for the better management of disease.

1.4 References

1. Amundsen, B. H., Helle-Valle, T., Edvardsen, T., Torp, H., Crosby, J., Lyseggen, E., Støylen, A., Ihlen, H., Lima, J. A., Smiseth, O. A. & Slørdahl, S. A. Noninvasive Myocardial Strain Measurement by Speckle Tracking Echocardiography. *Journal of the American College of Cardiology* **47,** 789–793. ISSN: 07351097. http://dx.doi.org/10.1016/j.jacc.2005.10.040%20https://linkinghub.elsevier.com/retrieve/pii/S0735109705027506 (Feb. 2006).

2. Moore, C., McVeigh, E. & Zerhouni, E. Noninvasive Measurement of Three-Dimensional Myocardial Deformation with Tagged Magnetic Resonance Imaging During Graded Local Ischemia. *Journal of Cardiovascular Magnetic Resonance* **1,** 207–222. ISSN: 1097-6647. arXiv: NIHMS150003. http://www.informaworld.com/openurl?genre=article%7B%5C&%7Ddoi=10.3109/10976649909088333%7B%5C&%7Dmagic=crossref%7B%5C%%7D7C%7B%5C%%7D7CD404A21C5BB053405B1A640AFFD44AE3 (July 1999).

3. Cho, G.-Y., Marwick, T. H., Kim, H.-S., Kim, M.-K., Hong, K.-S. & Oh, D.-J. Global 2-Dimensional Strain as a New Prognosticator in Patients With Heart Failure. *Journal of the American College of Cardiology* **54,** 618–624. ISSN: 07351097. http://dx.doi.org/10.1016/j.jacc.2009.04.061%20https://linkinghub.elsevier.com/retrieve/pii/S0735109709017422 (Aug. 2009).

4. Thavendiranathan, P., Poulin, F., Lim, K.-D., Plana, J. C., Woo, A. & Marwick, T. H. Use of Myocardial Strain Imaging by Echocardiography for the Early Detection of Cardiotoxicity in Patients During and After Cancer Chemotherapy. *Journal of the American College of Cardiology* **63,** 2751–2768. ISSN: 07351097. http://dx.doi.org/10.1016/j.jacc.2014.

01.073%20https://linkinghub.elsevier.com/retrieve/pii/S073510971401660X (July 2014).

5. McVeigh, E. R., Prinzen, F. W., Wyman, B. T., Tsitlik, J. E., Halperin, H. R. & Hunter, W. C. Imaging asynchronous mechanical activation of the paced heart with tagged MRI. *Magnetic Resonance in Medicine* **39,** 507–513. ISSN: 07403194. http://doi.wiley.com/10.1002/mrm.1910390402 (Apr. 1998).

6. Wyman, B. T., Hunter, W. C., Prinzen, F. W. & McVeigh, E. R. Mapping propagation of mechanical activation in the paced heart with MRI tagging. *American Journal of Physiology-Heart and Circulatory Physiology* **276,** H881–H891. ISSN: 0363-6135. https://www.physiology.org/doi/10.1152/ajpheart.1999.276.3.H881 (Mar. 1999).

7. Wyman, B. T., Hunter, W. C., Prinzen, F. W., Faris, O. P. & McVeigh, E. R. Effects of single- and biventricular pacing on temporal and spatial dynamics of ventricular contraction. *American Journal of Physiology-Heart and Circulatory Physiology* **282,** H372–H379. ISSN: 0363-6135. https://www.physiology.org/doi/10.1152/ajpheart.2002.282.1.H372 (Jan. 2002).

8. Kalam, K., Otahal, P. & Marwick, T. H. Prognostic implications of global LV dysfunction: a systematic review and meta-analysis of global longitudinal strain and ejection fraction. *Heart* **100,** 1673–1680. ISSN: 1355-6037. http://heart.bmj.com/lookup/doi/10.1136/heartjnl-2014-305538%20https://heart.bmj.com/lookup/doi/10.1136/heartjnl-2014-305538 (Nov. 2014).

9. Mirea, O., Pagourelias, E. D., Duchenne, J., Bogaert, J., Thomas, J. D., Badano, L. P., Voigt, J.-U., Badano, L. P., Thomas, J. D., Hamilton, J., Pedri, S., Lysyansky, P., Hansen, G., Ito, Y., Chono, T., Vogel, J., Prater, D., Park, S., Lee, J. Y., Houle, H., Georgescu, B., Baumann, R., Mumm, B., Abe, Y. & Gorissen, W. Variability and Reproducibility of Segmental Longitudinal Strain Measurement. *JACC: Cardiovascular Imaging* **11,** 15–24. ISSN: 1936878X. https://linkinghub.elsevier.com/retrieve/pii/S1936878X17303601 (Jan. 2018).

10. Mirea, O., Pagourelias, E. D., Duchenne, J., Bogaert, J., Thomas, J. D., Badano, L. P., Voigt, J.-U., Badano, L. P., Thomas, J. D., Hamilton, J., Pedri, S., Lysyansky, P., Hansen, G., Ito, Y., Chono, T., Vogel, J., Prater, D., Park, S., Lee, J. Y., Houle, H., Georgescu, B., Baumann, R., Mumm, B., Abe, Y. & Gorissen, W. Intervendor Differences in the Accuracy of Detecting Regional Functional Abnormalities. *JACC: Cardiovascular Imaging* **11,** 25–34. ISSN: 1936878X. https://linkinghub.elsevier.com/retrieve/pii/S1936878X17303637 (Jan. 2018).

11. Badano, L. P. & Muraru, D. The Good, the Bad, and the Ugly of Using Left Ventricular Longitudinal Myocardial Deformation by Speckle-Tracking Echocardiography to Assess Patients After an Acute Myocardial Infarction. *Circulation: Cardiovascular Imaging* **10,** 1–3. ISSN: 1941-9651. https://www.ahajournals.org/doi/10.1161/CIRCIMAGING.117.006693 (July 2017).

12. Castillo, E., Lima, J. A. C. & Bluemke, D. A. Regional Myocardial Function: Advances in MR Imaging and Analysis. *RadioGraphics* **23,** S127–S140. ISSN: 0271-5333. http://pubs.rsna.org/doi/10.1148/rg.23si035512 (Oct. 2003).

13. Moore, C. C., Lugo-Olivieri, C. H., McVeigh, E. R. & Zerhouni, E. A. Three-dimensional Systolic Strain Patterns in the Normal Human Left Ventricle: Characterization with Tagged MR Imaging. *Radiology* **214,** 453–466. ISSN: 0033-8419. arXiv: NIHMS150003. http://pubs.rsna.org/doi/10.1148/radiology.214.2.r00fe17453 (Feb. 2000).

14. Ibrahim, E.-S. H. Myocardial tagging by Cardiovascular Magnetic Resonance: evolution of techniques–pulse sequences, analysis algorithms, and applications. *Journal of Cardiovascular Magnetic Resonance* **13,** 36. ISSN: 1532-429X. http://jcmr-online.biomedcentral.com/articles/10.1186/1532-429X-13-36%20https://jcmr-online.biomedcentral.com/articles/10.1186/1532-429X-13-36 (Dec. 2011).

15. Jeung, M.-Y., Germain, P., Croisille, P., Ghannudi, S. E., Roy, C. & Gangi, A. Myocardial Tagging with MR Imaging: Overview of Normal and Pathologic Findings. *RadioGraphics* **32,** 1381–1398. ISSN: 0271-5333. http://pubs.rsna.org/doi/10.1148/rg.325115098 (Sept. 2012).

16. Taylor, R. J., Umar, F., Panting, J. R., Stegemann, B. & Leyva, F. Left ventricular lead position, mechanical activation, and myocardial scar in relation to left ventricular reverse remodeling and clinical outcomes after cardiac resynchronization therapy: A feature-tracking and contrast-enhanced cardiovascular magnetic r. *Heart Rhythm* **13,** 481–489. ISSN: 15475271. https://linkinghub.elsevier.com/retrieve/pii/S1547527115013053 (Feb. 2016).

17. Claus, P., Omar, A. M. S., Pedrizzetti, G., Sengupta, P. P. & Nagel, E. Tissue Tracking Technology for Assessing Cardiac Mechanics. *JACC: Cardiovascular Imaging* **8,** 1444–1460. ISSN: 1936878X. https://linkinghub.elsevier.com/retrieve/pii/S1936878X15008451 (Dec. 2015).

18. Aletras, A. H., Ding, S., Balaban, R. S. & Wen, H. DENSE: Displacement Encoding with Stimulated Echoes in Cardiac Functional MRI. *Journal of Magnetic Resonance* **137,** 247–252. ISSN: 10907807. https://linkinghub.elsevier.com/retrieve/pii/S1090780798916767 (Mar. 1999).

19. Cruz-Bastida, J. P., Gomez-Cardona, D., Li, K., Sun, H., Hsieh, J., Szczykutowicz, T. P. & Chen, G.-H. Hi-Res scan mode in clinical MDCT systems: Experimental assessment of spatial resolution performance. *Medical Physics* **43,** 2399–2409. ISSN: 00942405. http://doi.wiley.com/10.1118/1.4946816 (Apr. 2016).

20. Chen, Z., Contijoch, F., Schluchter, A., Grady, L., Schaap, M., Stayman, W., Pack, J. & McVeigh, E. Precise measurement of coronary stenosis diameter with CCTA using CT number calibration. *Medical Physics* **46,** 5514–5527. ISSN: 0094-2405. https://onlinelibrary.wiley.com/doi/10.1002/mp.13862 (Dec. 2019).

21. Contijoch, F., Stayman, J. W. & McVeigh, E. R. The impact of small motion on the visualization of coronary vessels and lesions in cardiac CT: A simulation study. *Medical Physics* **44,** 3512–3524. ISSN: 00942405. http://doi.wiley.com/10.1002/mp.12295 (July 2017).

22. Manohar, A., Rossini, L., Colvert, G., Vigneault, D. M., Contijoch, F., Chen, M. Y., del Alamo, J. C. & McVeigh, E. R. Regional dynamics of fractal dimension of the left ventricular endocardium from cine computed tomography images. *Journal of Medical Imaging* **6,** 1. ISSN: 2329-4302. https://www.spiedigitallibrary.org/journals/journal-of-medical-imaging/volume-6/issue-04/046002/Regional-dynamics-of-fractal-dimension-of-the-left-ventricular-endocardium/10.1117/1.JMI.6.4.046002.full (Nov. 2019).

23. Chen, M. Y., Shanbhag, S. M. & Arai, A. E. Submillisievert Median Radiation Dose for Coronary Angiography with a Second-Generation 320–Detector Row CT Scanner in 107 Consecutive Patients. *Radiology* **267,** 76–85. ISSN: 0033-8419. http://pubs.rsna.org/doi/10.1148/radiol.13122621 (Apr. 2013).

24. McCollough, C. H., Chen, G. H., Kalender, W., Leng, S., Samei, E., Taguchi, K., Wang, G., Yu, L. & Pettigrew, R. I. Achieving Routine Submillisievert CT Scanning: Report from the Summit on Management of Radiation Dose in CT. *Radiology* **264,** 567–580. ISSN: 0033-8419. http://pubs.rsna.org/doi/10.1148/radiol.12112265 (Aug. 2012).

25. Cerqueira, M. D., Weissman, N. J., Dilsizian, V., Jacobs, A. K., Kaul, S., Laskey, W. K., Pennell, D. J., Rumberger, J. A., Ryan, T. & Verani, M. S. Standardized Myocardial Segmentation and Nomenclature for Tomographic Imaging of the Heart. *Circulation* **105,** 539–542. ISSN: 0009-7322. https://www.ahajournals.org/doi/10.1161/hc0402.102975 (Jan. 2002).

26. Auger, D. A., Bilchick, K. C., Gonzalez, J. A., Cui, S. X., Holmes, J. W., Kramer, C. M., Salerno, M. & Epstein, F. H. Imaging left-ventricular mechanical activation in heart failure patients using cine DENSE MRI: Validation and implications for cardiac resynchronization therapy. *Journal of Magnetic Resonance Imaging* **46,** 887–896. ISSN: 10531807. http://doi.wiley.com/10.1002/jmri.25613%20https://onlinelibrary.wiley.com/doi/10.1002/jmri.25613 (Sept. 2017).

27. Bilchick, K. C., Kuruvilla, S., Hamirani, Y. S., Ramachandran, R., Clarke, S. A., Parker, K. M., Stukenborg, G. J., Mason, P., Ferguson, J. D., Moorman, J. R., Malhotra, R., Mangrum, J. M., Darby, A. E., DiMarco, J., Holmes, J. W., Salerno, M., Kramer, C. M. & Epstein, F. H. Impact of Mechanical Activation, Scar, and Electrical Timing on Cardiac Resynchronization Therapy Response and Clinical Outcomes. *Journal of the American College of Cardiology* **63,** 1657–1666. ISSN: 07351097. https://linkinghub.elsevier.com/retrieve/pii/S073510971401170X (Apr. 2014).

28. Kim, S., Chang, Y. & Ra, J. B. Cardiac motion correction based on partial angle reconstructed images in x-ray CT. *Medical Physics* **42,** 2560–2571. ISSN: 00942405. http://doi.wiley.com/10.1118/1.4918580 (Apr. 2015).

29. Manohar, A., Pack, J. D., Schluchter, A. J. & McVeigh, E. R. Four-dimensional computed tomography of the left ventricle, Part II: Estimation of mechanical activation times. *Medical Physics.* ISSN: 0094-2405. https://onlinelibrary.wiley.com/doi/10.1002/mp.15550 (Mar. 2022).

Chapter 2

Spatial resolution of regional cardiac function assessment with 4DCT

We developed an anthropomorphically accurate left ventricular (LV) phantom derived from human CT data to serve as ground truth for the optimization and the spatial resolution quantification of a CT-derived regional strain metric (SQUEEZ). Displacements were applied to the mesh points of a clinically derived end diastolic LV mesh to create analytical end systolic poses with physiologically accurate endocardial strains. Normal function as well as regional dysfunction of four sizes (1, 2/3, 1/2, and 1/3 AHA segments as core diameter), each exhibiting hypokinesia (70% reduction in strain) and subtle hypokinesia (40% reduction in strain), were simulated. Regional shortening RS_{CT}estimates were obtained by registering the end diastolic mesh to each simulated end systolic mesh condition using a non-rigid registration algorithm. Ground-truth models of normal function and of hypokinesia were used to identify the optimal parameters in the registration algorithm, and to measure the accuracy of detecting regional dysfunction

of varying sizes and severities. For normal LV function, RS_{CT}values in all 16 AHA segments were accurate to within 5%. For cases with regional dysfunction, the errors in RS_{CT}around the dysfunctional region increased with decreasing size of dysfunctional tissue.

2.1 Background

SQUEEZ [1] is a new method introduced to measure regional endocardial strain from 4DCT images acquired with routine clinical protocols. SQUEEZ exploits the high fidelity of 4DCT to track features of the endocardium, which are used by a non-rigid point set registration technique [2] to derive displacements of points on the endocardium across the cardiac cycle. This displacement estimate is used to obtain information on the regional shortening of the endocardium. SQUEEZ has shown to be capable of differentiating normal from dysfunctional myocardial regions in pigs [1], has been compared with CMR tagging derived circumferential shortening in canines [3], and more recently, baseline estimates of RS_{CT}values derived from SQUEEZ in the normal human LV were established [4]. In addition to the LV, SQUEEZ has shown to be capable of identifying regional differences in systolic function in complex right-ventricle (RV) geometries [5].

Cross-modality comparisons of regional strain measures in humans is a difficult task and the measurements made maybe subject to modality-specific biases as each imaging modality has inherent limitations ranging from operator variability to through-plane motion. Additionally, trabeculation of the endocardium is species dependent, with human hearts having more trabeculation than either porcine or canine hearts; hence, the prior optimization of SQUEEZ will likely need adjustment for human hearts. Significant effort has been laid on the development of computerized phantoms of the human heart which provide an essential ground-truth in the opti-

mization and evaluation of various imaging devices and techniques. Some of these phantoms are derived directly from patient image data (voxel phantoms) [6–9], while others are defined using mathematical primitives [10, 11]. The voxel phantoms are anatomically accurate but are limited in their flexibility for modelling different motions and anatomies, while on the other hand, the mathematical phantoms offer a great deal of modelling flexibility but do not accurately represent the human anatomy. A new breed of hybrid phantoms that combine the advantages of the above two classes have been developed [12–15]. These phantoms have been very useful in optimizing and evaluating various imaging systems for optimal patient diagnosis and treatment.

In this chapter, we describe the development of an anthropomorphically accurate LV mesh phantom with defined correspondences between endocardial points as a function of time across the cardiac cycle [16]. The phantom is derived from a high-resolution CT scan of a human LV and displacements were applied to each point to create analytical end systolic poses exhibiting physiologically accurate endocardial strains. Using the phantom, we tune the parameters of the registration algorithm to achieve optimal registration between the end diastolic and the end systolic LV poses. Additionally, we also quantify the spatial resolution limits of SQUEEZ for the estimation of regional wall motion abnormalities, thereby performing the first analytical evaluation of SQUEEZ using an anthropomorphically accurate phantom of the human LV.

2.2 Methods

2.2.1 Image Acquisition

The end diastolic phase of a human cardiac CT scan was used as the baseline image for phantom development. The image was acquired under IRB approved protocols at the National

Institutes of Health (Bethesda, Maryland) using retrospective electrocardiogram (ECG) gating with inspiratory breath-hold. The scanner used was a 320 detector-row (Aquilion ONE, Canon Medical Systems, Otawara, Japan), which enabled complete coverage of the heart from a single table position. The scan parameters were: tube current - 280 mA, kVP - 100 kV, and short scan acquisition with a gantry revolution time of 275 ms. Full R-R image data spanning a complete cardiac cycle was acquired and the end diastolic phase was reconstructed at 0% of the R-R phase. Optimal opacification from contrast dye was achieved using real-time bolus tracking.

The image was reconstructed into a matrix of 512 x 512 x 320 voxels using the manufacturer's (Canon Medical Systems) standard reconstruction algorithm (reconstruction diameter: 173.5 mm; kernel: Cardiac FC08), as implemented clinically. The image had voxel dimensions of 0.34 x 0.34 x 0.50 mm3 in the x, y, and z dimensions respectively. Neither the imaging parameters nor subject enrolment were determined by the authors for the purpose of our particular study. The images used in this work were directly obtained from the clinic with acquisition and reconstruction parameters determined by the clinical protocol used for that study.

2.2.2 Image Processing & Mesh Extraction

The LV endocardium was segmented with ITK-SNAP [17] using the active contour region growing module (thresholding type = high pass; threshold = 450; smoothness = 10; seed radius = 5; all other parameters were set as default). All further processing steps were performed in MATLAB (MathWorks Inc.).

The binary LV segmentation was loaded into MATLAB in its native orientation (original axial slices) and resolution. Prior to extracting the endocardial mesh, the binary LV volume was resampled to an isotropic resolution of 0.5 x 0.5 x 0.5 mm3 by linear interpolation. The isotropic

binary volume was rotated sequentially about the x and y axes to align the LV long axis with the z axis; hence, the longitudinal direction of the model is equivalent to the z-direction.

The binary LV volume was subsampled to a resolution of 2 x 2 x 2 mm3 by retaining every fourth (2mm/0.5mm) voxel in x, y, and z directions to achieve a spatial sampling consistent with previously published SQUEEZ analyses [1, 3–5]. A mesh of the boundary between the LV blood pool and the endocardium was extracted using the *isosurface* built-in MATLAB routine. The mesh comprised of 5257 faces and 2662 mesh points. A summary of the process is shown in Fig. 2.1A-C.

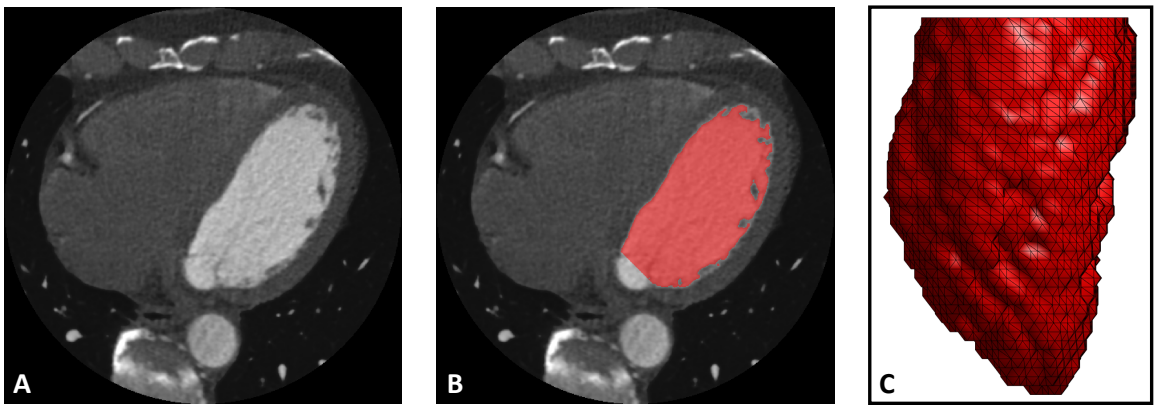

Figure 2.1: Image segmentation and mesh extraction. (A) Axial slice of the CT image. (B) Axial slice with the LV blood volume segmentation overlaid in red (with the mitral valve and the LV outflow-tract defined as the cut-off points). (C) 3D rendering of the extracted LV endocardial mesh, looking at the lateral wall with the anterior wall to the left, and the inferior wall to the right.

2.2.3 Strain Model

The end diastolic mesh, obtained from the LV segmentation as described in Sec. 2.2.2, was deformed to an analytical end systolic pose by prescribing displacements to the mesh points to achieve physiologically accurate end systolic strains. The three deformations modeled were:

1. Longitudinal strain (ε_{zz}): constant -21% [18] from apex to base

2. Circumferential strain (ε_{cc}): linear reduction from -44% at the apex to -34% at the base [18]

3. Azimuthal rotation around the long axis ($\Delta\theta$): linear decrease [19] in rotation from 13°in the counter-clockwise direction at the apex to 6.9°in the clockwise direction at the base, when viewed from apex to base [20]

Azimuthal rotation represents the rotation of the LV endocardium during systole; changes in $\Delta\theta$ as a function of long axis position create torsion in the LV model. The EF of the model was 70%, which was consistent with CT-based LV EFs measured in normal hearts [4]. Figure 2.2 shows the peak end systolic strain values as a function of z-position along the long axis of the LV.

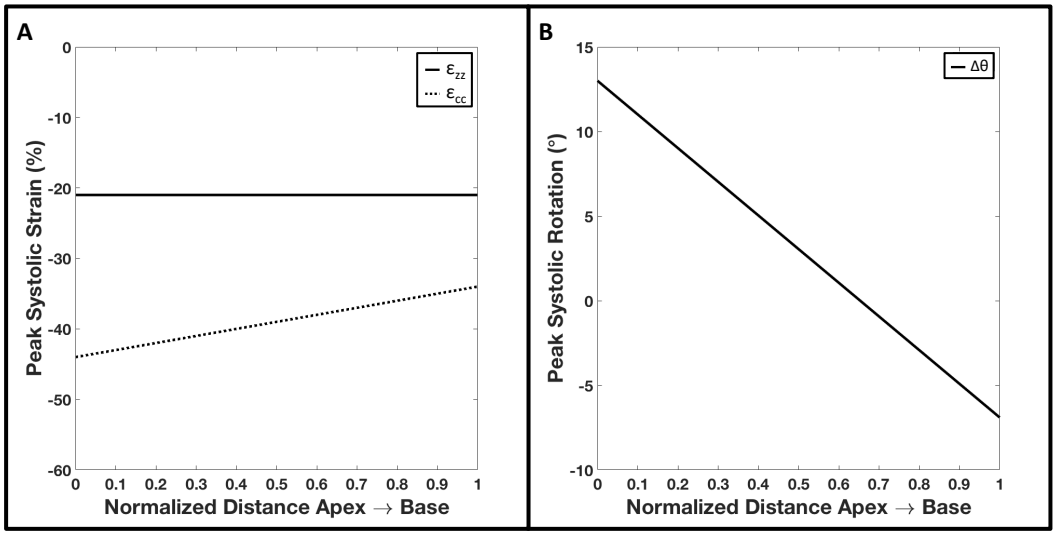

Figure 2.2: Components of the peak end systolic strain model as a function of z-position along the long axis of the LV from apex (position 0) to base (position 1). (A) Peak end systolic longitudinal (ε_{zz}; solid line) and circumferential (ε_{cc}; dotted line) strains as a function of the LV long axis (B) Peak end systolic LV rotation as a function of the LV long axis (positive rotation is counter-clockwise when viewed from apex looking up towards the base).

Displacement functions

Displacements were prescribed to each mesh point (x,y,z) in order to attain the desired three deformations specified above according to the following equations:

$$x' = \{x \cdot cos[\Delta\theta(\widetilde{z})] - y \cdot sin[\Delta\theta(\widetilde{z})]\} \times [1 + \epsilon_{cc}(\widetilde{z})], \tag{2.1}$$

$$y' = \{x \cdot sin[\Delta\theta(\widetilde{z})] + y \cdot cos[\Delta\theta(\widetilde{z})]\} \times [1 + \epsilon_{cc}(\widetilde{z})], \tag{2.2}$$

$$z' = z_0 + (z - z_0) \times (1 + \epsilon_{zz}), \tag{2.3}$$

where (x',y',z') are the new displaced coordinates, $\widetilde{z}$ is the normalized z coordinate (0 at the apex and 1 at the base), and z_0 is the fixed apical z coordinate.

Regional dysfunction model

Regional dysfunction was incorporated into the strain model by prescribing a reduction factor in the ϵ_{zz} and the ϵ_{cc} components over a particular region of interest. The dysfunction model had three adjustable parameters:

1. Position: spatial coordinates of the center of the dysfunctional region
2. Severity: reduction factor in strain at the center of the dysfunctional region
3. Size: diameter at which a 13% reduction from the desired dysfunctional severity occurred; defined as the 'core' diameter

To ensure continuity of the LV tissue, a 2D sigmoid function was used to define the dysfunctional region to create a smooth transition radially outward from the center (where severity

is maximum) to the normal tissue (see Appendix A, Sec. A.1). The sizes of the dysfunctional regions were reported in terms of fractions of an AHA segment [21] (corresponding to the American Heart Association's 17 segment model) defining the core of the dysfunctional region. The extent of the core was defined as the diameter at which a 13% reduction from the desired dysfunctional severity occurred; this corresponded to the flat 'table-top' region of the sigmoid function. A representative human end diastolic LV circumference of 170 mm was used as reference to define the AHA segments. For example, 1/2 an AHA segment translated to a core of 14 mm (170 mm/12).

Two severities of dysfunction were investigated in this paper: 1) hypokinesia, defined by a peak 70% reduction at the center in the ϵ_{zz} and the ϵ_{cc} components and 2) subtle hypokinesia, defined by a peak 40% reduction at the center in the ϵ_{zz} and the ϵ_{cc} components.

Texture smoothing

To mimic the CT image sampling of the end systolic pose of the ventricle more accurately, a low-pass filter was applied on the mesh using the iso2mesh [22] MATLAB toolbox (method = 'lowpass'; iterations = 4; alpha = 0.4). This was motivated by the change in LV endocardial texture during systole [23, 24] due to collapsing spaces between trabeculae coupled with spatial resolution limitations of the CT scanner; as the trabeculae come closer together in the analytical phantom due to myocardial contraction, the spatial frequency of the endocardial surface increases. Due to the scanner's finite resolution (point spread function), these high frequency structures can no longer be resolved giving rise to a smoothed texture of the endocardium at end systole. To simulate this texture change of the LV, a filter was applied. The filter was a Laplace filter applied in two steps; a forward step (smoothing; eqn. 2.4) and a backward step (volume conserving; eqn. 2.5) according to the following equations [25]

$$p' = p + \alpha \sum_{i=1}^{n} \phi(q_i - p), \qquad 0 < \alpha < 1, \qquad \phi = \frac{1}{n}, \tag{2.4}$$

$$p'' = p' + \mu \sum_{i=1}^{n} \phi(q_i - p), \qquad \mu = -1.02\alpha, \qquad \phi = \frac{1}{n}, \tag{2.5}$$

where p, p', and p'' are the original, intermediate, and final positions of a mesh point p and i = 1,2,3,...,n is the index number of the n neighboring mesh points q. The parameters α, μ, and number of iterations were chosen such that the frequency response of the applied filter was similar to that of the Standard reconstruction kernel of a 256 detector-row clinical scanner (Revolution CT, General Electric Medical Systems, Wisconsin; see Appendix A, Sec. A.2). Figure 2.3 shows the end diastolic (Fig. 2.3A) and the analytically derived final end systolic poses (with smoothing) under normal function (Fig. 2.3A) and a sample case exhibiting regional dysfunction (Fig. 2.3C).

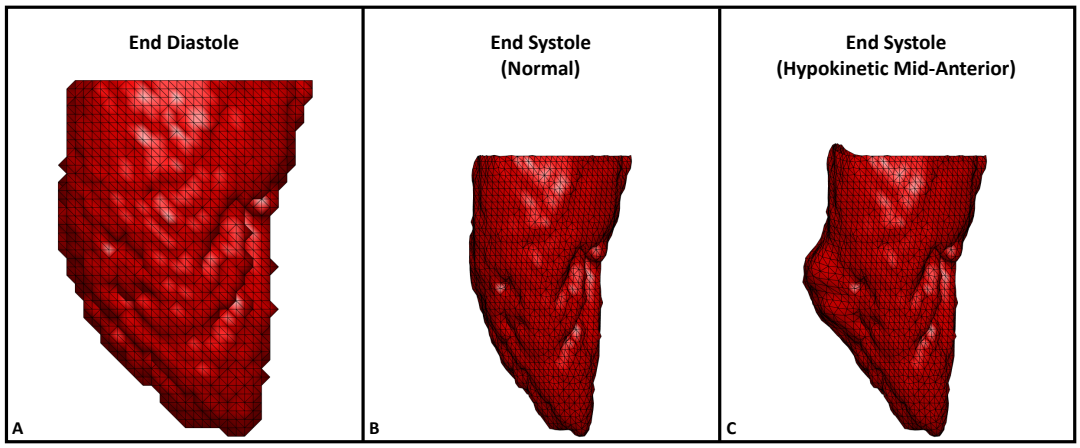

Figure 2.3: End diastolic and analytically derived end systolic LV poses. (A) End diastolic mesh derived from human LV clinical CT data. (B) Analytically derived end systolic pose with normal function. (C) Analytically derived end systolic pose exhibiting regional hypokinesia of 1/2 an AHA segment (14 mm) as core diameter at the mid-anterior segment of the LV with normal strain values in all other segments. All three views are of the LV lateral wall with the anterior wall to the left and the inferior wall to the right.

2.2.4 Non-rigid Point Set Registration

Coherent Point Drift (CPD), a probabilistic non-rigid point set registration technique [2], was used to register the end diastolic template mesh to the end systolic target mesh. Since our model had a perfect 1:1 correspondence, the registration accuracy could be validated with the known ground-truth. However, in the clinical scenario, a 1:1 correspondence does not exist between the end diastolic and the end systolic mesh points. From 10 4DCT scans of human LVs with normal function (CT measured LV EF: 73% $\pm$ 4%), meshes were extracted at end diastole and end systole and the ratio of the number of mesh points at end systole to end diastole was calculated to be 46% $\pm$ 7%; therefore, only 50% of the mesh points (every alternate point) in the analytically derived end systolic poses were retained.

Additionally, a uniform distribution of random noise in the range of $\pm$ 0.6 mm was added to the coordinates (x,y,z) of the down-sampled end systolic pose to make the noise independent. The limits of the added noise were determined by calculating the natural variability in the detection of the endocardial edge for different contrast-to-noise levels obtained by changing the x-ray tube current settings (see Appendix A, Sec. A.3). This down-sampled end systolic pose with added noise was used as the target for the registration of the template end diastolic mesh.

Identification of optimal set of CPD parameters

The CPD algorithm has 2 free parameters: β and λ. β is the width of the Gaussian smoothing kernel and λ is the regularization weight [2]. Both β and λ define the coherence of motion between neighboring points; an increase in either value, forces the points to move in a more coherent manner, while lower values allow for more localized deformations.

For our application of detecting a subtle wall motion abnormality, we needed the registra-

tion algorithm to balance global coherent motion with the ability to track localized deformations. The warping of the template end diastolic mesh to the target end systolic mesh had to be performed in a physiologically accurate manner (coherent motion), while simultaneously capturing regional abnormalities in cardiac contraction (localized changes in the expected motions). From visual inspection trials, performed on phantoms representing both normal LV function and regional hypokinetic function (1/2 AHA segment (14 mm) as core diameter), we observed β values between [0.5, 2] in steps of 0.1 and λ values between [1, 25] in steps of 1 covered the domain of values of interest. The above identified values for β and λ defined 400 (16β x 25λ) sets of possible parameters for the registration algorithm. From these 400, we sought to identify one set of parameters which yielded the 'best' (defined in the next section) registration between end diastole and end systole under both, normal and regional dysfunction conditions. The 1/2 AHA segment hypokinetic model was chosen based on two factors: 1) from visual inspection of wall motion abnormalities seen on CT images, this was considered smaller than the average size of dysfunction and 2) by optimizing for hypokinetic function, the registration fit would be better capable of capturing subtle wall motion abnormalities. The core of the 1/2 AHA segment hypokinetic region contained 36 mesh points.

Statistical evaluation

The accuracy and quality of the registration fit was assessed based on four metrics:

1. Global l^2 norm: The global l^2 norm was computed for all mesh points of the LV according to the formula:

$$l^2_{glo} = \frac{1}{N}\sqrt{\sum_{i=1}^{N}(x_i^0 - x_i)^2 + (y_i^0 - y_i)^2 + (z_i^0 - z_i)^2} \tag{2.6}$$

where (x^0,y^0,z^0) are the coordinates of the ground-truth mesh, (x,y,z) are the corresponding coordinates of the registered mesh, and i = 1,2,3,...,2662(N) is the index of the mesh points.

2. Regional l^2 norm: The regional l^2 norm was computed over the mesh points of the programmed dysfunctional region of the LV according to the formula:

$$l^2_{reg} = \frac{1}{n}\sqrt{\sum_{i=1}^{n}(x_i^0 - x_i)^2 + (y_i^0 - y_i)^2 + (z_i^0 - z_i)^2} \tag{2.7}$$

where (x^0,y^0,z^0) are the coordinates of the ground-truth mesh, (x,y,z) are the corresponding coordinates of the registered mesh, and i = 1,2,3,...,320(n) is the index of the mesh points within the programmed dysfunctional region.

3. Euclidean distance: Unlike the l^2 norm which provides an average measure of goodness of fit for all points in consideration, Euclidean distance was calculated on a point-by-point basis according to the formula:

$$dist_i = \sqrt{(x_i^0 - x_i)^2 + (y_i^0 - y_i)^2 + (z_i^0 - z_i)^2} \tag{2.8}$$

where (x^0,y^0,z^0) are the coordinates of the ground-truth mesh, (x,y,z) are the corresponding coordinates of the registered mesh, and i = 1,2,3,...,2662(N) is the index of the mesh points.

4. SQUEEZ: SQUEEZ [1] is a user-independent method developed to measure endocardial regional shortening ($\mathrm{RS_{CT}}$). It is measured by tracking features on the endocardium from 4DCT data and is computed as the square root of the ratio of areas of corresponding patches between a template mesh and a target mesh, according to the formula:

$$RS_{\mathrm{CT}} = \sqrt{\frac{A(\nu,t)}{A(\nu,t=0)}} - 1 \tag{2.9}$$

where $A(\nu, t)$ refers to the area of a patch ν at time t and $A(\nu, t = 0)$ is the area of the same patch at time $t = 0$ (end diastole). Consistent with previously published SQUEEZ analyses, each patch was defined as a single triangular face of the end diastolic template mesh; the average patch size at end diastole was 2.6 $\pm$ 0.5 mm^2. Recently, from a cohort of 25 subjects with normal LV function, McVeigh et al. determined the average peak end systolic RS_{CT}value over the entire LV endocardium to be -34% $\pm$ 5% [4].

Only those values of β and λ, from the pool of 400, that yielded registration fits that satisfied the following inclusion criteria were shortlisted:

1. Global l^2 norm in the normal case $\leq$ 0.015 (bottom 90% of all l^2 norms; errors were consistently low for the simulated normal LV function)
2. Regional l^2 norm in the dysfunctional case $\leq$ 0.07 (bottom 40% of all regional l^2 norms)
3. 95% of RS_{CT}values in the normal case to be within $\pm$5% [4] from the ground-truth
4. 90% of mesh points (2396 in number) in both the normal and the dysfunctional case to be within $\pm$1 mesh point distance ($\pm$2 mm) from the ground-truth
5. RS_{CT}values in all 16 AHA segments in the normal case to be within $\pm$5% from the ground-truth
6. RS_{CT}values in 15 normal AHA segments (excluding the mid-anterior segment containing the programmed dysfunctional region; AHA segment 7) in the dysfunctional case to be within $\pm$5% from the ground-truth
7. Average RS_{CT}value in abnormal AHA segment 7 (mid-anterior segment containing the programmed dysfunctional region) in the dysfunctional case $\geq$ -26% (average ground-truth

RS_{CT}value in the normal LV = -31%, hence cut-off threshold for abnormal function is -31% + 5% = -26%). The theoretical RS_{CT}value in the core of the hypokinetic region was -12% ± 2.2%.

2.2.5 Quantifying Spatial Resolution Limits of SQUEEZ for the Detection of Regional Dysfunction

Four sizes of regional dysfunction (1, 2/3, 1/2, and 1/3 AHA segments translating to core diameters of 28, 19, 14, and 9.5 mm respectively), each modeled with hypokinesia and subtle hypokinesia (defined in Sec. 2.2.4) were used to sample the threshold of detection of abnormal strain with SQUEEZ. The optimal set of CPD parameters was used and the target end systolic meshes for each size and severity of dysfunction were prepared as outlined in Sec. 2.4 (down-sampled and independent noise added).

Box plots of the distribution of RS_{CT}values within the core of the dysfunctional regions, for both the ground-truth and the registered meshes, were used to quantify the accuracy. The spatial resolution limit of SQUEEZ under both regional hypokinetic and subtle hypokinetic functions was defined as the smallest lesion size that SQUEEZ can accurately detect to within ±5% of the theoretical RS_{CT}value in the core of the dysfunctional regions.

2.3 Results

The results are presented under two sections: 1) identification of the optimal set of parameters for CPD registration and 2) quantification of the spatial resolution limits for the detection of regional wall motion abnormalities.

2.3.1 Optimal Set of Parameters for CPD Registration

From the 400 sets of parameters, only 6 sets of parameters satisfied the 7 inclusion criteria outlined in Sec. 2.2.4. β values only between 1 and 1.1 satisfied the inclusion criteria; high values of β imposed strong coherence of motion and hence, regional displacements (hypokinetic/infarct regions) were compromised while very low values of β led to hyper-flexible meshes. The values of λ ranged from 7 to 9 for $\beta = 1.1$ and from 10 to 12 for $\beta = 1$. Also observed was an inter-dependency between β and λ; as the value of β (width of the Gaussian smoothing kernel) decreased, in order to maintain the overall quality of the mesh (coherence of point displacements), the value of λ (the regularization weight) had to increase.

Figure 2.4 plots the l^2 norms as a function of β and λ under normal and regional dysfunction cases within the domain of β and λ values that satisfied the inclusion criteria. As seen from Fig. 2.4, the errors in both regional and global fits were stable and similar across all sets of shortlisted parameters (highlighted by the red boundaries). While any of the 6 shortlisted sets of parameters could be used, we needed to choose one operating point to proceed with the investigation of the spatial resolution of SQUEEZ for the detection of regional wall motion abnormalities. From Fig. 2.4B, for a value of $\beta = 1.1$, the errors across a wide range of λ values between [7,13] were stable and consistently low; this served as motivation to choose $\beta = 1.1$ over $\beta = 1.0$. Among the three available λ values of 7, 8, and 9 for $\beta = 1.1$, $\lambda = 9$ was chosen as the operating point to provide the highest regularization from among the shortlisted parameters. While our simulation was performed under controlled circumstances, human LVs artifactually lose features during systole in a non-coherent fashion (such as trabeculae collapsing and papillary muscles merging with the endocardium); hence for clinical LV scans, we expect that a higher regularization of the registration fit would decrease the influence of the artifactual

non-rigid deformation caused by the above listed artifacts.

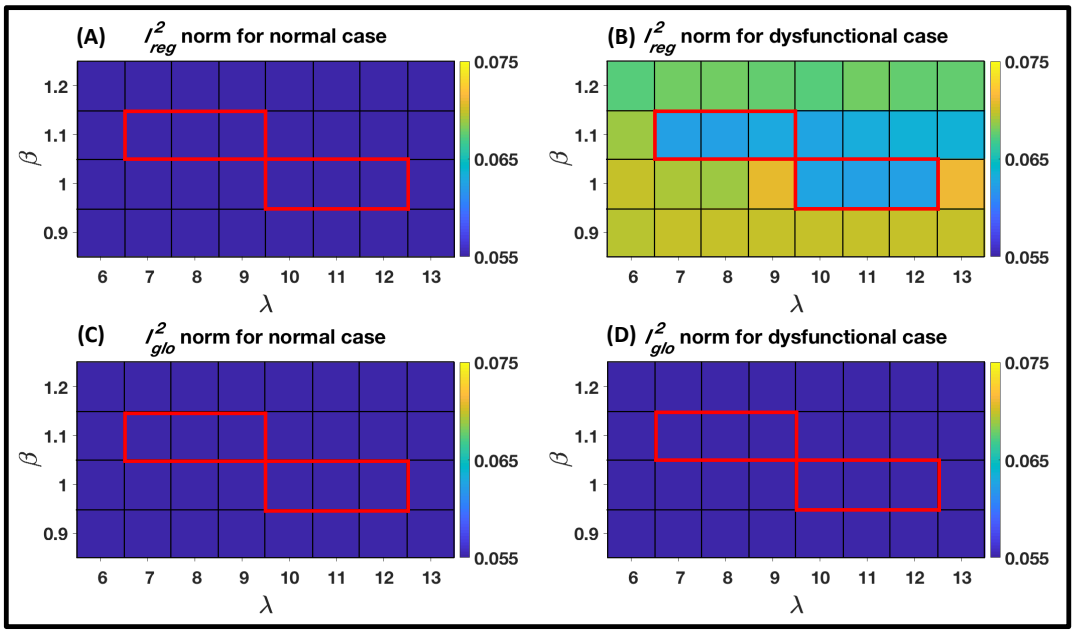

Figure 2.4: Registration errors as a function of β and λ within the domain of β and λ values that satisfied the inclusion criteria. (A) l^2 norm computed over a region of the endocardium in the model with normal LV function that corresponded to the hypokinetic region in the regional dysfunction model. (B) l^2 norm computed over the hypokinetic region in the regional dysfunction model. (C) l^2 norm computed over the entire endocardium in the model with normal LV function. (D) l^2 norm computed over the entire endocardium in the regional dysfunction model. The registration errors were stable and similar across all parameter sets that satisfied the inclusion criteria (highlighted by the red boundaries).

2.3.2 Spatial Resolution Limits of SQUEEZ for the Detection of Regional Dysfunction

Four sizes of regional dysfunction were simulated with each size exhibiting hypokinesia and subtle hypokinesia (see Sec. 2.2.5). Figure 2.5 summarizes the results of SQUEEZ for the detection of hypokinesia for the four sizes of simulated regional dysfunction. Panels A and B show the end systolic poses of the anterior wall of the LV with RS_{CT}values mapped onto the endocardial surface (panel A: programmed ground-truth RS_{CT}maps; panel B: RS_{CT}maps

derived from SQUEEZ). Panel C shows boxplots (bottom and top edges of each box correspond to the 25^{th} and the 75^{th} percentiles and the central line indicates the median) of the ground-truth (in blue) and the SQUEEZ derived (in pink) RS_{CT}values within the core of each of the four dysfunctional regions. For a detection threshold of $\pm$ 5% from the theoretical RS_{CT}value within the core of the dysfunctional regions, Fig. 2.5 demonstrates the smallest lesion size that can be confidently measured with SQUEEZ processing. Hypokinetic regions of 1 and 2/3 AHA segments as core diameter were accurately measured while the severity of dysfunction in the 1/2 and 1/3 AHA segments was underestimated.

Similarly, Fig. 2.6 summarizes the results of SQUEEZ for the detection of subtle hypokinesia for the four sizes of simulated regional dysfunction. Panels A and B show the end systolic poses of the anterior wall of the LV with RS_{CT}values mapped onto the endocardial surface (panel A: programmed ground-truth RS_{CT}maps; panel B: RS_{CT}maps derived from SQUEEZ). Panel C shows boxplots of the ground-truth and the SQUEEZ derived RS_{CT}values within the core of each of the four dysfunctional regions. Again, subtle hypokinetic regions of 1 and 2/3 AHA segments as core diameters were accurately measured while the severity of dysfunction in the 1/2 and 1/3 AHA segments was underestimated.

As seen from Figs. 2.5 and 2.6, the reduction in strain in localized and subtle wall motion abnormalities was underestimated. While SQUEEZ was able to capture lesions of size greater than 2/3 AHA segments with high accuracy, this result suggested that secondary techniques need to be identified and developed to facilitate the accurate capture of smaller localized regions of dysfunction.

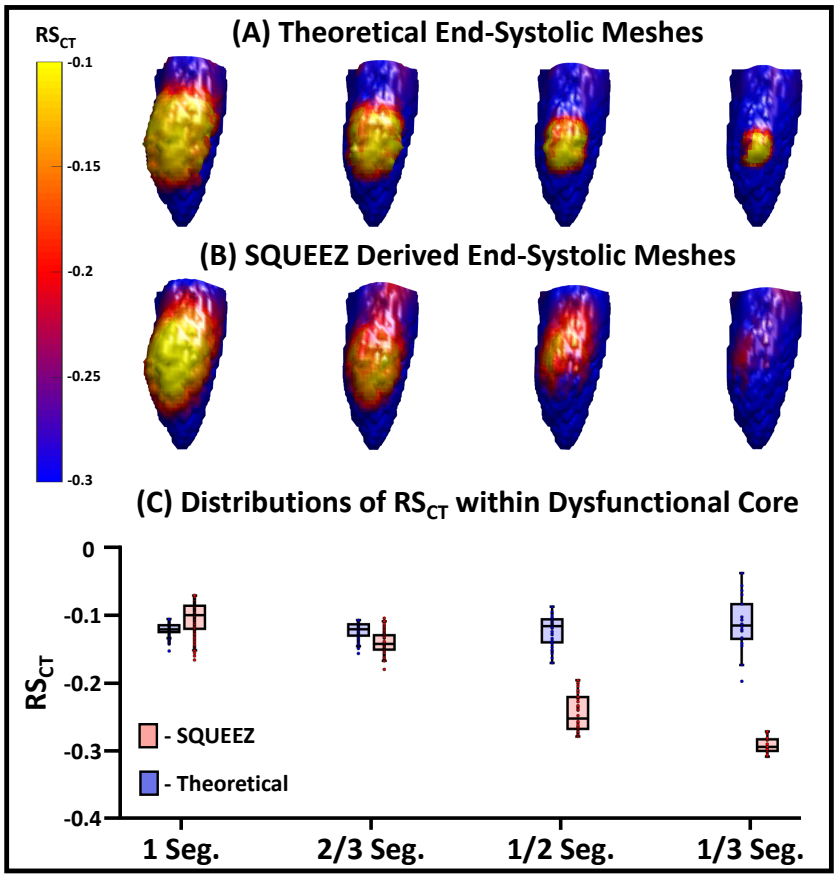

Figure 2.5: Detection of hypokinesia with SQUEEZ for four different sizes of regional dysfunction. (A-B) End systolic LV poses showing the anterior wall with regional shortening (RS_{CT}) values mapped onto the endocardial surface for the four sizes of regional dysfunction (A – programmed ground-truth RS_{CT}maps; B – RS_{CT}maps obtained with SQUEEZ). Yellow corresponds to low function and blue corresponds to normal function. (C) Boxplots of ground-truth and SQUEEZ derived RS_{CT}values within the core of each of the four dysfunctional regions.

2.4 Discussion

This manuscript presents an anthropomorphic LV mesh phantom derived from human cardiac CT data and prescribed with physiologically accurate strain functions [18–20] to create analytically known systolic poses. We have introduced an LV mesh model with programmable dysfunctional regions of various sizes, shapes, and severities for the first analytical evaluation of the spatial resolution of SQUEEZ for the human LV. A potential alternative to the work

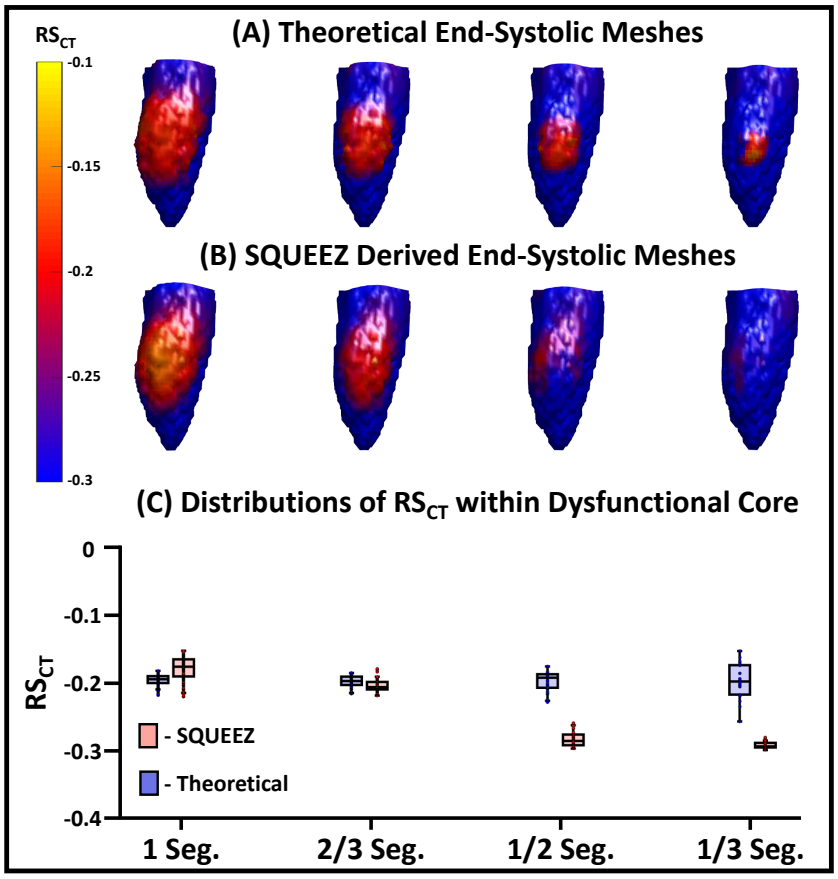

Figure 2.6: Detection of subtle hypokinesia with SQUEEZ for four different sizes of regional dysfunction. (A-B) End systolic LV poses showing the anterior wall with regional shortening (RS_{CT}) values mapped onto the endocardial surface for the four sizes of regional dysfunction (A – programmed ground-truth RS_{CT}maps; B – RS_{CT}maps obtained with SQUEEZ). Yellow corresponds to low function and blue corresponds to normal function. (C) Boxplots of ground-truth and SQUEEZ derived RS_{CT}values within the core of each of the four dysfunctional regions.

described here would be to compare strain estimates from SQUEEZ with those derived from another imaging technique such as MR tagging. However, comparing strain values in the human heart measured with two different imaging techniques is fraught with problems; the human subject needs to be imaged with each technique in quick succession, and each technique has its own inherent limitations. The LV phantom developed in this work provides a platform to compare the measured strain values with the actual programmed ground-truth values. In addition to the measurement of regional shortening, the model also provides a platform to investigate the

assessment of other LV phenomena such as dyssynchrony and endocardial twist, which were not examined in the work reported here. Another advantage of the developed mathematical phantom is that the analytically derived systolic poses can be used to create 3D printed physical phantoms, serving as a ground-truth for understanding the implications of different imaging protocols on the assessment of LV function using CT.

Using a model for normal LV function and a model for regional dysfunction of moderate size and severity, a set of parameters for the CPD registration algorithm was identified for our task. This was the first attempt at identifying the optimal set of CPD parameters for the quantification of human regional LV function using SQUEEZ. With these parameters, the accuracy of SQUEEZ for detecting programmed dysfunctional regions was measured. The accuracy of the strain estimate at the center of an abnormal region decreased as a function of decreasing size of the abnormal region; dysfunctional regions of 1 (28 mm) and 2/3 (19 mm) AHA segments as core diameter were captured with high accuracy, while the severity of dysfunction in the 1/2 (14 mm) and 1/3 (9.5 mm) AHA segments was underestimated. It should be noted that dysfunctional regions of 1/3 AHA segment and smaller are rarely detected by any current method in the clinical setting; however, as part of future work, more advanced approaches need to be developed to refine the SQUEEZ pipeline (modify CPD or use a different registration technique, modify mesh design) to facilitate the accurate detection of smaller localized wall motion abnormalities. Additionally, the effect of the spatial resolution of CT image acquisition on the accuracy of mesh registration and SQUEEZ needs to be investigated. Low-dose CT scans can be spatially smoothed to increase signal-to-noise ratio; the performance of SQUEEZ on smoothed data will determine the minimum dose achievable for obtaining local function with 4DCT.

2.4.1 Limitations

While the analytical phantom served as a ground-truth in the optimization and quantification of the spatial resolution limits of SQUEEZ for the detection of regional wall motion abnormalities, it does not exactly represent the texture change of the human LV during systolic contraction. Although a low-pass filter with a frequency response similar to that of a clinical CT scanner was applied to simulate the change in endocardial features, human LV systolic contraction in hearts with high ejection fraction lose endocardial features in a complex, non-random manner (for example, convergence of the papillary muscles and heart wall at end systole).

Currently, regional dysfunction is modeled in our phantom in a circular pattern, with the most severe dysfunction at the center and a smooth tapering off towards normal function radially outward. The model is limited by its symmetric shape which is likely adequate to model small regions of dysfunction; however, regional dysfunction occurs in various shapes, often in a non-isotropic manner, especially in severely abnormal hearts. While these abnormalities are simpler to detect, the accuracy of regional dysfunction quantification with non-isotropic spatial scales in x, y, and z may need to be investigated.

While the model offers a great degree of flexibility in programming regional dysfunction, it is currently limited by the lack of an accurate model of CT noise in the independent systolic phases for images with extremely low signal-to-noise ratio (i.e. images with doses < 0.2 mSv). Future work should address the effects of increasing CT noise and segmentation outliers on the computed $\mathrm{RS}_{\mathrm{CT}}$values so that the optimal smoothing can be applied and the lowest radiation dose limit estimated.

Acknowledgements

We thank Dr. Marcus Y. Chen at the Laboratory of Cardiac Energetics, National Heart, Lung, and Blood Institute, National Institutes of Health (NIH), for providing us with the human CT data used in this work.

This research was supported by NHLBI of the NIH (K01 HL143113, T32 HL105373, and R01 HL144678)

Chapter 2 is a reprint of the material: **Ashish Manohar**, Gabrielle M. Colvert, Andrew J. Schluchter, Francisco Contijoch, and Elliot R. McVeigh. "Anthropomorphic left ventricular mesh phantom: a framework to investigate the accuracy of SQUEEZ using Coherent Point Drift for the detection of regional wall motion abnormalities" *Journal of Medical Imaging* **6**, 2019. The dissertation author is the primary author.

2.5 References

1. Pourmorteza, A., Schuleri, K. H., Herzka, D. A., Lardo, A. C. & McVeigh, E. R. A New Method for Cardiac Computed Tomography Regional Function Assessment. *Circulation: Cardiovascular Imaging* **5,** 243–250. ISSN: 1941-9651. https://www.ahajournals.org/doi/10.1161/CIRCIMAGING.111.970061 (Mar. 2012).

2. Myronenko, A. & Xubo Song. Point Set Registration: Coherent Point Drift. *IEEE Transactions on Pattern Analysis and Machine Intelligence* **32,** 2262–2275. ISSN: 0162-8828. arXiv: 0905.2635. http://arxiv.org/abs/0905.2635%7B%5C%%7D0Ahttp://dx.doi.org/10.1109/TPAMI.2010.46%20http://www.ncbi.nlm.nih.gov/pubmed/20975122%20http://ieeexplore.ieee.org/document/5432191/ (Dec. 2010).

3. Pourmorteza, A., Chen, M. Y., van der Pals, J., Arai, A. E. & McVeigh, E. R. Correlation of CT-based regional cardiac function (SQUEEZ) with myocardial strain calculated from tagged MRI: an experimental study. *The International Journal of Cardiovascular Imaging* **32,** 817–823. ISSN: 1569-5794. http://link.springer.com/10.1007/s10554-015-0831-7 (May 2016).

4. McVeigh, E. R., Pourmorteza, A., Guttman, M., Sandfort, V., Contijoch, F., Budhiraja, S., Chen, Z., Bluemke, D. A. & Chen, M. Y. Regional myocardial strain measurements from 4DCT in patients with normal LV function. *Journal of Cardiovascular Computed*

Tomography **12,** 372–378. ISSN: 19345925. https://doi.org/10.1016/j.jcct.2018.05.002%20https://linkinghub.elsevier.com/retrieve/pii/S1934592518300923 (Sept. 2018).

5. Contijoch, F. J., Groves, D. W., Chen, Z., Chen, M. Y. & McVeigh, E. R. A novel method for evaluating regional RV function in the adult congenital heart with low-dose CT and SQUEEZ processing. *International Journal of Cardiology* **249,** 461–466. ISSN: 01675273. https://doi.org/10.1016/j.ijcard.2017.08.040%20https://linkinghub.elsevier.com/retrieve/pii/S0167527317334460 (Dec. 2017).

6. Kramer, R., Vieira, J. W., Khoury, H. J., Lima, F. R. A. & Fuelle, D. All about MAX: a male adult voxel phantom for Monte Carlo calculations in radiation protection dosimetry. *Physics in Medicine and Biology* **48,** 1239–1262. ISSN: 0031-9155. https://iopscience.iop.org/article/10.1088/0031-9155/48/10/301 (May 2003).

7. Kramer, R., Khoury, H. J., Vieira, J. W., Loureiro, E. C. M., Lima, V. J. M., Lima, F. R. A. & Hoff, G. All about FAX: a Female Adult voXel phantom for Monte Carlo calculation in radiation protection dosimetry. *Physics in Medicine and Biology* **49,** 5203–5216. ISSN: 0031-9155. https://iopscience.iop.org/article/10.1088/0031-9155/49/23/001 (Dec. 2004).

8. Xu, X. G., Chao, T. C. & Bozkurt, A. VIP-MAN: AN IMAGE-BASED WHOLE-BODY ADULT MALE MODEL CONSTRUCTED FROM COLOR PHOTOGRAPHS OF THE VISIBLE HUMAN PROJECT FOR MULTI-PARTICLE MONTE CARLO CALCULATIONS. *Health Physics* **78,** 476–486. ISSN: 0017-9078. http://journals.lww.com/00004032-200005000-00003 (May 2000).

9. Zubal, I. G., Harrell, C. R., Smith, E. O., Rattner, Z., Gindi, G. & Hoffer, P. B. Computerized three-dimensional segmented human anatomy. *Medical Physics* **21,** 299–302. ISSN: 00942405. http://doi.wiley.com/10.1118/1.597290 (Feb. 1994).

10. Peter, J., Gilland, D., Jaszczak, R. & Coleman, R. Four-dimensional superquadric-based cardiac phantom for Monte Carlo simulation of radiological imaging systems. *IEEE Transactions on Nuclear Science* **46,** 2211–2217. ISSN: 00189499. http://ieeexplore.ieee.org/document/819306/ (1999).

11. Zhu, J., Zhao, S., Ye, Y. & Wang, G. Computed tomography simulation with superquadrics. *Medical Physics* **32,** 3136–3143. ISSN: 00942405. http://doi.wiley.com/10.1118/1.2040727 (Sept. 2005).

12. Lee, C., Lodwick, D., Hurtado, J., Pafundi, D., Williams, J. L. & Bolch, W. E. The UF family of reference hybrid phantoms for computational radiation dosimetry. *Physics in Medicine and Biology* **55,** 339–363. ISSN: 0031-9155. https://iopscience.iop.org/article/10.1088/0031-9155/55/2/002 (Jan. 2010).

13. Segars, W., Lalush, D. & Tsui, B. *A realistic spline-based dynamic heart phantom* in *1998 IEEE Nuclear Science Symposium Conference Record. 1998 IEEE Nuclear Science Sympo-*

sium and Medical Imaging Conference (Cat. No.98CH36255) **2** (IEEE, 1999), 1175–1178. ISBN: 0-7803-5021-9. http://ieeexplore.ieee.org/xpls/abs%7B%5C_%7Dall.jsp?arnumber=775570%20http://ieeexplore.ieee.org/document/774369/.

14. Segars, W. P., Sturgeon, G., Mendonca, S., Grimes, J. & Tsui, B. M. W. 4D XCAT phantom for multimodality imaging research. *Medical Physics* **37,** 4902–4915. ISSN: 00942405. http://doi.wiley.com/10.1118/1.3480985 (Aug. 2010).

15. Veress, A. I., Segars, W. P., Weiss, J. A., Tsui, B. M. W. & Gullberg, G. T. Normal and Pathological NCAT Image and Phantom Data Based on Physiologically Realistic Left Ventricle Finite-Element Models. *IEEE Transactions on Medical Imaging* **25,** 1604–1616. ISSN: 0278-0062. http://ieeexplore.ieee.org/document/4016175/ (Dec. 2006).

16. Manohar, A., Contijoch, F., McVeigh, E. R., Colvert, G. & Schluchter, A. *LV systolic point-cloud model to quantify accuracy of CT derived regional strain* in *Medical Imaging 2019: Image-Guided Procedures, Robotic Interventions, and Modeling* (eds Fei, B. & Linte, C. A.) (SPIE, Mar. 2019), 13. ISBN: 9781510625495. https://www.spiedigitallibrary.org/conference-proceedings-of-spie/10951/2512635/LV-systolic-point-cloud-model-to-quantify-accuracy-of-CT/10.1117/12.2512635.full.

17. Yushkevich, P. A., Piven, J., Hazlett, H. C., Smith, R. G., Ho, S., Gee, J. C. & Gerig, G. User-guided 3D active contour segmentation of anatomical structures: Significantly improved efficiency and reliability. *NeuroImage* **31,** 1116–1128. ISSN: 10538119. https://linkinghub.elsevier.com/retrieve/pii/S1053811906000632 (July 2006).

18. Shi, J., Pan, C., Kong, D., Cheng, L. & Shu, X. Left Ventricular Longitudinal and Circumferential Layer-Specific Myocardial Strains and Their Determinants in Healthy Subjects. *Echocardiography* **33,** 510–518. ISSN: 07422822. http://doi.wiley.com/10.1111/echo.13132 (Apr. 2016).

19. Moore, C. C., Lugo-Olivieri, C. H., McVeigh, E. R. & Zerhouni, E. A. Three-dimensional Systolic Strain Patterns in the Normal Human Left Ventricle: Characterization with Tagged MR Imaging. *Radiology* **214,** 453–466. ISSN: 0033-8419. arXiv: NIHMS150003. http://pubs.rsna.org/doi/10.1148/radiology.214.2.r00fe17453 (Feb. 2000).

20. Kocabay, G., Muraru, D., Peluso, D., Cucchini, U., Mihaila, S., Padayattil-Jose, S., Gentian, D., Iliceto, S., Vinereanu, D. & Badano, L. P. Normal Left Ventricular Mechanics by Two-dimensional Speckle-tracking Echocardiography. Reference Values in Healthy Adults. *Revista Española de Cardiología (English Edition)* **67,** 651–658. ISSN: 18855857. http://www.revespcardiol.org/en/normal-left-ventricular-mechanics-by/articulo/90336681/%20https://linkinghub.elsevier.com/retrieve/pii/S1885585714000711 (Aug. 2014).

21. Cerqueira, M. D., Weissman, N. J., Dilsizian, V., Jacobs, A. K., Kaul, S., Laskey, W. K., Pennell, D. J., Rumberger, J. A., Ryan, T. & Verani, M. S. Standardized Myocardial Segmentation and Nomenclature for Tomographic Imaging of the Heart. *Circulation* **105,** 539–

542. ISSN: 0009-7322. https://www.ahajournals.org/doi/10.1161/hc0402.102975 (Jan. 2002).

22. Qianqian Fang & Boas, D. A. *Tetrahedral mesh generation from volumetric binary and grayscale images* in *2009 IEEE International Symposium on Biomedical Imaging: From Nano to Macro* (IEEE, June 2009), 1142–1145. ISBN: 978-1-4244-3931-7. http://ieeexplore.ieee.org/document/5193259/.

23. Moore, B. & Prasad Dasi, L. Quantifying left ventricular trabeculae function - application of image-based fractal analysis. *Physiological Reports* **1,** e00068. ISSN: 2051817X. http://www.ncbi.nlm.nih.gov/pubmed/24303149%20http://doi.wiley.com/10.1002/phy2.68%20http://www.pubmedcentral.nih.gov/articlerender.fcgi?artid=PMC3831892 (Sept. 2013).

24. Manohar, A., Rossini, L., Colvert, G., Vigneault, D. M., Contijoch, F., Chen, M. Y., del Alamo, J. C. & McVeigh, E. R. Regional dynamics of fractal dimension of the left ventricular endocardium from cine computed tomography images. *Journal of Medical Imaging* **6,** 1. ISSN: 2329-4302. https://www.spiedigitallibrary.org/journals/journal-of-medical-imaging/volume-6/issue-04/046002/Regional-dynamics-of-fractal-dimension-of-the-left-ventricular-endocardium/10.1117/1.JMI.6.4.046002.full (Nov. 2019).

25. Bade, R., Haase, J. & Preim, B. *Comparison of Fundamental Mesh Smoothing Algorithms for Medical Surface Models* in *SimVis* **6** (2006), 289–304.

Chapter 3

Temporal resolution of estimating timing of LV mechanics with 4DCT

The accurate and reproducible estimation of timing of LV mechanics may be beneficial in the successful planning and management of cardiac resynchronization therapy (CRT). We sought to demonstrate the viability of a 4DCT imaging system to estimate mechanical activation times of LV wall motion with high fidelity. An anthropomorphically accurate in-silico LV phantom with programmed septal-lateral wall dyssynchrony was developed. Twenty-six temporal phases of the in-silico phantom were used to sample the cardiac cycle of 1 second. For each of the 26 phases, 1 cm thick axial slabs emulating axial CT image volumes were extracted, 3D printed, and imaged using a commercially available CT scanner. A continuous dynamic sinogram was synthesized by blending sinograms from these static phases; the synthesized sinogram emulated the sinogram that would be acquired under true continuous phantom motion. Using the synthesized dynamic sinogram, images were reconstructed at 70 ms intervals spanning the full cardiac cycle; these

images exhibited expected motion artifact characteristics seen in images reconstructed from real dynamic data. The motion corrupted images were then processed with a novel motion correction algorithm (ResyncCT) to yield motion corrected images. Five pairs of motion uncorrected and motion corrected images were generated, each corresponding to a different starting gantry angle (0 to 180 degrees in 45 degree increments). Two line profiles perpendicular to the endocardial surface were used to sample local myocardial motion trajectories at the septum and the lateral wall, respectively. The mechanical activation time of wall motion was defined as the time at which the endocardial boundary crossed a fixed position defined on either of the two line profiles while moving towards the center of the LV during systolic contraction. The mechanical activation times of these myocardial trajectories estimated from the motion uncorrected and the motion corrected images were then compared with those derived from the static images of the 3D printed phantoms (ground-truth). Precision of the timing estimates was obtained from the five different starting gantry angle simulations. The range of estimated mechanical activation times observed across all starting gantry angles was significantly larger for the motion uncorrected images than the motion corrected images. The promising results reported in this chapter highlight the potential utility of 4DCT in estimating the timing of mechanical events of interest for CRT guidance.

3.1 Background

The advancements in 4DCT technology have made it a promising modality for the diagnosis and management of various cardiac diseases. One such application for these images is predicting response to CRT, which is a medical procedure for treating heart failure patients with mechanical dyssynchrony of the left ventricle. For many patients, this treatment is highly effective; unfortunately, treatment response rate is currently a serious limitation, with 30-50%

of patients not receiving much benefit as a result of their CRT procedure [1]. A great deal of research has been done into how to use echocardiography or cardiac magnetic resonance (CMR) imaging to guide treatment decisions, but such efforts have not produced a robust solution due to poor performance from echo [2, 3] and the complexity and limited applicability of MR techniques (e.g., 28% of CRT candidates already have RV pacing in place, which limits the use of CMR [4]).

Recent studies have determined the benefits of 4DCT in estimating mechanical dyssynchrony and guiding optimal lead placement. Hoffmann and colleagues demonstrated the utility of multi-detector CT systems to identify differences in the extent of left ventricular (LV) dyssynchrony between patients in heart failure and age-matched controls [5]. More recently, they determined the ability to predict 2-year major adverse cardiac events (MACE) using dual-source CT. They also showed that leads placed on sites with maximal wall thickness were associated with less MACE ($p < 0.01$) [6]. Behar et al. used CT to determine the epicardial vein for targeting optimal lead placement [7]. A CT-derived endocardial strain metric called SQUEEZ [8] was used to identify regions of scar tissue and regions of latest mechanical activation. They reported that pacing at a site determined optimal by CT-SQUEEZ correlated with higher clinical response rates than those paced in non-optimal regions (90% vs 60%).

However, previous studies have not addressed a major limitation in measuring temporal events with CT: the 'false dyssynchrony' artifact [9]. The temporal resolution of 4DCT is complex; motion artifacts seen in reconstructed CT images are due to the combined effect of gantry position as a function of time and the relative direction of wall motion [10, 11]. Edge locations in reconstructed CT images are updated every time the x-ray beam is tangent to the particular edge; therefore, depending on their orientation, different edges are updated at different points in time in a continuous 4DCT movie, giving the false impression of dyssynchronous contraction

(Sec. 3.2.4 provides further insight into the source of the false dyssynchrony artifact). These artifacts are usually not crucial in the assessment of global LV function; however, they impede the ability to accurately and precisely measure mechanical activation times at different locations on the LV wall. The accurate evaluation of activation times of wall motion and LV dyssynchrony provides critical information in the optimal planning and management of CRT [12, 13].

Thus, the objective of this study was to perform the first quantitative evaluation of the accuracy and precision of estimating mechanical activation times [14, 15] of LV wall motion using 4DCT. To serve as ground-truth, we developed an anthropomorphically accurate in-silico LV phantom with programmable dyssynchrony and used the phantom to understand and improve temporal motion artifacts seen in 4DCT images. Based on this study, guidance for estimating mechanical activation times of LV wall motion was obtained.

3.2 Methods

3.2.1 Dyssynchronous LV Phantom Development

Image acquisition, image segmentation, and mesh extraction

A CT image of the end diastolic phase of a human LV was used as the baseline for phantom development. The image was acquired using a 256 detector-row (Revolution CT, General Electric Healthcare, Chicago, IL) scanner at the University of California San Diego using retrospective electrocardiogram gating with inspiratory breath hold. The subject (age: 45 years; sex: female) was scanned for one complete cardiac cycle (tube current: 148 mA; kVp: 80kV) and the end diastolic phase was reconstructed at 0% of the R-R phase into a 512 x 512 x 256 grid. The image had a pixel spacing of 0.41 mm in the x-y plane and a slice thickness of 0.625 mm in z.

The reconstruction field of view diameter was 209 mm and the 'Standard' reconstruction kernel (name of the kernel on the GE Revolution CT scanner) was used. Neither subject enrollment, image acquisition, nor image reconstruction was done for the purpose of this particular study; the subject was scanned, and images were acquired and reconstructed as per standard clinical protocols established at the center. The images of the subject were retrospectively used in this study in accordance with an IRB approved protocol.

A mesh defining the LV endocardium was extracted in a manner similar to that described by Manohar et al. [16]. First, the end diastolic phase of the LV was segmented using the active contour region growing module in ITK-SNAP v3.6.2 [17] (thresholding type = high pass; threshold = 360 Hounsfield units (HU); smoothness = 10; seed radius = 10; all other parameters were set as default). The segmentation was then imported into MATLAB (MathWorks Inc.) and resampled to an isotropic resolution of 0.5 mm in x, y, and z dimensions. Finally, a mesh was extracted from the resampled segmentation using the *isosurface* built-in MATLAB routine which comprised of 98911 faces and 49627 mesh points. Figure 3.1 illustrates the process outlined above.

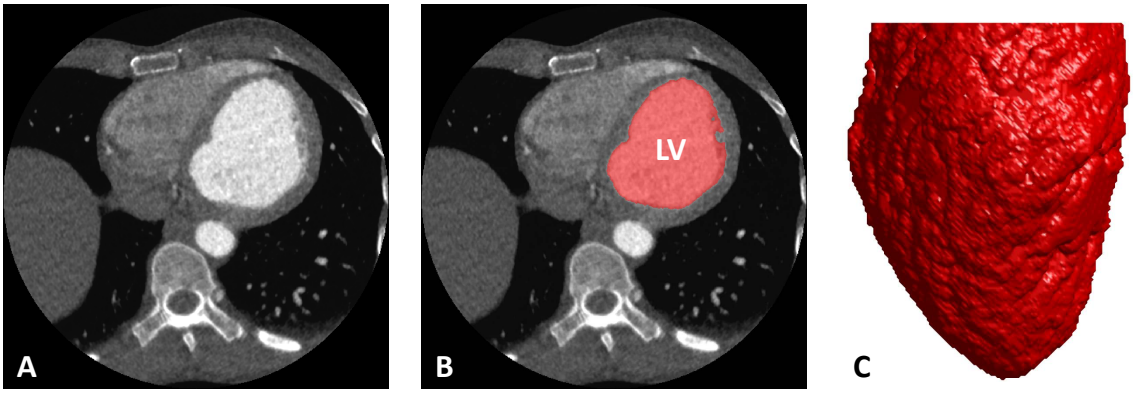

Figure 3.1: Image segmentation and mesh extraction. (A) Axial slice of the CT image. (B) Axial slice with the LV blood volume segmentation overlaid in red. (C) 3D rendering of the extracted LV endocardial mesh, looking at the lateral wall with the anterior wall to the left, and the inferior wall to the right.

Displacement functions

Dyssynchrony was programmed into the in-silico LV phantom by prescribing displacements to the extracted mesh points. These displacements were designed to achieve the desired endocardial strains as a function of both endocardial location and time across the cardiac cycle. Two strains were simulated: longitudinal strain (ϵ_{ll}) as a function of only time (t) across the cardiac cycle and circumferential strain (ϵ_{cc}) as a function of both time (t) and endocardial azimuthal location (θ). The strain functions used in this study were modeled based on realistic in-vivo strains reported by Helm et al. [18] and Delgado et al. [19] as well as on those derived from computer simulations using the CircAdapt model [20].

A time dependent gradient in circumferential strain in the azimuthal direction (θ) was programmed to simulate an activation delay in contraction between the in-silico phantom's septal ($\theta = \pi$) and lateral walls ($\theta = 0$); this was done to emulate the activation delay that is clinically observed in patients with a left bundle branch block (LBBB) or right ventricular (RV) apical pacing [18, 19]. This gradient was achieved by defining one strain vs time curve for the lateral wall at $\theta = 0$ ($\epsilon_{cc_{lateral}}$) and another strain vs time curve for the septum at $\theta = \pi$ ($\epsilon_{cc_{septal}}$); the circumferential strain at all other endocardial locations $0¡|\theta|¡\pi$ was a linearly interpolated value between the two defined strains at $\theta = 0$ and $\theta = \pi$. Figure 3.2A shows the designed longitudinal (solid blue) and circumferential (dashed red – lateral wall; dotted green – septum) strains as a function of time across the cardiac cycle. The R-R interval of the simulated cardiac cycle was set to 1 second.

The displacement functions were prescribed to the LV mesh points in the cardiac frame of reference, which was defined as the coordinate system in which the LV long axis was parallel to the z-axis (Fig. 3.2B). The mesh points were transformed from a cartesian coordinate

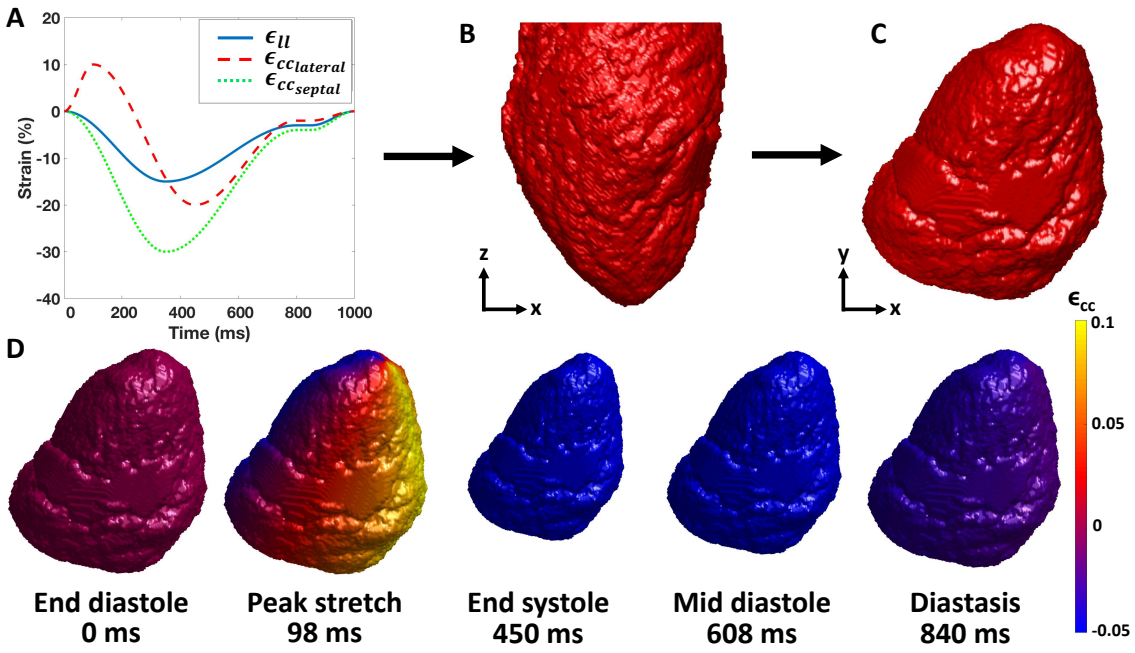

Figure 3.2: Simulation of LV dyssynchrony. (A) Longitudinal (ϵ_{ll} - solid blue) and circumferential ($\epsilon_{cc_{lateral}}$) - dashed red; $\epsilon_{cc_{septal}}$ – dotted green) strain curves as a function of time across the cardiac cycle. The R-R interval of the simulated cardiac cycle was set to 1 second. (B) 3D rendering of the end diastolic LV mesh in the cardiac frame of reference with the LV long axis parallel to the z axis. The lateral wall is in view with the anterior wall to the left and the inferior wall to the right. (C) 3D rendering of the end diastolic LV mesh rotated back to its original orientation in the scanner frame of reference. The inferior wall is in view with the septum on the left and the lateral wall on the right, looking from the patient's feet up towards the head. (D) 3D renderings of the analytically deformed meshes of the dyssynchronous LV in-silico phantom at 5 phases of the cardiac cycle with regional circumferential strain values mapped onto the endocardial surface. Blue represents endocardial contraction and yellow represents endocardial stretch. The orientation of the LV is the same as in 2.2C

.

system (x, y, z) to a cylindrical coordinate system (r, θ, z), with the origin set to the LV mesh centroid. Displacements were then prescribed to the mesh points (r, θ, z) according to the following equations:

$$r(\theta, t) = r(\theta, 0) \times (1 + \epsilon_{cc}(\theta, t)), \tag{3.1}$$

$$z(t) = z_0 + (z(0) - z_0) \times (1 + \epsilon_{ll}(t)), \tag{3.2}$$

where t is time across the cardiac cycle and $t = 0$ represents end diastole, z_0 is the fixed apical z coordinate of the LV mesh, and $\epsilon_{cc}(\theta, t)$ is the circumferential strain at time t for a point with an azimuthal coordinate of $0 \leq |\theta| \leq \pi$, given by the equation:

$$\epsilon_{cc}(\theta, t) = (\epsilon_{cc_{septal}}(t) - \epsilon_{cc_{lateral}}(t) \cdot \frac{|\theta|}{\pi} + \epsilon_{cc_{lateral}}(t), \tag{3.3}$$

After prescribing the displacement functions, the mesh points (r, θ, z) were transformed back to the cartesian coordinate system (x, y, z). The LV mesh was then rotated back to its original orientation in the scanner frame of reference as shown in Fig. 3.2C. Figure 3.2D shows analytically deformed meshes of the in-silico phantom at 5 phases of the cardiac cycle with regional ϵ_{cc} values mapped onto the endocardial surface (blue represents contraction and yellow represents stretch).

3.2.2 3D Printing & CT Imaging of the Dyssynchronous LV Phantom

Twenty-six phases of the dyssynchronous LV in-silico phantom were chosen to sample the simulated cardiac cycle of 1 second. The first phase was at 0 ms and the 26^{th} phase was at 975 ms of the simulated cardiac cycle. The 26 phases were chosen with variable time intervals such that no single mesh point had more than 2 mm displacement between any two consecutive phases. These 26 phases were sufficient to sample the programmed motion of the phantom across the simulated cardiac cycle (see Appendix B).

Generation of axial slabs and 3D printing

Axial slabs of 1 cm in thickness fixed in the scanner z-direction, were extracted from each of the 26 phases of the dyssynchronous LV in-silico phantom (Fig. 3.3A). The fixed axial slabs emulated clinical axial CT image volumes with the phantom's tissue moving in and out of the axial plane as it was programmed to contract and relax. The particular slab shown in Fig. 3.3A was chosen because it sampled both the delayed contracting lateral wall and the earlier contracting septum. These in-silico axial slabs were 3D printed to create physical phantoms. Each physical phantom, representing a particular phase of the cardiac cycle, was printed in the shape of a cylinder with a hollow LV cavity in the center using a Form 3 stereolithography printer (Formlabs Inc., Somerville, MA). The printing material used was a proprietary clear photopolymer resin (FLGPCL04) and the central LV cavity was filled with an iodinated non-ionic radiocontrast agent (10% by volume solution of Visipaque 320, General Electric Healthcare, Chicago, IL). Figure 3.3B shows the 26 3D printed phantom cylinders labeled with their corresponding time delays in ms after end diastole. Figure 3.3C shows the positioning holder and an example 3D printed phantom (corresponding to the 98 ms phase) positioned in the CT scanner; tabs on the side of each phantom locked each phantom into position to maintain spatial alignment over the time frames.

CT Imaging

A 256 detector-row (Revolution CT, General Electric Healthcare, Chicago, IL) clinical CT scanner was used to image the 26 3D printed phantom cylinders. Each cylinder was imaged for a total of 450 ms under 100 kVp, 350 mA, and small focal spot tube settings. The raw data for each scan was saved using the standard archiving software on the scanner. Each image was

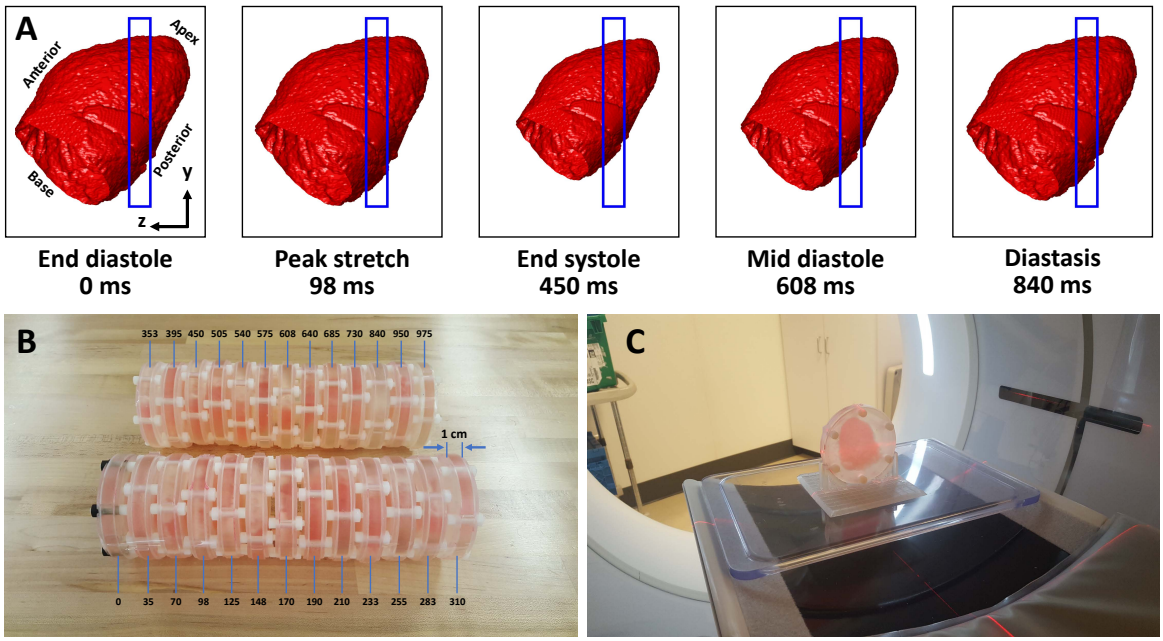

Figure 3.3: 3D printing and CT imaging of the 1 cm thick axial slabs of the dyssynchronous LV phantom. (A) Right sagittal views of the meshes of the dyssynchronous LV in-silico phantom at 5 phases of the cardiac cycle. The blue rectangle shows the 1 cm axial slab fixed in space; for each phase of the cardiac cycle, mesh points within that slab were extracted. (B) Stack of the 26 3D printed 1 cm thick cylinders of the dyssynchronous LV phantom. Each 3D printed phantom cylinder represents a particular phase of the cardiac cycle and is labeled with its corresponding time delay in ms after end diastole. (C) The 98 ms phantom cylinder positioned in the CT scanner for imaging. The phantom was locked into position using a holder fixed onto the scanner table.

.

reconstructed into a 512 x 512 x 128 grid with pixel spacings of 0.49 mm in the $x-y$ plane and a slice thickness of 0.625 mm in z. The 'Standard' reconstruction kernel (name of the kernel on the GE Revolution CT scanner) was used with a reconstruction field of view diameter of 250 mm. The HU values of the photopolymer resin and the contrast solution were 120 $\pm$ 15 and 1065 $\pm$ 30, respectively. These images, referred to hereafter as the "static" images, served as the motion artifact free ground-truth images of the dyssynchronous LV phantom, sampling the simulated cardiac cycle in 26 phases from 0 ms to 975 ms. Figure 3.4 shows the CT reconstructed images of the 3D printed phantom cylinders at 5 phases of the cardiac cycle.

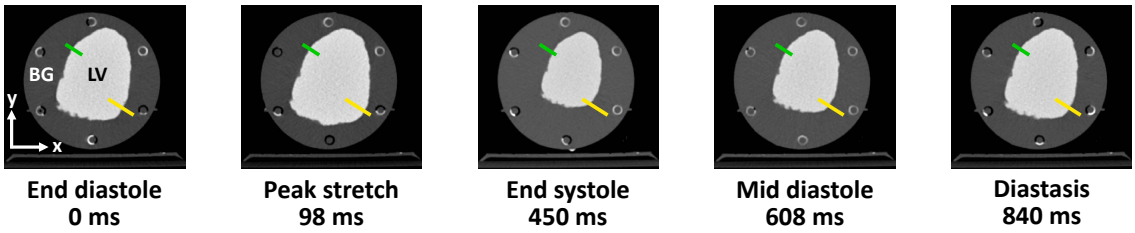

Figure 3.4: CT reconstructed images of the 3D printed phantom cylinders at 5 phases of the cardiac cycle. The circular gray background is the photopolymer resin (printing material). The LV cavity is filled with an iodinated radiocontrast solution. The green and yellow lines represent the septal wall and the lateral wall m-mode sampling lines, respectively. LV: left ventricle; BG: background resin.

.

3.2.3 Dynamic Raw Data Synthesis & Image Reconstructions

The raw data for each of the 26 images acquired as described above was saved using the standard archiving software on the scanner. These individual raw datasets, each representing a Static phase of the 3D printed phantom, were first converted to sinograms that can be reconstructed (data prep). The prepped sinograms were then used to create a synthetic dynamic sinogram which emulated the sinogram that would be acquired if the dyssynchronous phantom contracted and relaxed continuously in real time.

The first step in the synthesis of the dynamic sinogram was the extraction of a single full scan view range (360°) from each prepped Static sinogram. The views were then circularly shifted to align the starting view angles. In order to ensure there was no discontinuity at the wrap around point, the extracted view range was initially larger than one rotation and a gradual linear blending function was employed to combine the earliest and latest views together.

Given a reference view angle (β_c) and a corresponding reference time (t_c), one can compute the view angle positions that correspond exactly to each Static phase (for each of multiple cardiac cycles) as follows:

$$\beta_{n+26N} = \beta_c + (t_n - t_c + 1000N) \cdot \omega, \tag{3.4}$$

where N is an integer that indexes the cardiac cycle (e.g. -1 for the previous cardiac cycle, 0 for the current cycle, 1 for the next cardiac cycle), n is an integer from 1 to 26 indicating the phase index, and ω is the gantry rotation speed in radians per millisecond. A dynamic sinogram (D_{β_c,t_c}) was then computed from the Static sinograms (S_i) using linear interpolation at each view angle based on the two nearest phases, as follows:

$$D_{\beta_c,t_c}(\beta,\gamma,\alpha) = (1 - w(\beta)) \cdot \hat{S}_{i(\beta)}(\hat{\beta},\gamma,\alpha) + w(\beta) \cdot \hat{S}_{i(\beta)+1}(\hat{\beta},\gamma,\alpha), \tag{3.5}$$

where β is the view angle, γ is the fan angle, α is the cone angle, $w(\beta)$ is a linear interpolation weight in the range [0,1), given by the following equation:

$$w(\beta) = \frac{\beta - \beta_{i(\beta)}}{\beta_{i(\beta)+1} - \beta_{i(\beta)}}, \tag{3.6}$$

and $i(\beta)$ is defined as the unique index i such that

$$\beta_i \leq \beta < \beta_{i+1}, \tag{3.7}$$

Additionally, $\hat{S}_i$ and $\hat{\beta}$are defined via the modulo operator as follows:

$$\hat{S}_i(\beta,\gamma,\alpha) = S_{imod26}(\beta,\gamma,\alpha) \tag{3.8}$$

$$\hat{\beta} = \beta mod 2\pi, \tag{3.9}$$

In order to provide a multi-phase reconstruction series that covered the entire heart cycle (and to be able to apply our motion correction algorithm), we generated dynamic sinograms that covered a time period slightly larger than one heart cycle. Reconstructions were performed using the scanner reconstruction software (GE Revolution CT) at 90-degree intervals (70 ms intervals for a gantry rotation speed of 280 ms), yielding 14 phases that sampled the full cardiac cycle from 0 ms to 980 ms. The resulting images clearly manifested the expected motion artifact characteristics seen in images reconstructed from real dynamic data, including "double-wall" and "stationary-wall" artifacts and distortions that rotate in concert with the orientation of the gantry angle [**Pack**]. Intra window motion is included in the linear interpolation of sinogram data during the synthetic sinogram creation. The difference between the continuous sinogram and the interpolated sinogram yields artifacts in the reconstructed images that are imperceptible compared with the larger "double-wall" and "stationary-wall" artifacts [21]; these larger artifacts are the primary sources of error in the estimation of mechanical activation times of wall motion.

The motion-corrupted images, referred to hereafter as the "Uncorrected" images, were then processed with a novel motion correction algorithm called ResyncCT [**Pack**] to produce motion corrected images at the same 14 phases of the cardiac cycle as that of the Uncorrected images. ResyncCT is a new cardiac CT motion correction algorithm that leverages the power of conjugate pairs of partial angle reconstruction images for motion estimation and motion compensation. The motion corrected images are referred to hereafter as the "ResyncCT" images. This entire process was repeated for five different starting gantry angles by using a reference time of zero ($t_c = 0$) and reference view angles of:

$$\beta_c(k) = k \cdot \frac{\pi}{4}, \tag{3.10}$$

where k is an integer from 0 to 4, representing the five different starting gantry angles (0, 45, 90, 135, and 180 degrees).

3.2.4 M-mode Imaging

The effect of CT motion artifacts on the estimate of the position of the endocardium was quantified by sampling endocardial wall positions as a function of time across the cardiac cycle in a manner similar to ultrasound m-mode imaging [22, 23]. The lateral wall m-mode line (shown by the yellow line in Fig. 3.4) was placed close to the site of programmed latest activation. The septal wall m-mode line (shown by the green line in Fig. 3.4) was placed at a point of earlier activation on the septum.

Endocardial wall positions as a function of time were sampled along the m-mode lines for each of the Static, the Uncorrected, and the ResyncCT images. These m-mode images were then up-sampled via cubic interpolation by a factor of 10 to achieve sub-pixel resolution, thereby reducing the effects of pixel discretization. The endocardial boundary (edge) was detected from each m-mode image by applying a threshold of 530 HU, which was the optimal threshold for LV blood volume segmentation as determined by Otsu's method [24].

The first three rows of Fig. 3.5 (Figs. 3.5A-C) show the Uncorrected images sampled at three phases of the cardiac cycle; the full set of reconstructions (not shown) span the cardiac cycle from 0 ms to 980 ms in 70 ms intervals. Each column corresponds to a simulated starting gantry angle: 0°, 45°, 90°, 135°, and 180°from left to right. Figure 3.5D shows the lateral wall m-mode images sampled at the endocardial wall location shown by the yellow line. In Figs. 3.5A-C, the semi-circle represents the trajectory of the x-ray source (white object) as it rotates in the counterclockwise direction (for 0°, the source trajectory is centered at 12 o'clock; for 90°, the

source is centered at 9 o'clock). The green part of the trajectory represents the new "updated" views used in the reconstruction of a particular time frame of the object, assuming an image is reconstructed every 70ms (with a 280 ms gantry rotation time). The red part of the trajectory represents views used in the reconstruction of a time frame of the object that are shared with its previous time frame. Hence, edges of the object parallel to the rays within the green views are updated in the new time frame, while edges parallel to the rays within the red views remain unchanged from the previous time frame. This is the source of the false dyssynchrony artifact [**Pack**, 9].

3.2.5 Dynamics of Endocardial Boundary Motion During Systole

The septal and the lateral wall m-mode images were used to investigate the artifacts in the measured dynamics of endocardial boundary motion during systole. The endocardial boundary was detected from each of the m-mode images derived from the Static, the Uncorrected, and the ResyncCT images. The Uncorrected and the ResyncCT images had the endocardial boundaries sampled for 5 simulated starting gantry angles. The endocardial boundary positions derived from the Static images served as the ground-truth for error estimation; these boundary positions were not dependent on starting gantry angle.

For a pre-determined "critical" position along the length of the m-mode line, the time at which the endocardial boundary crossed this position during systole was estimated. The critical position and the time at which the endocardial boundary crossed that position are referred to hereafter as the mechanical activation position (MAP) and the mechanical activation time (MAT), respectively. The motivation behind estimating this value was to assess the accuracy and precision of measuring mechanical activation times at local regions of the heart wall from

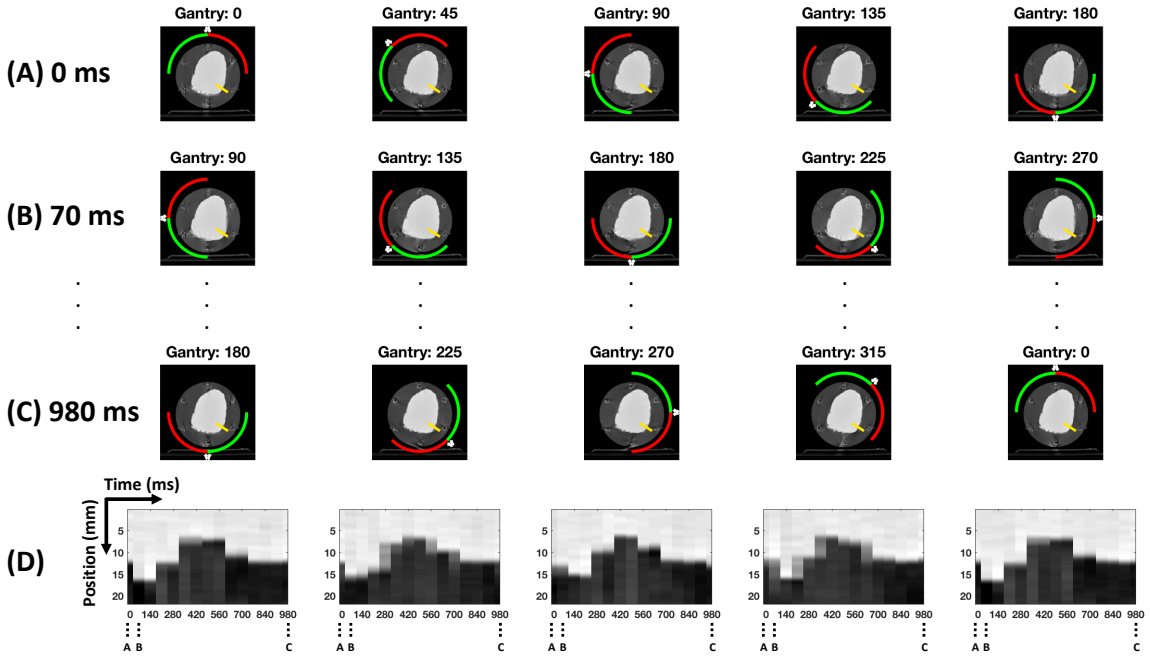

Figure 3.5: Simulated CT image acquisition, reconstruction, and m-mode imaging. Each column corresponds to a simulated starting gantry angle: 0°, 45°, 90°, 135°, and 180°from left to right, where the angular value of the source at the center of the acquisition is used to label each trajectory. The semi-circles shown in rows A-C represent the trajectory of the x-ray source (white object) as it rotates in the counterclockwise direction from 0°at 12 o'clock to 180°at 6 o'clock. The green part of the trajectory represents new views acquired that are used in the reconstruction of a particular time frame of the object. The red part of the trajectory represents views used in the reconstruction of a time frame of the object that are shared with its previous time frame. (A-C) Reconstructions of the Uncorrected images of the LV phantom at 3 of the 14 total phases of the cardiac cycle for a set of simulated starting gantry angles (columns). (D) Lateral wall m-mode images sampled at the endocardial lateral wall location shown by the yellow line. For each tile, the y axis is endocardial position along the length of the m-mode line in mm and the x axis is time across the cardiac cycle in ms; the motion of the wall is shown as the change in position of the boundary between the bright blood and the darker wall.

.

4DCT images, both with and without motion correction. MATs were estimated for all three classes of images: the Static, the Uncorrected, and the ResyncCT images. The MATs estimated from the Uncorrected (T_U) and the ResyncCT (T_R) images were compared with those estimated from the Static images (T_0; ground-truth). Figure 3.6 illustrates an example estimation of the MATs (T_0, T_U, and T_R) for a defined MAP (y_0) along the length of the lateral wall m-mode line.

This process was repeated for a series of MAPs defined in intervals of 0.5 mm along the lengths of both the septal wall and the lateral wall m-mode lines. For the lateral wall, 11 positions between 9 and 14 mm were defined along the length of the m-mode line, while 8 positions between 7 and 10.5 mm were defined for the septal wall m-mode line. These positions were chosen such that they sampled the full range of systolic endocardial boundary motion at both the lateral wall and the septal wall m-mode locations.

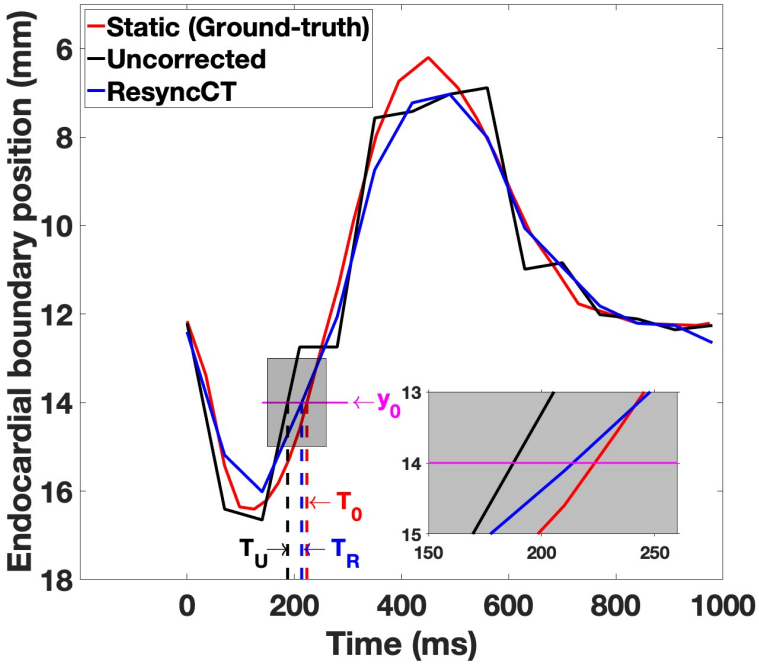

Figure 3.6: Estimation of mechanical activation times (MATs) at a defined mechanical activation position (MAP). For a defined MAP (y_0) along the length of the lateral wall m-mode line, the times at which the Static (T_0 - ground truth; red), the Uncorrected (T_U; black), and the ResyncCT (T_R; blue) derived endocardial boundaries crossed the MAP ($=y_0$) were estimated as their respective mechanical activation times (MAT).

At each MAP, the range of estimated MATs observed over all gantry angles was calculated for both the Uncorrected and the ResyncCT images. The distribution of ranges in MATs across all defined MAPs was then tested for statistically significant difference between the Uncorrected and the ResyncCT images using the two-sample t-test. A p-value of < 0.05 was considered

significant.

3.2.6 Time to Maximal Outward Displacement

The programmed displacement functions made the lateral wall, at the location sampled by the lateral wall m-mode line, reach its maximum outward position at the 123 ms time point of the cardiac cycle; this was the ground-truth value of the time to maximal outward displacement (TMOD) of the late activated lateral wall. This time is a possible parameter for the characterization of mechanical activation delay and has been previously used in tagged magnetic resonance imaging (MRI) studies of dyssynchrony [14, 15]. The TMOD calculation was performed only for the lateral wall m-mode images.

The TMOD values of the lateral wall endocardial boundaries derived from the Uncorrected and the ResyncCT images were measured by fitting a second-degree polynomial to the first 5 time points (0, 70, 140, 210, 280 ms; Fig. 3.7) of the endocardial boundary positions according to the model:

$$y = a_0 + a_1 t + a_2 t^2, \tag{3.11}$$

where y is the position of the endocardial boundary in mm and t is time across the cardiac cycle in ms. TMOD was then calculated as the extremum of the fitted function, given by the equation:

$$TMOD = f(a_1, a_2) = \frac{-a_1}{2a_2}, \tag{3.12}$$

The covariance matrix of the coefficients of the polynomial fit was estimated according to the following equation in order to obtain the confidence intervals of the fitted TMOD value:

$$Cov = \frac{(R^{-1} \times R^{-1\prime}) \times normr^2}{df}, \tag{3.13}$$

where Cov is the covariance matrix, R is the triangular R factor from a QR decomposition of the Vandermonde matrix of the input query points, $normr$ is the norm of the residuals, and df is the number of degrees of freedom. The variance of the fitted TMOD value was then estimated according to the following equation:

$$Var[f(a_1, a_2)] = \sum_{i=1}^{2} f_i'(a_1, a_2)^2 \times Var[a_i] + 2 \sum_{i>j} f_i'(a_1, a_2) \times f_j'(a_1, a_2) \times Cov[a_i, a_j], \tag{3.14}$$

where Var is the variance. A TMOD value was estimated for each starting gantry angle simulation for both the Uncorrected and the ResyncCT images, yielding a total of 10 TMOD values (5 Uncorrected and 5 ResyncCT).

The standard deviation ($\pm 1\sigma$) around each TMOD value was calculated as the square root of the variance derived from the polynomial fits. The distribution of ranges ($=2\sigma$) in the TMOD estimates observed over all 5 starting gantry angles was then tested for statistically significant difference between the Uncorrected and the ResyncCT images using the two-sample t-test. A p-value of < 0.05 was considered significant.

3.3 Results

3.3.1 Septal Wall & Lateral Wall M-Mode Images

Figure 3.8 shows the lateral wall m-mode images as a function of time across the cardiac cycle. Each column corresponds to a simulated starting gantry angle; 0°through 180°from left to

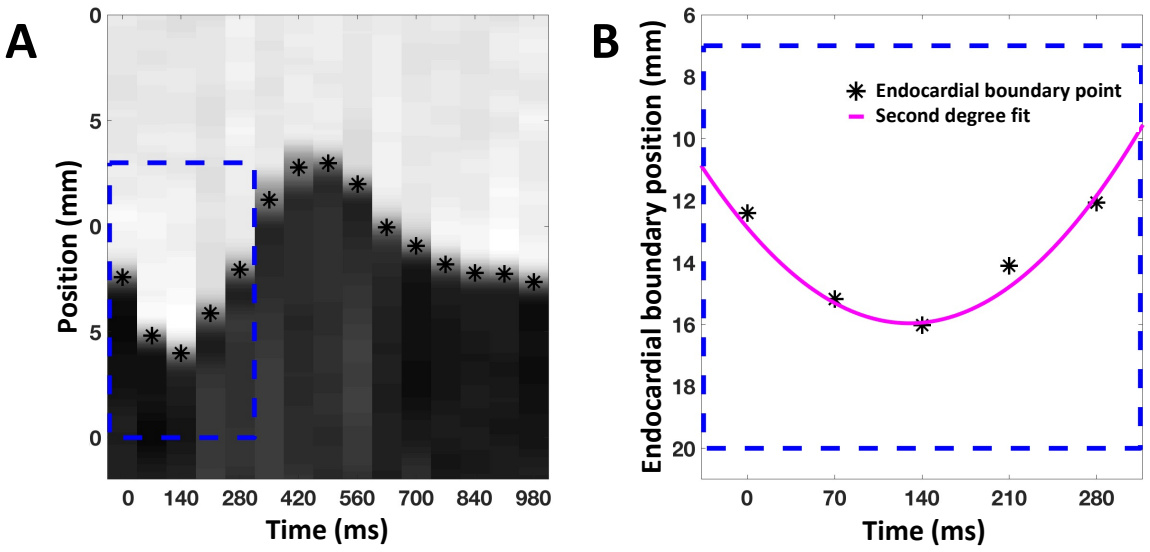

Figure 3.7: Estimation of the time to maximal outward displacement (TMOD). (A) Lateral wall m-mode image derived from the 0°starting gantry angle ResyncCT image. The dashed blue box is the highlighted region of interest shown in 7B. The black asterisks correspond to the endocardial boundary positions. (B) Second degree polynomial fit (magenta) to the first 5 time points of the endocardial boundary positions used in the estimation of TMOD.

right. The m-mode images were sampled at 70 ms regular intervals across the cardiac cycle from 0-980 ms. Figures 3.8A and 3.8C show the m-mode images derived from the Uncorrected images while Figs. 3.8B and 3.8D show the m-mode images derived from the ResyncCT images. Figures 3.8A-B show the grayscale images and Figs. 3.8C-D show the binarized images after applying a threshold of 530 HU. The overlaid red dots correspond to the ground-truth endocardial boundary positions (derived from the Static images) across the cardiac cycle sampled by the lateral wall m-mode line.

Similarly, Fig. 9 shows the septal wall m-mode images as a function of time across the cardiac cycle for the 5 simulated starting gantry angles. Figures 9A and 9C show the m-mode images derived from the Uncorrected images and Figs. 9B and 9D show the m-mode images derived from the ResyncCT images. Figures 9A-B show the grayscale images and Figs. 9C-D show the binarized images after applying a threshold of 530 HU. The overlaid red dots correspond

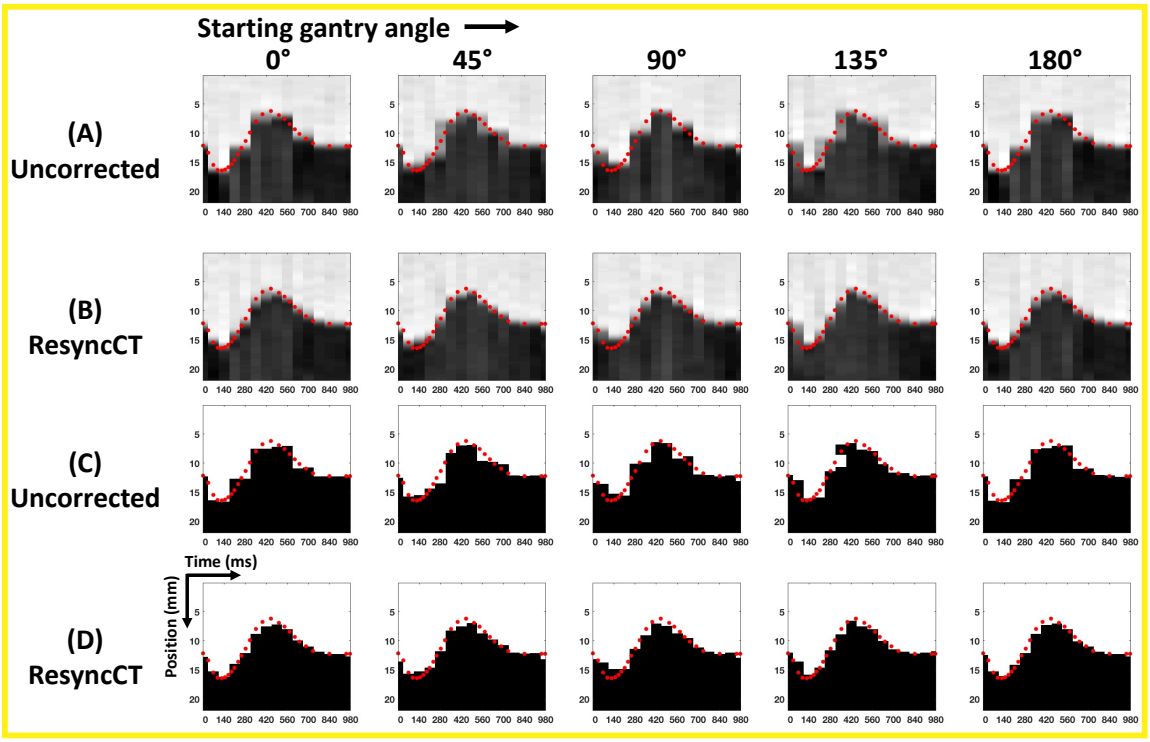

Figure 3.8: Lateral wall m-mode images of the endocardium as a function of time across the cardiac cycle for the 5 simulated starting gantry angles: 0°, 45°, 90°, 135°, and 180°(A-B) Grayscale m-mode images derived from (A) the Uncorrected and (B) the ResyncCT images. (C-D) Binarized m-mode images derived from (C) the Uncorrected and (D) the ResyncCT images, showing the endocardial boundary positions as defined by the images. The red dots correspond to the ground-truth endocardial boundary positions across the cardiac cycle sampled by the lateral wall m-mode line from the Static images. For each tile, the y-axis is position along the length of the m-mode line in mm and the x-axis is time across the cardiac cycle in ms.

to the ground-truth endocardial boundary positions (derived from the Static images) across the cardiac cycle sampled by the septal wall m-mode line.

It is clear from Fig. 8 and Fig. 9 that the ground-truth endocardial boundary positions (red dots) are closer to the boundaries observed in the ResyncCT corrected images. This difference in accuracy is also summarized in Fig. 10 below. It is also clear that the starting gantry angle has a significant effect on the positions of the endocardial boundary as a function of time across the cardiac cycle.

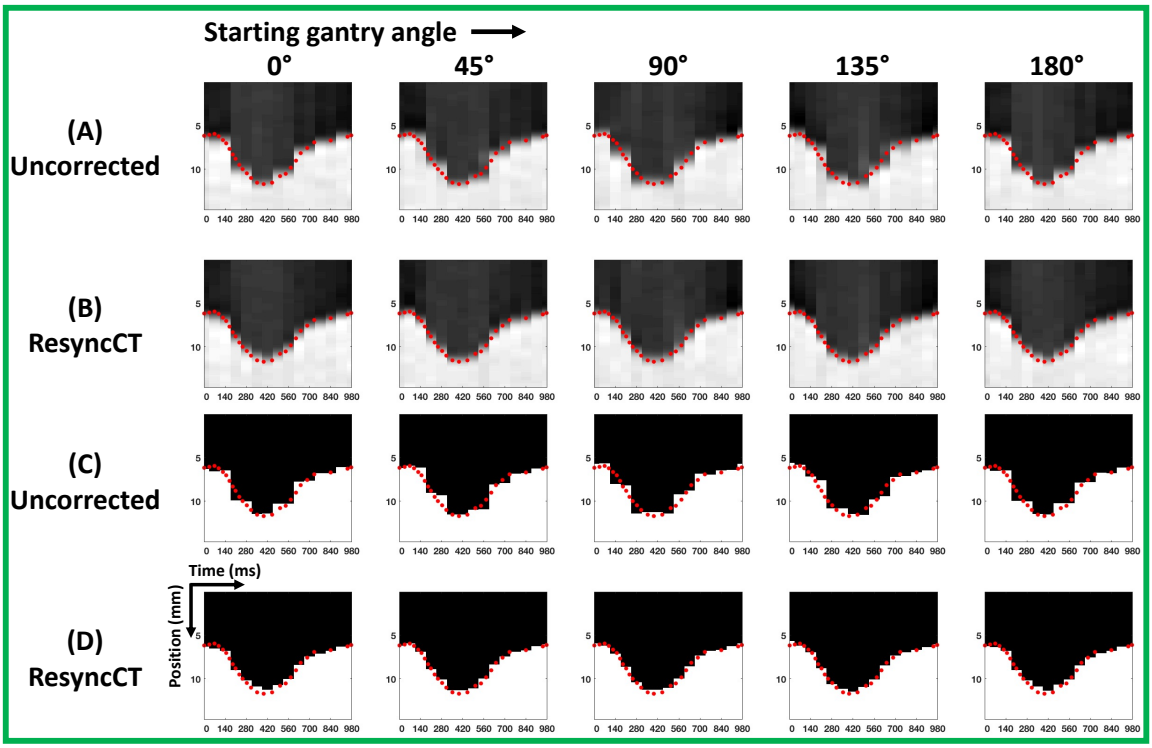

Figure 3.9: Septal wall m-mode images of the endocardium as a function of time across the cardiac cycle for the 5 simulated starting gantry angles: 0°, 45°, 90°, 135°, and 180°(A-B) Grayscale m-mode images derived from (A) the Uncorrected and (B) the ResyncCT images. (C-D) Binarized m-mode images derived from (C) the Uncorrected and (D) the ResyncCT images, showing the endocardial boundary positions as defined by the images. The red dots correspond to the ground-truth endocardial boundary positions across the cardiac cycle sampled by the septal wall m-mode line from the Static images. For each tile, the y-axis is position along the length of the m-mode line in mm and the x-axis is time across the cardiac cycle in ms.

3.3.2 Dynamics of Endocardial Boundary Motion During Systole

Figure 3.6 in Sec. 3.2.5 describes an example estimation of the MATs for a defined MAP along the length of the lateral wall m-mode line; the numerical values associated with Fig. 6 are specified here. For a MAP of 14 mm (y_0), the MATs of the endocardial boundaries derived from the Static, the Uncorrected, and the ResyncCT images were $T_0 = 223$ ms (ground-truth), $T_U = 185$ ms, and $T_R = 207$ ms, respectively.

Figure 3.10 extends the data shown in Fig. 3.6 to include all the defined MAPs and

all five gantry angle simulations for both the septal and the lateral wall m-mode lines. Figures 3.10A and 3.10C show the data for the lateral wall while Figs. 3.10B and 3.10D show the data for the septal wall. Figures 3.10A-B show the endocardial boundary positions across the cardiac cycle sampled by the m-mode lines for the five starting gantry angles. The boundaries derived from the Static, the Uncorrected, and the ResyncCT images are shown by the red, black, and blue lines, respectively. Figures 3.10C-D show the distributions of the MATs estimated from the Uncorrected (gray boxes) and the ResyncCT (blue boxes) images as a function of the defined MAPs. Each distribution contains 5 points, corresponding to the 5 simulated starting gantry angles. The red lines correspond to the ground-truth MAT at each defined MAP, estimated from the Static images.

The range of MATs observed across all 5 starting gantry angles and estimated over all MAPs was significantly higher for the Uncorrected images than the ResyncCT images (lateral wall: 58 ± 15 ms vs 12 ± 4 ms, $p < 0.005$; septal wall: 61 ± 13 ms vs 13 ± 9 ms, $p < 0.005$). From Fig. 3.10, it is clear that the MATs estimated from the ResyncCT images have a much lower error and much higher reproducibility with respect to different starting gantry angles than those estimated from the Uncorrected images. It is also clear that the precision of the estimate is dependent on where the MAT is estimated with respect to the trajectory of the endocardial boundary motion during systole.

3.3.3 Time to Maximal Outward Displacement

Figures 3.11A-B show the second-degree polynomial fits (magenta) to the first 5 time points (0, 70, 140, 210, and 280 ms) of the endocardial boundary positions. These second-degree fits were used to estimate the TMOD of the endocardial wall location sampled by the lateral wall

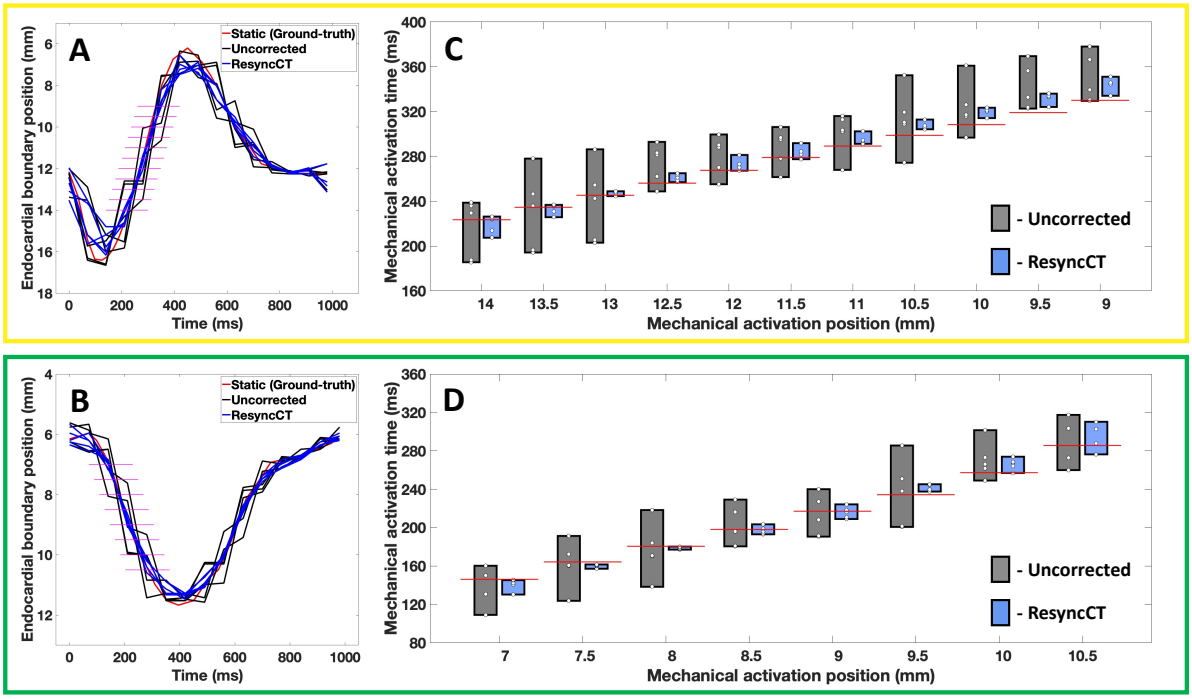

Figure 3.10: Dynamics of endocardial boundary motion during systole. (A-B) Endocardial boundary positions as a function of time across the cardiac cycle sampled by the (A) the lateral wall m-mode and (B) the septal wall m-mode. The endocardial boundary positions derived from the Static, the Uncorrected, and the ResyncCT images are shown by the red, black, and blue lines respectively. (C-D) Distributions of mechanical activation times (MATs) as a function of defined mechanical activation positions (MAPs) estimated from the Uncorrected (gray boxes) and the ResyncCT (blue boxes) images. The red lines represent the ground-truth MAT estimated from the Static images. Each distribution contains 5 points corresponding to the 5 simulated starting gantry angles. The locations of the defined MAPs in relation to the trajectory of endocardial boundary motion are shown by the magenta lines in 3.10A-B.

m-mode line. Each column corresponds to a simulated starting gantry angle; 0°through 180°from left to right. Figure 3.11A shows the estimation of TMOD for the endocardial boundaries derived from the Uncorrected images and Fig. 3.11B shows the estimation of TMOD for the boundaries derived from the ResyncCT images. Figure 3.11C shows the standard deviation ($\pm 1\sigma$) around the TMOD estimates for each of the 5 simulated starting gantry angles. The dashed red line corresponds to the ground-truth TMOD value of 123 ms. The range ($=2\sigma$) of the TMOD estimates observed over all 5 simulated starting gantry angles was 41 $\pm$ 8 ms for the Uncorrected

images and 18 ± 7 ms for the ResyncCT images ($p < 0.005$). It should be noted that endocardial stretch is small, or does not occur at all in some failing left ventricles; therefore, it is likely not a good parameter for measuring timing of mechanics with 4DCT.

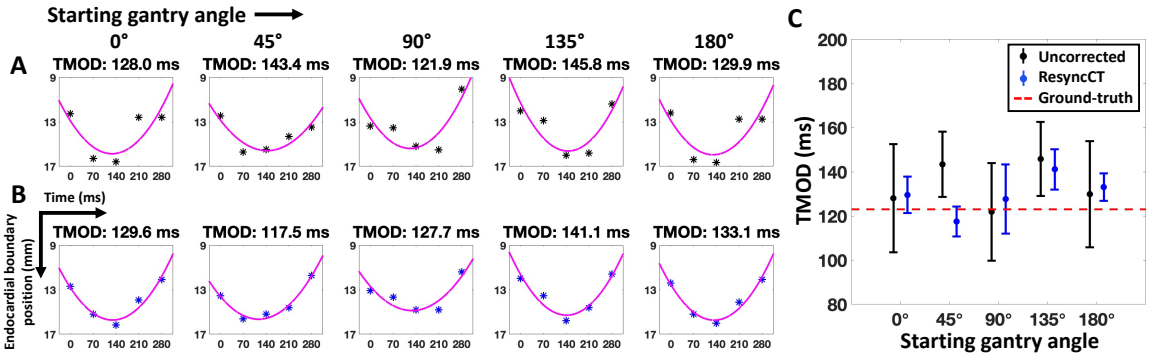

Figure 3.11: Time to maximal outward displacement (TMOD) of the endocardial wall location sampled by the lateral wall m-mode line. (A-B) Second degree polynomial fits (magenta) to the first 5 time points of the endocardial boundary positions derived from (A) the Uncorrected (black asterisks) and (B) the ResyncCT (blue asterisks) images. Each column corresponds to a simulated starting gantry angle. (C) ± 1 standard deviation around the TMOD estimates derived from the Uncorrected (black) and the ResyncCT (blue) images for each of the 5 simulated starting gantry angles. The dashed red line corresponds to the ground-truth TMOD value of 123 ms.

3.4 Discussion

The objective of this study was to develop an anthropomorphically accurate LV phantom with programmable dyssynchrony to test the efficacy of 4DCT in estimating the timing of cardiac mechanical events. The main findings of this study reveal that motion correction of 4DCT images significantly improves the accuracy and precision of estimating mechanical activation times of LV wall motion at local regions of the heart wall.

To the best of our knowledge, the phantom described in this paper is the first anthropomorphically accurate LV phantom to be used in the estimation of mechanical activation times of LV wall motion using 4DCT. The 4D XCAT phantom has previously been used as a simulation

tool in the assessment of mechanical LV dyssynchrony using gated SPECT MPI [25]. Although not performed in this study, local regions of dysfunction simulating ischemic/scar tissue could be incorporated into the motion model of the dyssynchronous phantom; this could be used to test the ability of 4DCT imaging systems to identify viable myocardium for optimal lead placement.

The temporal resolution of 4DCT is more complex than just reconstructing more time frames across the cardiac cycle with shorter time intervals in between the frames. The accuracy and precision of measuring mechanical activation times actually depends on the position of the gantry with respect to the direction of endocardial wall motion. For 4DCT cardiac imaging, each time frame is reconstructed from data acquired over 180°+ fan angle ("halfscan" reconstruction) [10] and the reconstructed image is not a simple temporal average of the true image of the moving heart within this acquisition window. Instead, each spatial frequency component of the image has its own temporal skew which is determined by the time at which the corresponding rays (orthogonal to its orientation) are measured during the acquisition. Since each spatial frequency has excellent "local" temporal resolution due to the sub-millisecond acquisition of each ray, motion compensation can be achieved if the temporal skew associated with each spatial frequency is accurately modeled.

The developed dyssynchronous LV phantom was used to assess the accuracy and precision of estimating mechanical activation times of LV wall motion at local regions of the endocardium using 4DCT, both with and without motion correction. Since there is no universally accepted definition nor method of computation of 'mechanical activation time' [12, 14, 26], a series of 'activation times' spanning the full range of endocardial systolic wall motion (MATs) was investigated, including the time to peak outward motion of the delayed contracting lateral wall (TMOD). Motion correcting the 4DCT images with the ResyncCT software yielded mechanical

activation times of endocardial wall motion that were significantly more accurate and precise than those obtained from images without motion correction. Multiple studies have reported that the mechanical activation delays between segments of the LV wall are of the order of 120 ± 100 ms in patients with a left bundle branch block [27, 28], whereas the delays in healthy controls are of the order of 20 ± 10 ms [29]. The MAT estimates obtained from the ResyncCT images have high precision which can enable the detection of LV dyssynchrony using 4DCT with high confidence.

4DCT wide detector imaging systems have excellent spatial resolution, are easy to operate, and permit rapid imaging of the heart (160 ms per image). 4DCT is also available to those patients with implanted metallic medical devices. Additionally, with recent advances in CT technology, the average radiation dose from a cardiac function scan is < 3 mSv, which is less than the average dose received from natural sources in a year [30]. The ability to image within a single heartbeat eliminates step-artifacts, which is a major limitation when imaging patients with arrhythmia. These advantages coupled with the encouraging results from this study, highlight the potential utility of modern 4DCT imaging systems in guiding CRT.

3.4.1 Limitations

The methods described in this study could be expanded to measure sensitivity to motion artifacts on the entire 3D endocardium. In the current form, 1 cm thick axial slabs of the phantom's endocardial surface were extracted; since these slabs were fixed in space, there was movement of phantom tissue into and out of the imaging plane as the phantom was programmed to contract and relax. Motion correction was then performed on the images of these axial slabs. As the motion of the human heart is highly 3D in nature, future studies investigating the accuracy

and precision of measuring mechanical activation times of the entire 3D endocardium could be performed.

Low x-ray dosage implies low image quality. The images of the 3D printed phantom cylinders were acquired under 350 mA and 100 kVp tube current settings, which constitutes a "medium" dose scan. While this study succeeded in demonstrating the high accuracy and precision of estimating mechanical activation times from 4DCT images with ResyncCT motion correction, the effect of dose on the accuracy and precision of those estimates should be investigated.

The dyssynchronous phantom developed in this study utilized a set of displacements that yielded endocardial strains typical of those observed in a patient with an LBBB or RV apical pacing [18, 19]. While the designed strain functions were sufficient to demonstrate the potential value of 4DCT + ResyncCT in the estimation of mechanical activation times of LV wall motion, future studies could explore the effect of varying regional and global LV function. Additionally, the strain functions were smooth in nature with a linear interpolation of strains between the delayed lateral wall and the earlier activating septum. While the highly detailed motions of hearts may contain fast subtle motions, the programmed motion of the phantom was sufficient to accurately model the "stationary-wall" and the "double-wall" artifacts which are the primary sources of error when estimating mechanical activation times of the myocardial walls with 4DCT.

The dynamics of endocardial boundary motion during systole were investigated using two m-mode lines, one on the lateral wall and the other on the septum. Both m-mode lines sampled endocardial wall motion in phase with different gantry angles during data acquisition. While sampling endocardial wall motion at only two locations is a limitation, we believe this limited spatial sampling is compensated by simulating 5 different starting gantry angles. The starting

gantry angles were simulated in increments of 45°; this effectively leads to sampling locations on the endocardium by m-mode lines perpendicular to the surface rotating in 45°increments.

As shown from phantom experiments in this study, 4DCT + ResyncCT yield highly accurate estimates of mechanical activation times of endocardial wall motion. The promising initial results reported in this work motivate future studies to perform a head-to-head validation in patients against CMR tagging, the gold-standard modality for estimating regional cardiac function.

3.5 Conclusions

We developed an anthropomorphically accurate dyssynchronous LV phantom and used this phantom to evaluate the accuracy and precision of estimating mechanical activation times of LV wall motion with 4DCT. After motion correction with the ResyncCT algorithm, 4DCT yields estimates of mechanical activation times of LV wall motion with significantly improved accuracy and precision. The promising results reported in this study highlight the potential utility of 4DCT in measuring the timing of mechanical events of interest for CRT guidance.

Acknowledgements

This research was supported by NHLBI of the National Institutes of Health under award number R01 HL144678 (McVeigh). The content is solely the responsibility of the authors and does not necessarily represent the official views of the National Institutes of Health. This work was done during the term of an Award from the American Heart Association (AHA 20PRE35210261).

Chapter 3 is a reprint of the material: **Ashish Manohar**, Jed D. Pack, Andrew J.

Schluchter, and Elliot R. McVeigh. "Four-dimensional computed tomography of the left ventricle, Part II: Estimation of mechanical activation times" *Medical Physics* **49**, 2022. The dissertation author is the primary author.

3.6 References

1. Vernooy, K., van Deursen, C. J. M., Strik, M. & Prinzen, F. W. Strategies to improve cardiac resynchronization therapy. *Nature Reviews Cardiology* **11,** 481–493. ISSN: 1759-5002. `http://www.nature.com/articles/nrcardio.2014.67` (Aug. 2014).

2. Mirea, O., Pagourelias, E. D., Duchenne, J., Bogaert, J., Thomas, J. D., Badano, L. P., Voigt, J.-U., Badano, L. P., Thomas, J. D., Hamilton, J., Pedri, S., Lysyansky, P., Hansen, G., Ito, Y., Chono, T., Vogel, J., Prater, D., Park, S., Lee, J. Y., Houle, H., Georgescu, B., Baumann, R., Mumm, B., Abe, Y. & Gorissen, W. Variability and Reproducibility of Segmental Longitudinal Strain Measurement. *JACC: Cardiovascular Imaging* **11,** 15–24. ISSN: 1936878X. `https://linkinghub.elsevier.com/retrieve/pii/S1936878X17303601` (Jan. 2018).

3. Mirea, O., Pagourelias, E. D., Duchenne, J., Bogaert, J., Thomas, J. D., Badano, L. P., Voigt, J.-U., Badano, L. P., Thomas, J. D., Hamilton, J., Pedri, S., Lysyansky, P., Hansen, G., Ito, Y., Chono, T., Vogel, J., Prater, D., Park, S., Lee, J. Y., Houle, H., Georgescu, B., Baumann, R., Mumm, B., Abe, Y. & Gorissen, W. Intervendor Differences in the Accuracy of Detecting Regional Functional Abnormalities. *JACC: Cardiovascular Imaging* **11,** 25–34. ISSN: 1936878X. `https://linkinghub.elsevier.com/retrieve/pii/S1936878X17303637` (Jan. 2018).

4. Daubert, J.-C., Saxon, L., Adamson, P. B., Auricchio, A., Berger, R. D., Beshai, J. F., Breithard, O., Brignole, M., Cleland, J., DeLurgio, D. B., Dickstein, K., Exner, D. V., Gold, M., Grimm, R. A., Hayes, D. L., Israel, C., Leclercq, C., Linde, C., Lindenfeld, J., Merkely, B., Mont, L., Murgatroyd, F., Prinzen, F., Saba, S. F., Shinbane, J. S., Singh, J., Tang, A. S., Vardas, P. E., Wilkoff, B. L., Zamorano, J. L., Anand, I., Blomstrom-Lundqvist, C., Boehmer, J. P., Calkins, H., Cazeau, S., Delgado, V., Estes, N. A. M., Haines, D., Kusumoto, F., Leyva, P., Ruschitzka, F., Stevenson, L. W. & Torp-Pedersen, C. T. 2012 EHRA/HRS expert consensus statement on cardiac resynchronization therapy in heart failure: implant and follow-up recommendations and management: A registered branch of the European Society of Cardiology (ESC), and the Heart Rhythm Society; and in col. *Europace* **14,** 1236–1286. ISSN: 1099-5129. `https://academic.oup.com/europace/article-lookup/doi/10.1093/europace/eus222` (Sept. 2012).

5. Truong, Q. A., Singh, J. P., Cannon, C. P., Sarwar, A., Nasir, K., Auricchio, A., Faletra, F. F., Sorgente, A., Conca, C., Moccetti, T., Handschumacher, M., Brady, T. J. & Hoffmann, U. Quantitative Analysis of Intraventricular Dyssynchrony Using Wall Thickness by Multidetector Computed Tomography. *JACC: Cardiovascular Imaging* **1,** 772–

781. ISSN: 1936878X. http://dx.doi.org/10.1016/j.jcmg.2008.07.014%20https://linkinghub.elsevier.com/retrieve/pii/S1936878X08003604 (Nov. 2008).

6. Truong, Q. A., Szymonifka, J., Picard, M. H., Thai, W.-e., Wai, B., Cheung, J. W., Heist, E. K., Hoffmann, U. & Singh, J. P. Utility of dual-source computed tomography in cardiac resynchronization therapy—DIRECT study. *Heart Rhythm* **15,** 1206–1213. ISSN: 15475271. https://doi.org/10.1016/j.hrthm.2018.03.020%20https://linkinghub.elsevier.com/retrieve/pii/S1547527118302340 (Aug. 2018).

7. Behar, J. M., Rajani, R., Pourmorteza, A., Preston, R., Razeghi, O., Niederer, S., Adhya, S., Claridge, S., Jackson, T., Sieniewicz, B., Gould, J., Carr-White, G., Razavi, R., McVeigh, E. & Rinaldi, C. A. Comprehensive use of cardiac computed tomography to guide left ventricular lead placement in cardiac resynchronization therapy. *Heart Rhythm* **14,** 1364–1372. ISSN: 15475271. http://dx.doi.org/10.1016/j.hrthm.2017.04.041%20https://linkinghub.elsevier.com/retrieve/pii/S154752711730574X (Sept. 2017).

8. Pourmorteza, A., Schuleri, K. H., Herzka, D. A., Lardo, A. C. & McVeigh, E. R. A New Method for Cardiac Computed Tomography Regional Function Assessment. *Circulation: Cardiovascular Imaging* **5,** 243–250. ISSN: 1941-9651. https://www.ahajournals.org/doi/10.1161/CIRCIMAGING.111.970061 (Mar. 2012).

9. Kidoh, M., Shen, Z., Suzuki, Y., Ciuffo, L., Ashikaga, H., Fung, G. S. K., Otake, Y., Zimmerman, S. L., Lima, J. A. C., Higuchi, T., Lee, O., Sato, Y., Becker, L. C., Fishman, E. K. & Taguchi, K. *False dyssynchrony: problem with image-based cardiac functional analysis using x-ray computed tomography* in *Medical Imaging 2017: Physics of Medical Imaging* (eds Flohr, T. G., Lo, J. Y. & Gilat Schmidt, T.) (Mar. 2017), 101321U. ISBN: 9781510607095. http://proceedings.spiedigitallibrary.org/proceeding.aspx?doi=10.1117/12.2250257.

10. Contijoch, F., Stayman, J. W. & McVeigh, E. R. The impact of small motion on the visualization of coronary vessels and lesions in cardiac CT: A simulation study. *Medical Physics* **44,** 3512–3524. ISSN: 00942405. http://doi.wiley.com/10.1002/mp.12295 (July 2017).

11. Li, Y., Cao, X., Xing, Z., Sun, X., Hsieh, J. & Chen, G.-H. *Image quality improvement in MDCT cardiac imaging via SMART-RECON method* in *Medical Imaging 2017: Physics of Medical Imaging* (eds Flohr, T. G., Lo, J. Y. & Gilat Schmidt, T.) **10132** (Mar. 2017), 101322Z. ISBN: 9781510607095. http://proceedings.spiedigitallibrary.org/proceeding.aspx?doi=10.1117/12.2254644.

12. Auger, D. A., Bilchick, K. C., Gonzalez, J. A., Cui, S. X., Holmes, J. W., Kramer, C. M., Salerno, M. & Epstein, F. H. Imaging left-ventricular mechanical activation in heart failure patients using cine DENSE MRI: Validation and implications for cardiac resynchronization therapy. *Journal of Magnetic Resonance Imaging* **46,** 887–896. ISSN: 10531807. http://doi.wiley.com/10.1002/jmri.25613%20https://onlinelibrary.wiley.com/doi/10.1002/jmri.25613 (Sept. 2017).

13. Gao, X., Abdi, M., Auger, D. A., Sun, C., Hanson, C. A., Robinson, A. A., Schumann, C., Oomen, P. J., Ratcliffe, S., Malhotra, R., Darby, A., Monfredi, O. J., Mangrum, J. M., Mason, P., Mazimba, S., Holmes, J. W., Kramer, C. M., Epstein, F. H., Salerno, M. & Bilchick, K. C. Cardiac Magnetic Resonance Assessment of Response to Cardiac Resynchronization Therapy and Programming Strategies. *JACC: Cardiovascular Imaging.* ISSN: 1936878X. https://linkinghub.elsevier.com/retrieve/pii/S1936878X21005052 (Aug. 2021).

14. Wyman, B. T., Hunter, W. C., Prinzen, F. W. & McVeigh, E. R. Mapping propagation of mechanical activation in the paced heart with MRI tagging. *American Journal of Physiology-Heart and Circulatory Physiology* **276,** H881–H891. ISSN: 0363-6135. https://www.physiology.org/doi/10.1152/ajpheart.1999.276.3.H881 (Mar. 1999).

15. Faris, O. P., Evans, F. J., Ennis, D. B., Helm, P. A., Taylor, J. L., Chesnick, A. S., Guttman, M. A., Ozturk, C. & McVeigh, E. R. Novel Technique for Cardiac Electromechanical Mapping with Magnetic Resonance Imaging Tagging and an Epicardial Electrode Sock. *Annals of Biomedical Engineering* **31,** 430–440. ISSN: 0090-6964. http://link.springer.com/10.1114/1.1560618 (Apr. 2003).

16. Manohar, A., Colvert, G. M., Schluchter, A., Contijoch, F. & McVeigh, E. R. Anthropomorphic left ventricular mesh phantom: a framework to investigate the accuracy of SQUEEZ using Coherent Point Drift for the detection of regional wall motion abnormalities. *Journal of Medical Imaging* **6,** 1. ISSN: 2329-4302. https://www.spiedigitallibrary.org/journals/journal-of-medical-imaging/volume-6/issue-04/045001/Anthropomorphic-left-ventricular-mesh-phantom--a-framework-to-investigate/10.1117/1.JMI.6.4.045001.full (Dec. 2019).

17. Yushkevich, P. A., Piven, J., Hazlett, H. C., Smith, R. G., Ho, S., Gee, J. C. & Gerig, G. User-guided 3D active contour segmentation of anatomical structures: Significantly improved efficiency and reliability. *NeuroImage* **31,** 1116–1128. ISSN: 10538119. https://linkinghub.elsevier.com/retrieve/pii/S1053811906000632 (July 2006).

18. Helm, R. H., Leclercq, C., Faris, O. P., Ozturk, C., McVeigh, E., Lardo, A. C. & Kass, D. A. Cardiac Dyssynchrony Analysis Using Circumferential Versus Longitudinal Strain. *Circulation* **111,** 2760–2767. ISSN: 0009-7322. https://www.ahajournals.org/doi/10.1161/CIRCULATIONAHA.104.508457 (May 2005).

19. Delgado, V., Ypenburg, C., van Bommel, R. J., Tops, L. F., Mollema, S. A., Marsan, N. A., Bleeker, G. B., Schalij, M. J. & Bax, J. J. Assessment of Left Ventricular Dyssynchrony by Speckle Tracking Strain Imaging. *Journal of the American College of Cardiology* **51,** 1944–1952. ISSN: 07351097. https://linkinghub.elsevier.com/retrieve/pii/S0735109708008632 (May 2008).

20. Lumens, J., Leenders, G. E., Cramer, M. J., De Boeck, B. W. L., Doevendans, P. A., Prinzen, F. W. & Delhaas, T. Mechanistic Evaluation of Echocardiographic Dyssynchrony Indices. *Circulation: Cardiovascular Imaging* **5,** 491–499. ISSN: 1941-9651. https://www.ahajournals.org/doi/10.1161/CIRCIMAGING.112.973446 (July 2012).

21. Kim, S., Chang, Y. & Ra, J. B. Cardiac motion correction based on partial angle reconstructed images in x-ray CT. *Medical Physics* **42,** 2560–2571. ISSN: 00942405. http://doi.wiley.com/10.1118/1.4918580 (Apr. 2015).

22. Strotmann, J. M., Kvitting, J.-P. E., Wilkenshoff, U. M., Wranne, B., Hatle, L. & Sutherland, G. R. Anatomic M-Mode Echocardiography: A New Approach to Assess Regional Myocardial Function—A Comparative In Vivo and In Vitro Study of Both Fundamental and Second Harmonic Imaging Modes. *Journal of the American Society of Echocardiography* **12,** 300–307. ISSN: 08947317. https://linkinghub.elsevier.com/retrieve/pii/S0894731799700507 (May 1999).

23. Feigenbaum, H. Role of M-mode Technique in Today's Echocardiography. *Journal of the American Society of Echocardiography* **23,** 240–257. ISSN: 08947317. http://dx.doi.org/10.1016/j.echo.2010.01.015%20https://linkinghub.elsevier.com/retrieve/pii/S0894731710000581 (Mar. 2010).

24. Otsu, N. A Threshold Selection Method from Gray-Level Histograms. *IEEE Transactions on Systems, Man, and Cybernetics* **9,** 62–66. ISSN: 0018-9472. http://ieeexplore.ieee.org/document/4310076/ (Jan. 1979).

25. Cheung, A. A., Tianye Niu, Faber, T. L., Segars, W. P., Lei Zhu & Ji Chen. *Simulation of left ventricular dyssynchrony using the XCAT phantom* in *IEEE Nuclear Science Symposuim & Medical Imaging Conference* (IEEE, Oct. 2010), 3187–3189. ISBN: 978-1-4244-9106-3. http://ieeexplore.ieee.org/document/5874391/.

26. Zwanenburg, J. J. M., Götte, M. J. W., Kuijer, J. P. A., Heethaar, R. M., van Rossum, A. C. & Marcus, J. T. Timing of cardiac contraction in humans mapped by high-temporal-resolution MRI tagging: early onset and late peak of shortening in lateral wall. *American Journal of Physiology-Heart and Circulatory Physiology* **286,** H1872–H1880. ISSN: 0363-6135. https://www.physiology.org/doi/10.1152/ajpheart.01047.2003 (May 2004).

27. Van Bommel, R. J., Tanaka, H., Delgado, V., Bertini, M., Borleffs, C. J. W., Ajmone Marsan, N., Holzmeister, J., Ruschitzka, F., Schalij, M. J., Bax, J. J. & Gorcsan, J. Association of intraventricular mechanical dyssynchrony with response to cardiac resynchronization therapy in heart failure patients with a narrow QRS complex. *European Heart Journal* **31,** 3054–3062. ISSN: 0195-668X. https://academic.oup.com/eurheartj/article-lookup/doi/10.1093/eurheartj/ehq334 (Dec. 2010).

28. Andersson, L. G., Wu, K. C., Wieslander, B., Loring, Z., Frank, T. F., Maynard, C., Gerstenblith, G., Tomaselli, G. F., Weiss, R. G., Wagner, G. S., Ugander, M. & Strauss, D. G. Left ventricular mechanical dyssynchrony by cardiac magnetic resonance is greater in patients with strict vs nonstrict electrocardiogram criteria for left bundle-branch block. *American Heart Journal* **165,** 956–963. ISSN: 00028703. https://linkinghub.elsevier.com/retrieve/pii/S0002870313002196 (June 2013).

29. Bader, H., Garrigue, S., Lafitte, S., Reuter, S., Jaïs, P., Haïssaguerre, M., Bonnet, J., Clementy, J. & Roudaut, R. Intra-left ventricular electromechanical asynchrony. *Journal*

of the American College of Cardiology **43,** 248–256. ISSN: 07351097. https://linkinghub.elsevier.com/retrieve/pii/S0735109703014165 (Jan. 2004).

30. Bolus, N. E. NCRP Report 160 and What It Means for Medical Imaging and Nuclear Medicine. *Journal of Nuclear Medicine Technology* **41,** 255–260. ISSN: 0091-4916. http://tech.snmjournals.org/cgi/doi/10.2967/jnmt.113.128728 (Dec. 2013).

Chapter 4

Prediction of CRT response using a lead placement score defined using 4DCT-derived features of LV mechanics

Cardiac resynchronization therapy (CRT) is a proven treatment for patients with heart failure and dyssynchrony; however, approximately 30% of patients do not respond to the treatment. Additionally, the relatively high non-responder rate poses difficulties for the optimal utilization of medical resources; thus, more accurate patient stratification for CRT remains an unmet need. Despite significant efforts focused on using imaging to guide CRT, the results thus far have been ambiguous. Poor reproducibility of echocardiography coupled with the complexity of cardiac magnetic resonance have likely contributed to the poor overall adoption of these meth-

ods for pre-CRT assessment. In this work, we describe a metric called the lead placement score (LPS) that combines multiple 4DCT-derived features of left-ventricular (LV) mechanics into a single number for each possible pacing lead location on the LV; the features included in the LPS map have previously been shown to correlate with CRT response. Using a machine learning classifier, a model was constructed with these features and then used to derive the LPS map for each individual subject. The LPS was found to correlate with the probability of a subject responding to CRT. 4DCT is widely available and provides high-resolution images of the full cardiac cycle. Additionally, recent technological advancements have also dramatically reduced the radiation dose from 4DCT scans. The advantages of 4DCT coupled with the promising results reported in this study, highlight the potential utility of 4DCT in the planning of CRT.

4.1 Background

Multiple trials have proven that cardiac resynchronization therapy (CRT) can provide significant benefit for patients with intraventricular dyssynchrony and heart failure [1]. Current guidelines for CRT patient selection include New York Heart Association (NYHA) functional classes II-IV, echocardiography-derived left ventricular ejection fractions (LVEF) $\leq$ 35%, and QRS durations ¿120 ms [2]. Despite its proven benefit, approximately 30% of patients selected for CRT do not respond to the treatment [3]. This non-responder rate continues to pose considerable challenges for the optimal utilization of medical resources [4]; thus, necessitating accurate patient stratification.

Significant effort has been focused on reducing the non-responder rate through the use of imaging, for the most part with echocardiography [5]. Two-dimensional radial strain from speckle-tracking echocardiography has been previously used to identify optimal left ventricle (LV)

lead placement sites [6]. Additionally, a number of studies have explored the role of tissue doppler imaging in patient selection for CRT [7]. However, poor reproducibility of echocardiography measurements due to inter- and intra-observer variability coupled with inter-vendor differences have led to disappointing results and hindered its routine clinical use [8].

Similarly, cardiac magnetic resonance (CMR) imaging has also been used to guide CRT [9]. Cine MRI [10], tagged MRI [11], and cine DENSE [12] have shown great promise in mapping regional strain and mechanical activation times of the LV myocardium. Also, late gadolinium enhancement imaging is effective at identifying regions of scar tissue that need to be avoided for lead placement [13]. However, 28% of patients in consideration for CRT already have existing right ventricular (RV) pacing systems in place [2], making CMR not widely available to this cohort. Additionally, tagged MRI and cine DENSE images are not simple to acquire and analyze, requiring skilled technicians and image analysis personnel. No imaging modality is currently recommended for CRT planning and management.

Recent studies have explored the use of 4DCT to guide CRT. Truong et al. used dual-source CT to derive LV dyssynchrony indices that predicted 2-year major adverse cardiac events (MACE). They also reported that leads placed on sites with maximal wall thickness correlated with less MACE [14]. Rinaldi and colleagues utilized 4DCT-derived assessment of LV dyssynchrony and myocardial scar to target LV lead placement. They showed that patients with leads implanted in segments targeted from CT had higher clinical response rates [15] and superior acute hemodynamic responses [16] than those with leads implanted in the non-target segments. Fyenbo et al. used CT to identify regions of myocardial scar and to compute scar burden. They found that high scar burden and proximity of scar to the LV pacing site were correlated with echocardiographic non-response [17].

We hoped to improve on the insights from these previous studies by using additional features of LV mechanics that have previously been shown to correlate with CRT response [1] in a larger number of subjects. Thus, the purpose of this study was to use a combination of 4DCT-derived regional and global features of LV mechanics to define patient-specific maps of lead placement scores (LPS) that are correlated with CRT response.

4.2 Methods

4.2.1 Subject Population and CT Imaging

Subjects recruited for the ImagingCRT [18] randomized controlled trial were retrospectively used for this study. The trial enrolled a total of 182 subjects; however, only 147 subjects had contrast enhanced 4DCT scans both before and after CRT implantation. The complete study protocol for the trial is described in detail by Sommer et al. [18, 19]. Briefly, all 147 subjects were ¿ 40 years, belonged to NYHA functional classes II-IV, had echocardiography derived LVEF $\leq$ 35%, and had QRS widths $\geq$ 120 ms with a left bundle branch block (LBBB) or ¿ 180 ms with an RV pacing configuration, respectively. The trial was conducted at the Department of Cardiology, Aarhus University Hospital, Skejby, Denmark and was approved by the Central Denmark regional committee on health research ethics as well as the Danish Data Protection Agency. All trial participants gave informed written consent, and the trial was registered on Clinicaltrials.gov (NCT01323686).

The prescribed cardiac 4DCT imaging protocol has previously been described in detail [18]. Each subject had two contrast-enhanced full cardiac cycle and full LV volume retrospective ECG-gated 4DCT scans: the first scan was on the day prior to CRT implantation and the second

scan was 6-months after implantation; we refer to these scans hereafter as the *baseline* and the *follow-up* scans, respectively. All scans were acquired using a dual-source CT scanner (Somatom Definition Flash, Siemens Healthcare, Erlangen, Germany) with a multi-slice z-axis detector of 38.4 mm, a gantry rotation time of 280 ms, pitch factors in the range of [0.17, 0.3], x-ray tube voltages of 80-120 kVp, and adaptive tube currents with a reference of 370 mAs. In these retrospective scans, an ECG controlled tube current modulation was applied with reduction of the current to 20% and reference mA applied only between 60-70% of the R-R interval. Images were reconstructed every 5% of the R-R interval, from 0% to 95%, using an iterative reconstruction algorithm (SAFIRE I26f-4, Siemens Healthcare, Erlangen, Germany). The reconstructed images had in-plane pixel spacings in the range of [0.6, 1] mm and slice thicknesses of 0.7 mm.

Subjects were excluded from this study if either their baseline or follow-up scans had one or more of the following imaging artifacts, preventing precise measurements of LV mechanics:

1. Severe helical step artifact
2. Insufficient LV chamber-myocardium contrast for blood volume segmentation
3. Severe metal artifacts from the pacemaker/defibrillator leads preventing segmentation of the LV blood volume

4.2.2 Image Segmentation and Mesh Extraction

The LV blood pool was segmented from the reconstructed CT images in a manner similar to that described by Colvert et al. [20] and Manohar et al. [21]. Briefly, the blood pool was segmented in ITK-SNAP v3.8.0 [22] software using the active contour region growing module. Two planes delineating the mitral valve and the left ventricular outflow tract (LVOT) were defined as previously described [20]. The process was repeated for all 20 time frames in each

of the baseline and the follow-up 4DCT datasets of each subject. Additionally, the positions of the right and the left lead tips were marked in the end diastolic image of the follow-up scans; these positions were used to project the corresponding right and left pacing sites onto the LV endocardial model, respectively. Figure 4.1 illustrates the segmentation process.

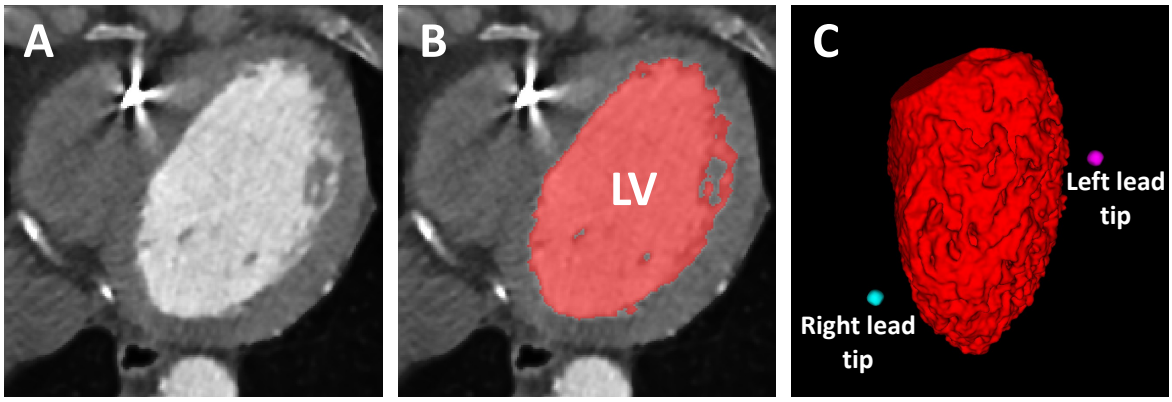

Figure 4.1: LV blood-volume segmentation. (A) Axial contrast-enhanced cardiac CT image. (B) LV blood-volume segmentation overlaid in red. (C) 3D rendering of the LV blood-volume segmentation with the locations of the right (cyan) and the left (magenta) lead tips. The anterior wall is in view with the septum on the left and the lateral wall on the right. LV: left ventricle.

Meshes defining the endocardium were extracted using the *isosurface* MATLAB routine (MathWorks Inc., Natick, MA; v9.8 – R2020a). Vertices and faces belonging to the defined mitral valve and LVOT planes were removed, leaving a 2D surface delineating only the LV endocardium. The meshes were extracted at an isotropic resolution of 2 mm in x, y, and z directions for calculating local LV function, which was consistent with previously published analyses [20, 21, 23, 24].

4.2.3 Global and Regional Features of LV Mechanics

Eight global and regional features of LV mechanics were derived from the baseline 4DCT scans for each subject. The global LV features used were:

1. End diastolic volume (EDV)

2. End systolic volume (ESV)

3. Circumferential uniformity ratio estimate using singular value decomposition (CURE-SVD)

4. LV sphericity index (LVSI)

and the regional LV features used were:

1. Peak regional shortening (PRS_{CT})

2. Time to peak regional shortening ($TPRS_{CT}$)

3. Maximum pre-stretch of regional shortening ($MSRS_{CT}$)

4. Time to onset of shortening (TOS)

The choice of these 8 features was driven by previous CRT studies using CMR and CT imaging [1, 10]. Detailed information on the computation of the above 8 features can be found in the Supplemental Material. Figure 4.2 describes the estimation of the 4 regional LV features.

LV volumes and ejection fraction

LV volume was computed as a function of time across the cardiac cycle for all 20 times frames in each 4D dataset by summing the segmented LV blood pool voxels in each time frame. LVEF was then calculated as:

$$LVEF = \frac{EDV - ESV}{EDV}, \tag{4.1}$$

where EDV is the LV volume in mL at end diastole and ESV is the LV volume in mL at end systole.

Circumferential uniformity ratio estimate

An additional feature used in this work is the circumferential uniformity ratio estimate (CURE) [25, 26]. CURE is a metric that describes the synchrony or dyssynchrony of contraction in the circumferential direction of a particular short axis slice of the LV. A spatiotemporal matrix containing RS_{CT}values was constructed, with the columns representing time frames of the cardiac cycle and the rows representing the spatial sampling of RS_{CT}in the circumferential direction of a slice of the LV endocardium. To obtain an estimate of CURE that was less sensitive to noise, a singular value decomposition (SVD) was performed on this matrix to smooth out noise and to identify the primary spatiotemporal pattern of RS_{CT}in the particular LV slice. Only the rank-1 SVD approximation was retained. A modified CURE value based on this rank-1 SVD approximation, called CURE-SVD [27], was calculated as the ratio of the amplitude of the DC component to the sum of the amplitudes of the DC and the first order sinusoidal frequency components, given by the equation:

$$CURE - SVD = \frac{f_0}{f_0 + f_1}, \tag{4.2}$$

where f_0 is the amplitude of the DC component and f_1 is the amplitude of the first order sinusoidal component. These frequency components were derived from a Fourier transform analysis of the circumferential distribution of RS_{CT}at a particular time frame of the cardiac cycle (Fourier transform of the signal from a particular column of the rank-1 SVD matrix). The Fourier transform analysis was performed using the built-in fft function in MATLAB (MathWorks Inc., Natick, MA; v9.8 – R2020a). The above process of constructing a spatiotemporal matrix of RS_{CT}, deriving its rank-1 SVD approximation, and calculating CURE-SVD was repeated for all defined

short axis slices of the LV endocardium. The final CURE-SVD value for a subject was computed as the average of all CURE-SVD values across all defined LV short axis slices.

Left ventricular sphericity index

Left ventricular sphericity index (LVSI) is a measure that captures the degree of sphericity of the left ventricle and was not used in previous 4DCT studies to guide CRT. It is defined as the ratio of EDV to the volume of a sphere whose diameter is equal to the major axis (long axis) of the LV at end diastole [28], given by the formula:

$$LVSI = \frac{EDV}{\frac{\pi L^3}{6}}, \tag{4.3}$$

where L is the length of the long axis of the LV at end diastole.

Regional endocardial shortening

Regional endocardial shortening ($\mathrm{RS_{CT}}$) from 4DCT images [20, 23, 24] was measured according to the following formula:

$$RS_{\mathrm{CT}}(\nu, t) = \sqrt{\frac{A(\nu, t)}{A(\nu, t=0)}} - 1, \tag{4.4}$$

where $A(\nu, t)$ is the area of an endocardial patch ν at time t of the cardiac cycle and $A(\nu, t = 0)$ is the area of the same endocardial patch ν at end diastole ($t = 0$). The location of each patch ν was tracked over the heart cycle using a point set registration algorithm [29]; the average patch size at end diastole was 2.6 ± 0.5 mm^2. For each time frame of the cardiac cycle, the $\mathrm{RS_{CT}}$values were mapped onto the endocardial surface, yielding a high-resolution estimate of regional endocardial shortening.

For each subject, three features derived from the spatiotemporal distribution of RS_{CT}were defined; Fig. 4.2 describes the three features for an example RS_{CT}vs time curve. The features were:

1. Peak regional shortening (PRS_{CT}): maximum shortening achieved in a spatial segment of the LV. This feature correlates strongly with the existence of myocardial infarction.

2. Time to peak regional shortening ($TPRS_{CT}$): normalized time of the cardiac cycle at which peak shortening occurs in a spatial segment of the LV.

3. Maximum pre-stretch of regional shortening ($MSRS_{CT}$): maximum endocardial pre-stretch (RS_{CT}¿ 0) in a spatial segment of the LV. If pre-stretch does not occur, then $MSRS_{CT}$is 0. This feature correlates strongly with late mechanical activation, and poor myocardial function in that segment.

Time to onset of shortening

The "time to onset of shortening" (TOS) is the time at which the endocardium begins to contract during systole. It has been shown to be an excellent descriptor of dyssynchrony [11, 30, 31] and a strongly predictive feature for CRT response [12]; this feature was not included in previous studies using 4DCT to guide CRT. There is no universally accepted definition nor method of computation of TOS; for our study, the TOS of a spatial segment of the LV was defined as the time at which the RS_{CT}vs time curve for that segment reached 10% of its dynamic range during systole. The dynamic range of shortening during systole was defined as the range from maximum pre-stretch ($MSRS_{CT}$) to peak shortening (PRS_{CT}); if no pre-stretch occurred, it was defined as the range of shortening from end diastole (RS_{CT}= 0) to peak shortening (RS_{CT}= PRS_{CT}). For LV spatial segments with very low function, the TOS was not estimated due to

insufficient dynamic range. Figure 4.2 illustrates the values of PRS_{CT}, $TPRS_{CT}$, $MSRS_{CT}$, and TOS for an exemplar RS_{CT}vs time curve from our 4DCT studies. Curves like this were measured over 90 contiguous local regions of the LV (see 4.2.4.

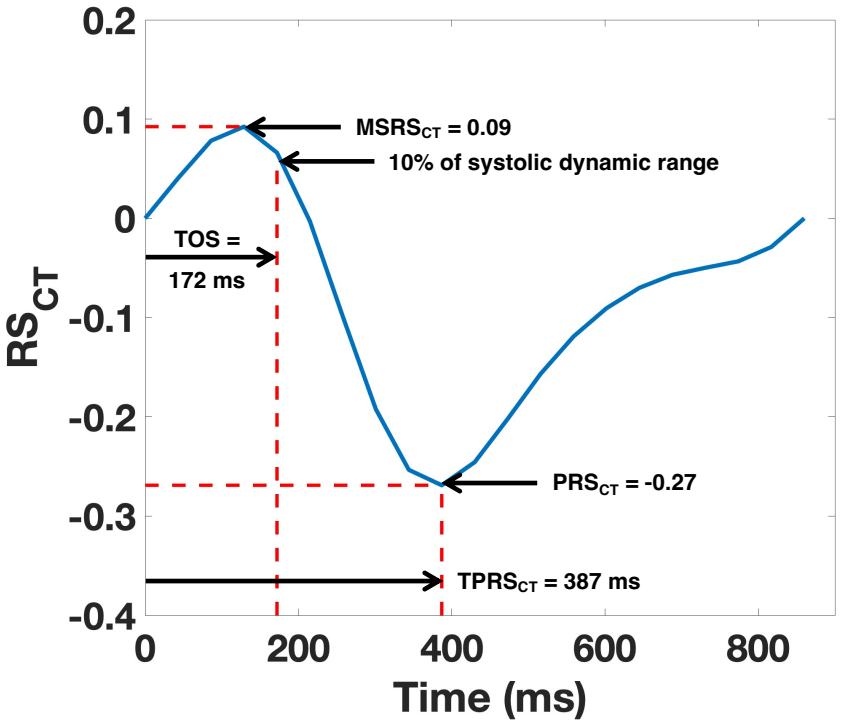

Figure 4.2: Measurements of maximum pre-stretch of regional shortening ($MSRS_{CT}$), time to onset of shortening (TOS), peak regional shortening (PRS_{CT}), and time to peak regional shortening ($TPRS_{CT}$) for an exemplar RS_{CT}vs time curve for a single location on the LV. RS_{CT}: regional endocardial shortening.

4.2.4 Spatial Sampling of the LV Endocardium

The LV endocardium for each subject was divided into 90 spatial segments: 18 circumferential segments (one every 20°) for each slice, and 5 slices defined from apex to base along the long axis of the LV [20]. This 90 segment model yields a higher spatial sampling than the traditional AHA 17 segment model, permitting wall function analysis that captures the high resolution features of mechanical function that are obvious in the 4DCT data. Each region rep-

resents approximately 2 cm^2 of endocardial surface for a normal ventricle. The location of the right and the left lead tips were mapped onto the LV endocardial segments closest to the lead locations.

4.2.5 Definition of CRT Response

Subjects were considered responders if their CT-derived ESV decreased by $\geq$ 15% 6-months post CRT implantation [8]. The ESV of the subjects were computed from the 4DCT exams as described in the Supplemental Material and the change in ESV 6-months post implantation was calculated between the baseline and the follow-up 4DCT scans.

4.2.6 Lead Placement Score

The LPS is a scalar parameter that is obtained by combining several features derived from the baseline 4DCT scan of a subject under consideration for CRT. Our goal was to derive an LPS that is correlated with CRT response. An individual LPS can be calculated for each of the 90 segments of the LV endocardium, yielding a high-resolution patient-specific LPS map that highlights possible target pacing lead sites for achieving a higher probability of CRT response. Since all subjects in this study had follow-up 4DCT scans, the locations of the right and the left lead tips were precisely known; thus, to match the response observed in these subjects, the LPS value in our analysis was obtained from the right and left lead tip locations projected onto the baseline 4DCT scans.

The LPS values were computed using a model obtained by training a support vector machine (SVM) [32]. The following features derived from the baseline scans of the subjects were used in model training: the global LV features of 1) EDV, 2) ESV, 3) CURE-SVD, and

4) LVSI, and the regional LV features of 5) PRS_{CT}, 6) $TPRS_{CT}$, 7) $MSRS_{CT}$, and 8) TOS. For each of the regional LV features, the values at the two spatial segments in the baseline scans that corresponded to the right and the left lead tip locations in the follow-up scans were used to calculate a single LPS value for each subject. For example, TOS-right and TOS-left represented the TOS of the LV segments that spatially corresponded to the segments of the right and the left lead tips in the follow-up scans. Thus, a total of 12 features were used to train the SVM model (4 global + 4x2 regional).

The built-in *fitcsvm* function in MATLAB (Statistics and Machine Learning Toolbox, MathWorks Inc., Natick, MA; v9.8 – R2020a) was used to train the SVM model ('kernel': linear; 'Standardize': true; 'Prior': uniform; all other parameters were set to default). The prior probability input parameter was set to 'uniform' to handle the class imbalance between responders (n=52) and non-responders (n=30) in our dataset; thus, proportionately weighting the cost of misclassification [33]. A bagging [34] approach with 1000 iterations was implemented for training; for each iteration, an SVM model was trained on a bootstrapped dataset that was sampled with replacement. Each bootstrapped dataset had the same number of subjects as the original dataset and the trained SVM model obtained was a vector of 12 feature coefficients. Nine TOS-right values were indeterminable and were imputed via the method of mean imputation [35] for training. The final model was derived by averaging the feature coefficients of the individually trained models on the 1000 bootstrapped datasets (the mean values of the feature coefficients converged around the 350^{th} iteration).

The LPS was calculated for all subjects in the study according to the formula:

$$LPS_i = \boldsymbol{\beta} \cdot \boldsymbol{x_i} + b, \tag{4.5}$$

where $\boldsymbol{\beta}$ is the vector of mean feature coefficients, $\boldsymbol{x}$ is the feature vector values at the location of the left and the right leads, b is the bias term, and i = 1,2,3,...,N is an index for the N subjects used in the study. The LPS value that maximized the geometric mean (g-mean) was chosen as the "optimal" threshold for the prediction of responders and non-responders. The g-mean is a performance metric that balances the correct prediction of both the majority (CRT responders) and the minority (CRT non-responders) classes [36]; it is defined as the square root of the product of the sensitivity and the specificity.

4.3 Results

4.3.1 Study Population

Out of the 147 subjects that had 4DCT scans acquired at both baseline and at 6-months follow-up, 82 subjects had images that were of sufficient quality to be usable for this study. Scans of subjects were excluded because of either helical step artifacts (37 subjects, 25%), insufficient LV blood pool-myocardium contrast (19 subjects, 13%), or severe metallic lead artifacts (9 subjects, 6%). Figure 4.3 shows a flow diagram of the subject selection process used in this study. The mean radiation dose across the 82 subjects was 4.4 ± 2.6 mSv (median: 4.1 mSv; IQR: 2 mSv). The baseline characteristics are provided in Table 4.1.

The CT-derived and the echocardiography-derived LVEFs at baseline were statistically different (37 ± 9% vs 25 ± 6%, $p < 0.001$) and poorly correlated ($r = 0.46$, $p < 0.001$).

4.3.2 Lead Placement Score and Response Prediction

Out of the 82 subjects, 52 (63%) had an ESV decrease of ≥ 15% at 6-months follow-up and were considered responders. The average weights of the 12 features that were used in training

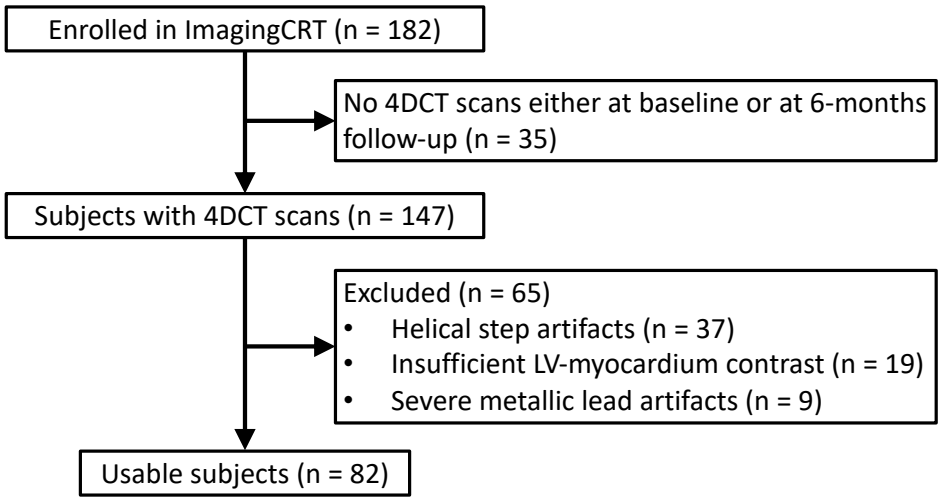

Figure 4.3: Flow diagram of the subject selection process.

the SVM model are shown in Table 4.2.

Figure 4.4 shows the relationship between the LPS and the relative change in ESV between the baseline and the follow-up scans. An LPS threshold of -0.2 maximized the geometric mean (g-mean) value for response prediction; among the subjects above this threshold, the non-responder rate was 9% (4/(4+41)), down from the original non-responder rate of 37% (30/82), and the sensitivity and the specificity at this threshold were 79% and 87%, respectively.

Figure 4.5A shows the histogram of the LPS values for all 82 subjects. The LPS of the true non-responders are shown in red while those of the true responders are shown in blue. Figure 4.5B shows the receiver operating characteristic (ROC) curve of the prediction model. The area under the curve (AUC) was 87% (95% confidence interval: 77 – 94%). Additionally, the LPS model outperformed a model defined using only clinical predictors of CRT response (see C).

There is a very practical way to stratify the subjects using the LPS. We can break the subjects into 3 groups with respect to their posttest probabilities: lower probability of response, unchanged probability, and higher probability of response. Without considering the 4DCT data,

Table 4.1: Baseline characteristics of the 82 CRT subjects.

N	82	
Female, n (%)	17 (21)	
Age, y	70.7 ± 9.1	
Body mass index, kgm^{-2}	26.5 ± 4.2	
Medical history, n (%)	Hypertension	20 (24)
	Diabetes mellitus	18 (22)
	Ischemic cardiomyopathy	42 (51)
	Myocardial infarction	28 (34)
	Coronary artery bypass graft	19 (23)
NYHA class, n (%)	II	41 (50)
	III	39 (48)
	IV	2 (2)
Atrial fibrillation, n (%)	Paroxysmal	12 (15)
	Permanent	9 (11)
Medicine, n (%)	β-blockers	75 (91)
	ACE inhibitor or angiotensin receptor blocker	78 (95)
	Loop diuretics	51 (62)
	Spironolactone	40 (49)
6-minute walk test, m	393 ± 124	
QRS width, ms	170 ± 24	
Left bundle branch block, n (%)	77 (94)	
Chronic RV pacing, n (%)	16 (20)	
Estimated glomerular filteration rate, mL/min per 1.73 m^2	66 ± 16	
CT	EDV, mL	273 ± 93
	ESV, mL	178 ± 81
	EF, %	37 ± 9
Echocardiography	EDV, mL	257 ± 85
	ESV, mL	195 ± 71
	EF, %	25 ± 6

the pretest probability of responding to CRT using the $\geq$ 15% reduction in ESV definition was 52/82 (63%). For the same response definition, by incorporating the 4DCT data, subjects with an LPS in the lowest quartile (LPS $\leq$ Q1 = -1) had a posttest probability of responding of 14% (3/21). Similarly, subjects with an LPS in the highest quartile (LPS $\geq$ Q3 = 1.3) had a

Table 4.2: Feature weights of the SVM model with the responder criterion set at % ΔESV $\leq$ -15%.

Feature name	**Feature weight for % ΔESV $\leq -15\%$**
1. EDV	0.15
2. ESV	-0.47
3. CURE-SVD	-0.33
4. LVSI	0.22
5. PRS_{CT}-right	0.45
6. PRS_{CT}-left	-0.41
7. $TPRS_{CT}$-right	0.66
8. $TPRS_{CT}$-left	-0.30
9. $MSRS_{CT}$-right	-0.57
10. $MSRS_{CT}$-left	-0.57
11. TOS-right	-0.02
12. TOS-left	1.73

posttest probability of responding of 90% (19/21), and for those subjects with an LPS within the interquartile range (IQR; Q1 $<$ LPS $<$ Q3), the posttest probability remained essentially unchanged from the pretest probability (75% vs 63%; p = 0.2).

The above analysis was performed on subjects that had already undergone CRT; hence, the precise locations of the left and the right lead tips were known. For our analysis of predicting response in these subjects, we used features of LV mechanics that were estimated from the baseline 4DCT scans at the two endocardial segments corresponding to the pacing lead tip locations. However, in general, the analysis pipeline developed can be applied to generate high resolution LV maps of LPS, aiding in the selection of target lead placement sites for achieving a higher probability of response. Fixing the location of the right lead, LPS maps were generated for the LV free wall (anterior wall to inferior wall).

Figure 4.6 shows four example subjects that highlight the significance of the LPS in identifying target lead placement sites: (a) a responder (% ΔESV = -43) with uniformly high LPS values across the entire LV free wall and the left lead placed in this region of high LPS, (b) a

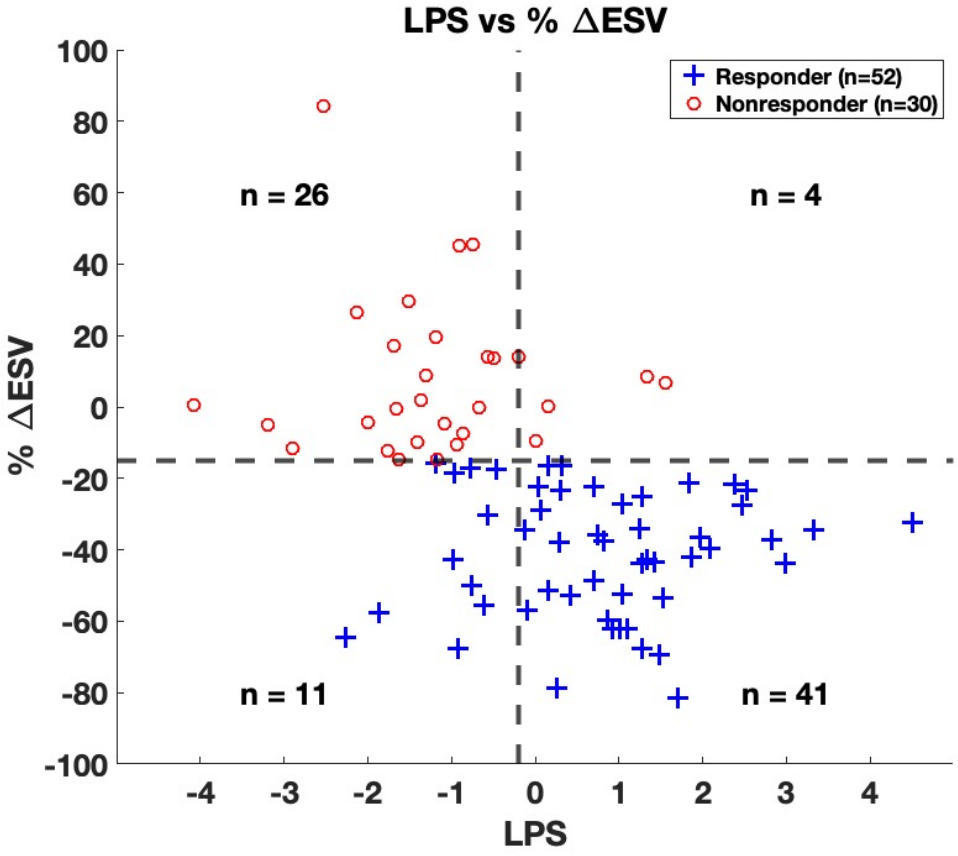

Figure 4.4: Relationship between change in ESV at 6-months follow-up and lead placement score (LPS). Distribution of LPS values for the lead locations in each subject as a function of the relative change in ESV between baseline and follow-up scans. The vertical dashed line corresponds to the LPS threshold (-0.2) that maximized the g-mean value for response prediction. The horizontal dashed line corresponds to the response definition of a relative reduction in ESV of 15%. '+' represents a true responder and 'o' represents a true non-responder. LPS: lead placement score; ESV: end systolic volume.

responder (% ΔESV = -68) with a localized region of high LPS values on the basal inferolateral wall and the left lead placed in this region of high LPS, (c) a non-responder (% ΔESV = -13) with globally low LPS values and thus the left lead placed in a region of low LPS, and (d) a non-responder (% ΔESV = +14) with a localized region of high LPS values on the basal inferolateral wall, but the left lead not placed in this region of high LPS. For each subject, polar maps of the 4 regional features of LV mechanics (TOS, PRS_{CT}, $TPRS_{CT}$, and $MSRS_{CT}$) that were used in

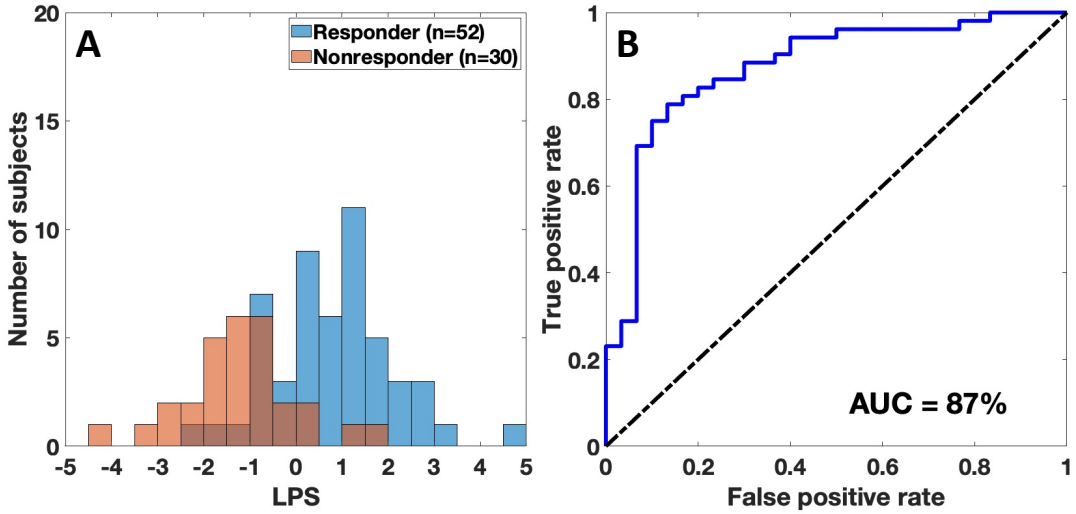

Figure 4.5: (A) Histogram of LPS for all 82 subjects. The non-responders are shown in red, and the responders are shown in blue. (B) ROC curve of the trained SVM model to predict responders as a function of changing LPS threshold. LPS: lead placement scores; ROC: receiver operating characteristic; AUC: area under curve; SVM: support vector machine.

the derivation of the LPS are shown. Additionally, the location of the right and the left lead tips are shown by the blue and red highlighted segments, respectively. Also shown are polar maps of the LPS as well as 3D renderings of the LV lateral wall with the LPS values mapped onto the endocardial surface.

4.4 Discussion

The primary objective of this study was to use known quantitative features of LV mechanics derived from baseline 4DCT scans as features in a lead placement score that correlated with CRT response. The main findings reported demonstrate the potential utility of 4DCT in guiding patient selection for CRT; in at least 42 of the 82 subjects used in the study, the LPS could have a significant impact on the decision to proceed with CRT. The study also highlights the patient-specific variation in the distribution of LPS values across the LV; some subjects had

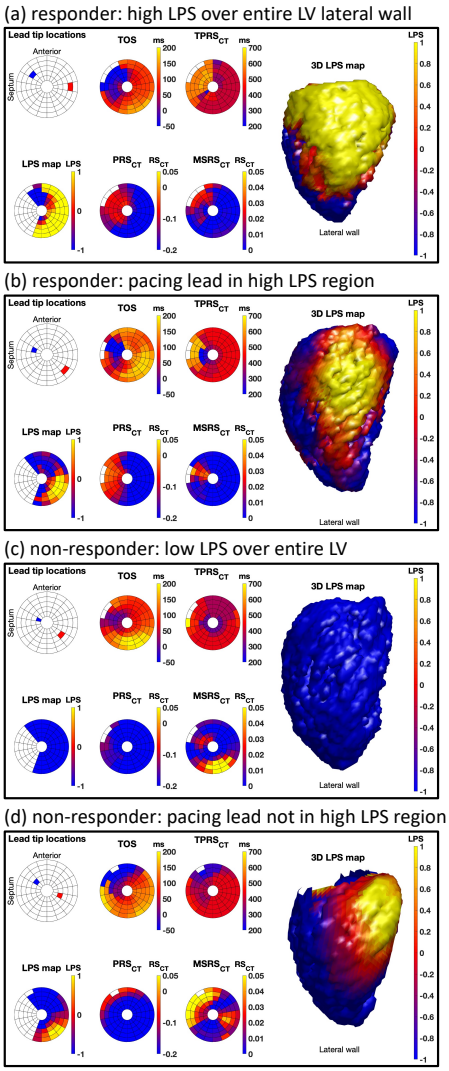

Figure 4.6: Lead placement score (LPS) maps of CRT responders and non-responders. (a-d) Four example subjects with the following information shown for each subject:
Lead tip locations: blue = right lead, red = left lead; TOS: time to onset of shortening, in ms; PRS_{CT}: peak regional shortening; $TPRS_{CT}$: time to peak regional shortening, in ms; $MSRS_{CT}$: maximum pre-stretch of regional shortening; LPS map: lead placement score map as a polar map; 3D LPS map: 3D rendering of the LV lateral wall with LPS values mapped onto the endocardial surface. (a) a responder (% ΔESV = -43) with uniformly high LPS values across the entire LV free wall and the left lead placed in this region of high LPS. (b) a responder (% ΔESV = -68) with a localized region of high LPS values on the basal inferolateral wall and the left lead placed in this region of high LPS. (c) a non-responder (% ΔESV = -13) with globally low LPS values and thus the left lead placed in a region of low LPS. (d) a non-responder (% ΔESV = +14) with a localized region of high LPS values on the basal inferolateral wall, but the left lead not placed in this region of high LPS.

large areas with high LPS values, providing multiple LV lead placement target sites for achieving a higher probability of CRT response. Other subjects had small areas with high LPS values; knowing this information may be beneficial in designing CRT delivery that is most effective. Lastly, some subjects had uniformly low LPS values across the LV; CRT may not be the optimal treatment for these subjects, especially since CRT is not without risk. Thus, the patient-specific LPS maps could aid in the optimal planning and management of patients under consideration for CRT.

4DCT scans of 147 subjects recruited for the ImagingCRT trial were retrospectively analyzed in this study. While the temporal resolution of the CT images was high because of the "dual-source" technology of the particular CT scanner used to acquire the 4DCT images, due to the limited z-axis coverage, imaging the entire superior-inferior extent of the heart was performed in helical mode. Unfortunately, 37 of the 147 subjects (25%) had severe step artifacts due to beat-to-beat irregularities, rendering the images not usable for dyssynchrony analysis. Despite the excellent temporal resolution of the dual-source scanner (66 ms per frame), wider detector scanners (256 or 320 detector-rows) with full heart coverage from a single table position may be better suited for this application, especially with the recent innovations in motion estimation and motion compensation technology [37, 38].

Despite 30 years of clinical development, no single definition of CRT response has been universally accepted [4]; however, $\geq$ 15% reduction in LV ESV is the most commonly used [2, 8] and can be measured with great precision using 4DCT. Previous studies using CT to guide CRT have used echocardiography derived LV ESV to determine response [16, 39]; however, the reproducibility of the echocardiography measures is low causing uncertainty in the results. The image-based response definition used in this study was derived from the LV blood volume

segmentations of the baseline and the follow-up 4DCT images, which are highly reproducible [40] and are free from any assumptions about LV geometry or manual contouring. For these reasons, we are confident in the precision of the 4DCT derived measurement of change in ESV as mechanical response. Additionally, the mean baseline CT-derived LVEF was higher than the echocardiography-derived LVEF due to the simple "blood pool voxel" counting used to compute LVEF from CT; this bias was expected.

To the best of our knowledge, this is the first study that combined multiple features derived from a baseline 4DCT scan into a single scalar value (the "lead placement score") that is correlated with CRT response. In addition, this paper differs from previous work using 4DCT to guide CRT in that we computed traditional dyssynchrony parameters (CURE, TOS) that have previously demonstrated a correlation with CRT response. The 4DCT scans contain an abundance of information; using a limited number of features derived from the scans for training, an SVM model was able to stratify subjects into LV mechanics responders and non-responders with high accuracy. An SVM was chosen as the desired classifier because: 1) it is less susceptible to overfitting [41] and 2) it has no local minima because it is defined by a convex optimization problem. Due to the limited number of subjects in this study, coupled with the class imbalance between the responders and the non-responders, it was not feasible to have an independent testing dataset. Thus, we implemented a bagging (bootstrap aggregation) [34] approach to overcome this limitation; bagging is an established method that improves stability and helps with overfitting [42].

The LPS was defined using a model that comprised 8 global and regional features of LV mechanics. TOS-left (time to onset of shortening at the left lead location) was the most prominent feature of the model, with its feature weight nearly three times that of the second

most prominent feature. EDV, ESV, and LVSI are features that describe the size and shape of the LV. While a reduction in ESV is itself used as an established definition of CRT response, previous studies have investigated the relationship between CRT response and EDV and LVSI [43, 44]. Dyssynchrony features such as CURE [27], TOS [12], and $TPRS_{CT}$[45] have all been shown to correlate with CRT response; the results from this study are consistent with these previously published results. Peak shortening (PRS_{CT}) and maximum pre-stretch ($MSRS_{CT}$) are features that capture the function and viability of an LV myocardial region. Low values of $PRS_{CT}$are useful in identifying regions of scar/ischemic tissue, much like late gadolinium enhancement and reduced wall thickening; pacing at these sites is to be avoided as they are correlated with CRT non-response [1]. To the best of our knowledge, the influence of maximum pre-stretch ($MSRS_{CT}$) on CRT response has not been previously reported; the results reported in this study reveal it to be a relatively important feature of the model used to stratify subjects for CRT. A large pre-stretch at either the location of the right or left lead likely detects a region of poor myocardial health which confers the observed reduction in probability of response.

The analysis pipeline adopted in this study was fully automated except for the selection of the mitral valve plane and the boundary plane between the LV chamber and the aortic outflow tract, which were performed manually using an algorithm derived from selected morphological features. The inter- and intra-user variability of this segmentation process has been previously shown to be very low, making RS_{CT}a highly reproducible metric for estimating regional endocardial function [20]. Additionally, with the advancements made in the field of deep learning cardiac image segmentation [46, 47], the entire segmentation component of the analysis pipeline will likely be fully automated in the near future.

The role of imaging in guiding CRT has been uncertain. A potential reason for this is

the high variability of measurements obtained from echocardiography [8, 48, 49]. Modern 4DCT imaging systems can acquire high resolution images of the entire heart across the full cardiac cycle very rapidly, and in the case of wide detector systems, within a single heartbeat. Therefore, these systems do not suffer from step artifacts; thus, enabling artifact-free imaging of patients with arrhythmias. Another benefit of 4DCT is its ability to image patients with implanted metallic medical devices; nearly 28% of patients in consideration for CRT have existing RV pacing systems in place [2]. Additionally, using the dynamic mA feature of the scanner, the subjects used in this study had low CT-based radiation doses (median: 4.1 mSv; IQR: 2 mSv), which is comparable to the dose received from natural sources of radiation annually [50]. The dose from CT is continuously being reduced as CT technology advances; from the 2007 and the 2017 dose surveys, the dose from coronary CT angiography was reduced by 78% (885 mGy*cm vs 195 mGy*cm, $p < 0.001$) [51]. The limits of achievable dose reduction are further being pushed by technological advancements such as iterative reconstruction, photon-counting detectors, and the use of deep learning [52].

4.4.1 Limitations

This study uses 4DCT scans of 82 subjects acquired at both baseline and at 6-months follow-up after CRT implantation. This is a unique dataset of 4DCT scans where a highly precise direct comparison of LV mechanical states can be made pre- and post-CRT. While the models derived in this study show great promise for using 4DCT in guiding patient selection for CRT, analysis of independent data and prospective trials will be required to ensure generalizability. CRT is now an accepted therapy for dyssynchronous heart failure; therefore, larger datasets are available for testing our existing model.

All 4DCT images used in this study were acquired and reconstructed with the same CT imaging system (Somatom Definition Flash, Siemens Healthcare, Erlangen, Germany); this was tremendously advantageous in facilitating a direct comparison of LPS values derived from 4DCT scans of similar image characteristics. Future studies will need to explore the effect of vendor specific differences and total radiation dose on the computed LPS values.

4.5 Conclusions

A lead placement score map was developed using features of LV mechanics that were derived from 4DCT images acquired in 82 subjects prior to CRT implantation. The LPS value at the lead locations correlated with subject response to CRT; it effectively stratified 1/4 of the subjects into low probability (14%) of response and 1/4 into high probability (90%) of response, and the remaining 1/2 had a probability of response that was unchanged from the pretest probability (75% vs 63%, p = 0.2). Additionally, an LPS threshold that maximized the geometric mean of true negative and true positive rates categorized subjects as responders and non-responders with high sensitivity (79%) and specificity (87%), with an area under the ROC curve of 87% (95% CI: 77 - 94%). These encouraging results highlight the potential utility of 4DCT in planning CRT.

Acknowledgements

This work was supported by grants from the National Institutes of Health (R01HL144678, F31HL151183, T32HL105373) and the American Heart Association (AHA 20PRE35210261). The ImagingCRT study was funded by Aarhus University, the Danish Heart Foundation (11-04-R84-A3234-22641), the Danish Council for Independent Research (11–107461), Central Denmark

Region (1-45-72-4-09), Eva and Henry Frænkels Foundation, and Manufacturer Karl G. Andersens Foundation. Dr. Nielsen was supported by a grant from the Novo Nordisk Foundation (NNF16OC0018658).

Chapter 4 is a reprint of the material: **Ashish Manohar**, Gabrielle M. Colvert, James Yang, Zhennong Chen, Maria J. Ledesma-Carbayo, Mads Brix Kronborg, Anders Sommer, Bjarne L. Nørgaard, Jens Cosedis Nielsen, and Elliot R. McVeigh. "Prediction of CRT response using a lead placement score derived from 4DCT" *medRxiv*, DOI:10.1101/2022.03.23.22272846, 2022. The dissertation author is the primary author.

4.6 References

1. Prinzen, F. W., Vernooy, K. & Auricchio, A. Cardiac Resynchronization Therapy. *Circulation* **128,** 2407–2418. ISSN: 0009-7322. https://www.ahajournals.org/doi/10.1161/CIRCULATIONAHA.112.000112 (Nov. 2013).

2. Daubert, J.-C., Saxon, L., Adamson, P. B., Auricchio, A., Berger, R. D., Beshai, J. F., Breithard, O., Brignole, M., Cleland, J., DeLurgio, D. B., Dickstein, K., Exner, D. V., Gold, M., Grimm, R. A., Hayes, D. L., Israel, C., Leclercq, C., Linde, C., Lindenfeld, J., Merkely, B., Mont, L., Murgatroyd, F., Prinzen, F., Saba, S. F., Shinbane, J. S., Singh, J., Tang, A. S., Vardas, P. E., Wilkoff, B. L., Zamorano, J. L., Anand, I., Blomstrom-Lundqvist, C., Boehmer, J. P., Calkins, H., Cazeau, S., Delgado, V., Estes, N. A. M., Haines, D., Kusumoto, F., Leyva, P., Ruschitzka, F., Stevenson, L. W. & Torp-Pedersen, C. T. 2012 EHRA/HRS expert consensus statement on cardiac resynchronization therapy in heart failure: implant and follow-up recommendations and management: A registered branch of the European Society of Cardiology (ESC), and the Heart Rhythm Society; and in col. *Europace* **14,** 1236–1286. ISSN: 1099-5129. https://academic.oup.com/europace/article-lookup/doi/10.1093/europace/eus222 (Sept. 2012).

3. Vernooy, K., van Deursen, C. J. M., Strik, M. & Prinzen, F. W. Strategies to improve cardiac resynchronization therapy. *Nature Reviews Cardiology* **11,** 481–493. ISSN: 1759-5002. http://www.nature.com/articles/nrcardio.2014.67 (Aug. 2014).

4. Daubert, C., Behar, N., Martins, R. P., Mabo, P. & Leclercq, C. Avoiding non-responders to cardiac resynchronization therapy: a practical guide. *European Heart Journal* **38,** ehw270. ISSN: 0195-668X. http://eurheartj.oxfordjournals.org/lookup/doi/10.1093/eurheartj/ehw270 (July 2016).

5. Marek, J., Gandalovičová, J., Kejřová, E., Pšenička, M., Linhart, A. & Paleček, T. Echocardiography and cardiac resynchronization therapy. *Cor et Vasa* **58,** e340–e351. ISSN: 00108650. http://e-coretvasa.cz/doi/10.1016/j.crvasa.2015.08.001.html (June 2016).

6. Khan, F. Z., Virdee, M. S., Palmer, C. R., Pugh, P. J., O'Halloran, D., Elsik, M., Read, P. A., Begley, D., Fynn, S. P. & Dutka, D. P. Targeted Left Ventricular Lead Placement to Guide Cardiac Resynchronization Therapy. *Journal of the American College of Cardiology* **59,** 1509–1518. ISSN: 07351097. https://linkinghub.elsevier.com/retrieve/pii/S0735109712003725 (Apr. 2012).

7. VITARELLI, A., FRANCIOSA, P. & ROSANIO, S. Tissue Doppler Imaging in the assessment of selection and response from cardiac resynchronization therapy. *European Journal of Echocardiography* **8,** 309–316. ISSN: 15252167. https://academic.oup.com/ehjcimaging/article-lookup/doi/10.1016/j.euje.2006.12.005 (Oct. 2007).

8. Chung, E. S., Leon, A. R., Tavazzi, L., Sun, J.-P., Nihoyannopoulos, P., Merlino, J., Abraham, W. T., Ghio, S., Leclercq, C., Bax, J. J., Yu, C.-M., Gorcsan, J., St John Sutton, M., De Sutter, J. & Murillo, J. Results of the Predictors of Response to CRT (PROSPECT) Trial. *Circulation* **117,** 2608–2616. ISSN: 0009-7322. https://www.ahajournals.org/doi/10.1161/CIRCULATIONAHA.107.743120 (May 2008).

9. Leyva, F. Cardiac resynchronization therapy guided by cardiovascular magnetic resonance. *Journal of Cardiovascular Magnetic Resonance* **12,** 64. ISSN: 1532-429X. https://jcmr-online.biomedcentral.com/articles/10.1186/1532-429X-12-64 (Dec. 2010).

10. Taylor, R. J., Umar, F., Panting, J. R., Stegemann, B. & Leyva, F. Left ventricular lead position, mechanical activation, and myocardial scar in relation to left ventricular reverse remodeling and clinical outcomes after cardiac resynchronization therapy: A feature-tracking and contrast-enhanced cardiovascular magnetic r. *Heart Rhythm* **13,** 481–489. ISSN: 15475271. https://linkinghub.elsevier.com/retrieve/pii/S1547527115013053 (Feb. 2016).

11. McVeigh, E. R., Prinzen, F. W., Wyman, B. T., Tsitlik, J. E., Halperin, H. R. & Hunter, W. C. Imaging asynchronous mechanical activation of the paced heart with tagged MRI. *Magnetic Resonance in Medicine* **39,** 507–513. ISSN: 07403194. http://doi.wiley.com/10.1002/mrm.1910390402 (Apr. 1998).

12. Auger, D. A., Bilchick, K. C., Gonzalez, J. A., Cui, S. X., Holmes, J. W., Kramer, C. M., Salerno, M. & Epstein, F. H. Imaging left-ventricular mechanical activation in heart failure patients using cine DENSE MRI: Validation and implications for cardiac resynchronization therapy. *Journal of Magnetic Resonance Imaging* **46,** 887–896. ISSN: 10531807. http://doi.wiley.com/10.1002/jmri.25613%20https://onlinelibrary.wiley.com/doi/10.1002/jmri.25613 (Sept. 2017).

13. Shetty, A. K., Duckett, S. G., Ginks, M. R., Ma, Y., Sohal, M., Bostock, J., Kapetanakis, S., Singh, J. P., Rhode, K., Wright, M., O'Neill, M. D., Gill, J. S., Carr-White, G., Razavi, R. & Rinaldi, C. A. Cardiac magnetic resonance-derived anatomy, scar, and dyssynchrony

fused with fluoroscopy to guide LV lead placement in cardiac resynchronization therapy: a comparison with acute haemodynamic measures and echocardiographic reverse remodelling. *European Heart Journal - Cardiovascular Imaging* **14,** 692–699. ISSN: 2047-2404. https://academic.oup.com/ehjcimaging/article-lookup/doi/10.1093/ehjci/jes270 (July 2013).

14. Truong, Q. A., Szymonifka, J., Picard, M. H., Thai, W.-e., Wai, B., Cheung, J. W., Heist, E. K., Hoffmann, U. & Singh, J. P. Utility of dual-source computed tomography in cardiac resynchronization therapy—DIRECT study. *Heart Rhythm* **15,** 1206–1213. ISSN: 15475271. https://doi.org/10.1016/j.hrthm.2018.03.020%20https://linkinghub.elsevier.com/retrieve/pii/S1547527118302340 (Aug. 2018).

15. Behar, J. M., Rajani, R., Pourmorteza, A., Preston, R., Razeghi, O., Niederer, S., Adhya, S., Claridge, S., Jackson, T., Sieniewicz, B., Gould, J., Carr-White, G., Razavi, R., McVeigh, E. & Rinaldi, C. A. Comprehensive use of cardiac computed tomography to guide left ventricular lead placement in cardiac resynchronization therapy. *Heart Rhythm* **14,** 1364–1372. ISSN: 15475271. http://dx.doi.org/10.1016/j.hrthm.2017.04.041%20https://linkinghub.elsevier.com/retrieve/pii/S154752711730574X (Sept. 2017).

16. Gould, J., Sidhu, B. S., Sieniewicz, B. J., Porter, B., Lee, A. W. C., Razeghi, O., Behar, J. M., Mehta, V., Elliott, M. K., Toth, D., Haberland, U., Razavi, R., Rajani, R., Niederer, S. & Rinaldi, C. A. Feasibility of intraprocedural integration of cardiac CT to guide left ventricular lead implantation for CRT upgrades. *Journal of Cardiovascular Electrophysiology* **32,** 802–812. ISSN: 1045-3873. https://onlinelibrary.wiley.com/doi/10.1111/jce.14896 (Mar. 2021).

17. Fyenbo, D. B., Sommer, A., Kühl, J. T., Kofoed, K. F., Nørgaard, B. L., Kronborg, M. B., Bouchelouche, K. & Nielsen, J. C. Transmural Myocardial Scar Assessed by Cardiac Computed Tomography. *Journal of Computer Assisted Tomography* **43,** 312–316. ISSN: 0363-8715. http://journals.lww.com/00004728-201903000-00024 (2019).

18. Sommer, A., Kronborg, M. B., Poulsen, S. H., Bttcher, M., Nrgaard, B. L., Bouchelouche, K., Mortensen, P. T., Gerdes, C. & Nielsen, J. C. Empiric versus imaging guided left ventricular lead placement in cardiac resynchronization therapy (ImagingCRT): study protocol for a randomized controlled trial. *Trials* **14,** 113. ISSN: 1745-6215. http://trialsjournal.biomedcentral.com/articles/10.1186/1745-6215-14-113 (2013).

19. Sommer, A., Kronborg, M. B., Nørgaard, B. L., Poulsen, S. H., Bouchelouche, K., Böttcher, M., Jensen, H. K., Jensen, J. M., Kristensen, J., Gerdes, C., Mortensen, P. T. & Nielsen, J. C. Multimodality imaging-guided left ventricular lead placement in cardiac resynchronization therapy: a randomized controlled trial. *European Journal of Heart Failure* **18,** 1365–1374. ISSN: 13889842. https://academic.oup.com/europace/article/21/9/1369/5528508%20https://onlinelibrary.wiley.com/doi/10.1002/ejhf.530 (Nov. 2016).

20. Colvert, G. M., Manohar, A., Contijoch, F. J., Yang, J., Glynn, J., Blanke, P., Leipsic, J. A. & McVeigh, E. R. Novel 4DCT Method to Measure Regional Left Ventricular Endocardial

Shortening Before and After Transcatheter Mitral Valve Implantation. *Structural Heart* **5,** 410–419. ISSN: 2474-8706. https://doi.org/10.1080/24748706.2021.1934617%20https://www.tandfonline.com/doi/full/10.1080/24748706.2021.1934617 (July 2021).

21. Manohar, A., Colvert, G. M., Schluchter, A., Contijoch, F. & McVeigh, E. R. Anthropomorphic left ventricular mesh phantom: a framework to investigate the accuracy of SQUEEZ using Coherent Point Drift for the detection of regional wall motion abnormalities. *Journal of Medical Imaging* **6,** 1. ISSN: 2329-4302. https://www.spiedigitallibrary.org/journals/journal-of-medical-imaging/volume-6/issue-04/045001/Anthropomorphic-left-ventricular-mesh-phantom--a-framework-to-investigate/10.1117/1.JMI.6.4.045001.full (Dec. 2019).

22. Yushkevich, P. A., Piven, J., Hazlett, H. C., Smith, R. G., Ho, S., Gee, J. C. & Gerig, G. User-guided 3D active contour segmentation of anatomical structures: Significantly improved efficiency and reliability. *NeuroImage* **31,** 1116–1128. ISSN: 10538119. https://linkinghub.elsevier.com/retrieve/pii/S1053811906000632 (July 2006).

23. McVeigh, E. R., Pourmorteza, A., Guttman, M., Sandfort, V., Contijoch, F., Budhiraja, S., Chen, Z., Bluemke, D. A. & Chen, M. Y. Regional myocardial strain measurements from 4DCT in patients with normal LV function. *Journal of Cardiovascular Computed Tomography* **12,** 372–378. ISSN: 19345925. https://doi.org/10.1016/j.jcct.2018.05.002%20https://linkinghub.elsevier.com/retrieve/pii/S1934592518300923 (Sept. 2018).

24. Contijoch, F. J., Groves, D. W., Chen, Z., Chen, M. Y. & McVeigh, E. R. A novel method for evaluating regional RV function in the adult congenital heart with low-dose CT and SQUEEZ processing. *International Journal of Cardiology* **249,** 461–466. ISSN: 01675273. https://doi.org/10.1016/j.ijcard.2017.08.040%20https://linkinghub.elsevier.com/retrieve/pii/S0167527317334460 (Dec. 2017).

25. Leclercq, C., Faris, O., Tunin, R., Johnson, J., Kato, R., Evans, F., Spinelli, J., Halperin, H., McVeigh, E. & Kass, D. A. Systolic Improvement and Mechanical Resynchronization Does Not Require Electrical Synchrony in the Dilated Failing Heart With Left Bundle-Branch Block. *Circulation* **106,** 1760–1763. ISSN: 0009-7322. https://www.ahajournals.org/doi/10.1161/01.CIR.0000035037.11968.5C (Oct. 2002).

26. Helm, R. H., Leclercq, C., Faris, O. P., Ozturk, C., McVeigh, E., Lardo, A. C. & Kass, D. A. Cardiac Dyssynchrony Analysis Using Circumferential Versus Longitudinal Strain. *Circulation* **111,** 2760–2767. ISSN: 0009-7322. https://www.ahajournals.org/doi/10.1161/CIRCULATIONAHA.104.508457 (May 2005).

27. Ramachandran, R., Chen, X., Kramer, C. M., Epstein, F. H. & Bilchick, K. C. Singular Value Decomposition Applied to Cardiac Strain from MR Imaging for Selection of Optimal Cardiac Resynchronization Therapy Candidates. *Radiology* **275,** 413–420. ISSN: 0033-8419. http://pubs.rsna.org/doi/10.1148/radiol.14141578 (May 2015).

28. Ambale-Venkatesh, B., Yoneyama, K., Sharma, R. K., Ohyama, Y., Wu, C. O., Burke, G. L., Shea, S., Gomes, A. S., Young, A. A., Bluemke, D. A. & Lima, J. A. Left ventricular shape predicts different types of cardiovascular events in the general population. *Heart* **103,** 499–507. ISSN: 1355-6037. https://heart.bmj.com/lookup/doi/10.1136/heartjnl-2016-310052 (Apr. 2017).

29. Myronenko, A. & Xubo Song. Point Set Registration: Coherent Point Drift. *IEEE Transactions on Pattern Analysis and Machine Intelligence* **32,** 2262–2275. ISSN: 0162-8828. arXiv: 0905.2635. http://arxiv.org/abs/0905.2635%7B%5C%%7D0Ahttp://dx.doi.org/10.1109/TPAMI.2010.46%20http://www.ncbi.nlm.nih.gov/pubmed/20975122%20http://ieeexplore.ieee.org/document/5432191/ (Dec. 2010).

30. Wyman, B. T., Hunter, W. C., Prinzen, F. W. & McVeigh, E. R. Mapping propagation of mechanical activation in the paced heart with MRI tagging. *American Journal of Physiology-Heart and Circulatory Physiology* **276,** H881–H891. ISSN: 0363-6135. https://www.physiology.org/doi/10.1152/ajpheart.1999.276.3.H881 (Mar. 1999).

31. Wyman, B. T., Hunter, W. C., Prinzen, F. W., Faris, O. P. & McVeigh, E. R. Effects of single- and biventricular pacing on temporal and spatial dynamics of ventricular contraction. *American Journal of Physiology-Heart and Circulatory Physiology* **282,** H372–H379. ISSN: 0363-6135. https://www.physiology.org/doi/10.1152/ajpheart.2002.282.1.H372 (Jan. 2002).

32. Feeny, A. K., Rickard, J., Patel, D., Toro, S., Trulock, K. M., Park, C. J., LaBarbera, M. A., Varma, N., Niebauer, M. J., Sinha, S., Gorodeski, E. Z., Grimm, R. A., Ji, X., Barnard, J., Madabhushi, A., Spragg, D. D. & Chung, M. K. Machine Learning Prediction of Response to Cardiac Resynchronization Therapy. *Circulation: Arrhythmia and Electrophysiology* **12,** 1–12. ISSN: 1941-3149. https://www.ahajournals.org/doi/10.1161/CIRCEP.119.007316 (July 2019).

33. He, H. & Ma, Y. *Imbalanced Learning: Foundations, Algorithms, and Applications* (eds He, H. & Ma, Y.) ISBN: 9781118074626. https://onlinelibrary.wiley.com/doi/book/10.1002/9781118646106 (Wiley, June 2013).

34. Bauer, E. & Kohavi, R. Empirical comparison of voting classification algorithms: bagging, boosting, and variants. *Machine Learning* **36,** 105–139. ISSN: 08856125 (1999).

35. Donders, A. R. T., van der Heijden, G. J., Stijnen, T. & Moons, K. G. Review: A gentle introduction to imputation of missing values. *Journal of Clinical Epidemiology* **59,** 1087–1091. ISSN: 08954356. https://linkinghub.elsevier.com/retrieve/pii/S0895435606001971 (Oct. 2006).

36. Lin, W.-J. & Chen, J. J. Class-imbalanced classifiers for high-dimensional data. *Briefings in Bioinformatics* **14,** 13–26. ISSN: 1467-5463. https://academic.oup.com/bib/article-lookup/doi/10.1093/bib/bbs006 (Jan. 2013).

37. Nett, B. E., Pack, J. D. & Okerlund, D. *Task based assessment of a motion compensation algorithm via simulation of a moving stenotic vessel* in *Medical Imaging 2013: Physics of Medical Imaging* (eds Nishikawa, R. M. & Whiting, B. R.) (Mar. 2013), 86682B. ISBN: 9780819494429. http://proceedings.spiedigitallibrary.org/proceeding.aspx?doi=10.1117/12.2006593.

38. Manohar, A., Pack, J. D., Schluchter, A. J. & McVeigh, E. R. Four-dimensional computed tomography of the left ventricle, Part II: Estimation of mechanical activation times. *Medical Physics.* ISSN: 0094-2405. https://onlinelibrary.wiley.com/doi/10.1002/mp.15550 (Mar. 2022).

39. Kronborg, M. B., Sommer, A., Fyenbo, D. B., Norgaard, B. L., Gerdes, C., Jensen, J. M., Jensen, H. K., Kristensen, J. & Nielsen, J. C. Left ventricular regional remodeling and lead position during cardiac resynchronization therapy. *Heart Rhythm* **15,** 1542–1549. ISSN: 15475271. https://doi.org/10.1016/j.hrthm.2018.04.012%20https://linkinghub.elsevier.com/retrieve/pii/S1547527118303552 (Oct. 2018).

40. Sugeng, L., Mor-Avi, V., Weinert, L., Niel, J., Ebner, C., Steringer-Mascherbauer, R., Schmidt, F., Galuschky, C., Schummers, G., Lang, R. M. & Nesser, H. J. Quantitative assessment of left ventricular size and function: Side-by-side comparison of real-time three-dimensional echocardiography and computed tomography with magnetic resonance reference. *Circulation* **114,** 654–661. ISSN: 00097322 (2006).

41. Cortes, C. & Vapnik, V. Support-vector networks. *Machine Learning* **20,** 273–297. ISSN: 0885-6125. http://link.springer.com/10.1007/BF00994018 (Sept. 1995).

42. Sukhanov, S., Merentitis, A., Debes, C., Hahn, J. & Zoubir, A. M. *Bootstrap-based SVM aggregation for class imbalance problems* in *2015 23rd European Signal Processing Conference (EUSIPCO)* (IEEE, Aug. 2015), 165–169. ISBN: 978-0-9928-6263-3. http://ieeexplore.ieee.org/document/7362366/.

43. Matsumoto, K., Tanaka, H., Okajima, K., Hayashi, T., Kajiya, T., Sugiyama, D., Kawai, H. & Hirata, K.-i. Reverse remodelling induces progressive ventricular resynchronization after cardiac resynchronization therapy 'from vicious to virtuous cycle'. *European Journal of Echocardiography* **12,** 782–789. ISSN: 1525-2167. https://academic.oup.com/ehjcimaging/article-lookup/doi/10.1093/ejechocard/jer143 (Oct. 2011).

44. St John Sutton, M. G., Plappert, T., Abraham, W. T., Smith, A. L., DeLurgio, D. B., Leon, A. R., Loh, E., Kocovic, D. Z., Fisher, W. G., Ellestad, M., Messenger, J., Kruger, K., Hilpisch, K. E. & Hill, M. R. Effect of Cardiac Resynchronization Therapy on Left Ventricular Size and Function in Chronic Heart Failure. *Circulation* **107,** 1985–1990. ISSN: 0009-7322. https://www.ahajournals.org/doi/10.1161/01.CIR.0000065226.24159.E9 (Apr. 2003).

45. Kydd, A. C., Khan, F. Z., O'Halloran, D., Pugh, P. J., Virdee, M. S. & Dutka, D. P. Radial Strain Delay Based on Segmental Timing and Strain Amplitude Predicts Left Ventricular Reverse Remodeling and Survival After Cardiac Resynchronization Therapy. *Circulation:*

Cardiovascular Imaging **6,** 177–184. ISSN: 1941-9651. https://www.ahajournals.org/doi/10.1161/CIRCIMAGING.112.000191 (Mar. 2013).

46. Chen, C., Qin, C., Qiu, H., Tarroni, G., Duan, J., Bai, W. & Rueckert, D. Deep Learning for Cardiac Image Segmentation: A Review. *Frontiers in Cardiovascular Medicine* **7.** ISSN: 2297-055X. arXiv: 1911.03723. https://www.frontiersin.org/article/10.3389/fcvm.2020.00025/full (Mar. 2020).

47. Vigneault, D. M., Contijoch, F., Bridge, C. P., Lowe, K., Jan, C. & McVeigh, E. R. *M-SiSSR: Regional Endocardial Function Using Multilabel Simultaneous Subdivision Surface Registration* in *Functional Imaging and Modeling of the Heart* (Springer, Cham, 2021), 242–252. https://link.springer.com/10.1007/978-3-030-78710-3%7B%5C_%7D24.

48. Mirea, O., Pagourelias, E. D., Duchenne, J., Bogaert, J., Thomas, J. D., Badano, L. P., Voigt, J.-U., Badano, L. P., Thomas, J. D., Hamilton, J., Pedri, S., Lysyansky, P., Hansen, G., Ito, Y., Chono, T., Vogel, J., Prater, D., Park, S., Lee, J. Y., Houle, H., Georgescu, B., Baumann, R., Mumm, B., Abe, Y. & Gorissen, W. Variability and Reproducibility of Segmental Longitudinal Strain Measurement. *JACC: Cardiovascular Imaging* **11,** 15–24. ISSN: 1936878X. https://linkinghub.elsevier.com/retrieve/pii/S1936878X17303601 (Jan. 2018).

49. Mirea, O., Pagourelias, E. D., Duchenne, J., Bogaert, J., Thomas, J. D., Badano, L. P., Voigt, J.-U., Badano, L. P., Thomas, J. D., Hamilton, J., Pedri, S., Lysyansky, P., Hansen, G., Ito, Y., Chono, T., Vogel, J., Prater, D., Park, S., Lee, J. Y., Houle, H., Georgescu, B., Baumann, R., Mumm, B., Abe, Y. & Gorissen, W. Intervendor Differences in the Accuracy of Detecting Regional Functional Abnormalities. *JACC: Cardiovascular Imaging* **11,** 25–34. ISSN: 1936878X. https://linkinghub.elsevier.com/retrieve/pii/S1936878X17303637 (Jan. 2018).

50. McCollough, C. H., Primak, A. N., Braun, N., Kofler, J., Yu, L. & Christner, J. Strategies for Reducing Radiation Dose in CT. *Radiologic Clinics of North America* **47,** 27–40. ISSN: 00338389. https://linkinghub.elsevier.com/retrieve/pii/S0033838908001863 (Jan. 2009).

51. Stocker, T. J., Deseive, S., Leipsic, J., Hadamitzky, M., Chen, M. Y., Rubinshtein, R., Heckner, M., Bax, J. J., Fang, X.-M., Grove, E. L., Lesser, J., Maurovich-Horvat, P., Otton, J., Shin, S., Pontone, G., Marques, H., Chow, B., Nomura, C. H., Tabbalat, R., Schmermund, A., Kang, J.-W., Naoum, C., Atkins, M., Martuscelli, E., Massberg, S., Hausleiter, J., Carrascosa, P., Deviggiano, A., Naoum, C., Magnussen, J., Otton, J., Kaplan, A., Feuchtner, G., Plank, F., De Smet, K., Buls, N., Cury, R. C., Bittencourt, M. S., Nomura, C. H., Dantas, R. N., Leipsic, J., Blanke, P., Chartrand-Lefebvre, C., Chin, A., Small, G., Chow, B., Silva F, C., Godoy Z, M., Silva F, C., Fang, X.-M., Jie, W., Cadena, A., Adla, T., Suchanek, V., Grove, E. L., Pedersen, K. B., Lambrechtsen, J., Husic, M., Knuuti, J., Maaniitty, T., Bischoff, B., Arnoldi, E., Schmermund, A., Eckert, J., Hadamitzky, M., Finck, T., Hell, M., Marwan, M., Bamberg, F., Mangold, S., Schlosser, T., Ludwig, J., Mylona, M., Skiadopoulos, S., Maurovich-Horvat, P., Szilveszter, B., Jadav, U., Pinto, B. V., Rubinshtein,

R., Hussein, E., Andreini, D., Pontone, G., Martuscelli, E., Sperandio, M., Kitagawa, K., Nagasawa, N., Tabbalat, R., Farhan, R. A., Sierra Galán, L. M., Delgado, L. A., Sierra Galán, L. M., Reza Orozco, M. A., Castellón, F. C., Zamudio, M. D., Preciado-Anaya, A., Gómez, R. P., Forsdahl, S. H., Hansen, G. A., Günther, A., Kristiansen, J. F., Huapalla, E. C., Chavez, P. T., Marques, H., de A Goncalves, P., Ramanathan, S., Sinitsyn, V., Glazkova, M., Abazid, R., Smettei, O. A., Dawood, A., Omar, S. H., Kang, J.-W., Yang, D. H., Kim, T. H., Park, C. H., Shin, S., Ryu, S. J., Palomares, J. R., Cuellar, H., Bax, J. J., van Rosendael, A., Williams, M. C., Newby, D., van Beek, E. J. R., Bull, R., Jayawardhana, K., Dickson, P., Espey, J., Lesser, J., Han, B. K., Bullock-Palmer, R., Rabbat, M., Schoenecker, N., Thomas, D. M., Gore, R. S., Atkins, M., Chen, M. Y., Shanbhag, S. M., Mahmarian, J., Yu, J., Villines, T. C. & Nguyen, B. Reduction in radiation exposure in cardiovascular computed tomography imaging: results from the PROspective multicenter registry on radiaTion dose Estimates of cardiac CT angIOgraphy iN daily practice in 2017 (PROTECTION VI). *European Heart Journal* **39,** 3715–3723. ISSN: 0195-668X. `https://academic.oup.com/eurheartj/article/39/41/3715/5079037` (Nov. 2018).

52. Lell, M. M. & Kachelrieß, M. Recent and Upcoming Technological Developments in Computed Tomography. *Investigative Radiology* **55,** 8–19. ISSN: 0020-9996. `http://journals.lww.com/00004424-202001000-00002` (Jan. 2020).

Chapter 5

Clinical utility of motion-corrected cardiac 4DCT images in the estimation of left ventricular mechanical activation times

In chapter 3, we demonstrated that 4DCT with the ResyncCT motion correction algorithm yields estimates of mechanical activation times of left ventricular (LV) wall motion with significantly improved accuracy and precision under controlled phantom experiments. In chapter 4, the time to onset of shortening at the proposed site of implantation of the left lead was the most important feature of the lead placement score (LPS) model; thus, the accurate and precise estimation of LV mechanical activation times can potentially have a significant impact in predicting the probability of a patient responding to cardiac resynchronization therapy (CRT). This

chapter investigates the clinical applicability of ResyncCT in the estimation of LV mechanical activation times.

5.1 Background

Cardiac resynchronization therapy (CRT) is an effective treatment for patients in heart failure and with left ventricular (LV) dyssynchrony [1]; however, 30-50% of patients selected for CRT do not respond to the treatment [2]. Current guidelines for CRT patient selection include echocardiography-derived left ventricular ejection fractions (LVEF) $\leq$ 35%, New York Heart Association (NYHA) functional classes II-IV, and QRS durations $>$ 120 ms [3]. Significant effort has been focused on reducing this non-responder rate through more effective patient selection with the use of non-invasive imaging, primarily with echocardiography, but with limited success thus far [4, 5].

Cardiac magnetic resonance (CMR) has been shown to be an excellent modality for the accurate and reproducible estimation of timing of mechanical events of the LV [6–8]. CMR-derived estimates of LV mechanical activation have also been shown to be strongly correlated with CRT response [9–11]; thus, establishing LV mechanical activation as an important parameter for predicting CRT response. However, the complexity and limited availability of highly skilled CMR centers has hindered its routine clinical use. Additionally, 28% of patients under consideration for CRT already have existing right ventricular (RV) pacing systems in place, serving as a contraindication for CMR imaging in many of these patients [3].

Four-dimensional x-ray computed tomography (4DCT) can yield high-resolution 3D volumetric images across the cardiac cycle with low radiation dose [12]. The images can also be acquired using routine FDA approved scanning protocols available from all vendors which do not

require specially trained personnel. Previous studies have successfully used dual-source 4DCT for LV dyssynchrony assessment and CRT planning [13–15]. Dual-source scanners offer higher temporal resolution; however, due to their limited z-axis detector coverage, they can suffer from step-artifacts that arise during helical acquisition of the superior-inferior extent of the heart over multiple irregular heartbeats. We previously reported that out of 147 subjects recruited for a retrospective CRT study, 37 subjects (25%) had severe step-artifacts preventing the precise estimation of LV mechanics [16]. With the advances made in 4DCT motion correction technology [17], wide detector scanners can now yield high temporal resolution images, together with the advantages of single-heartbeat and single-table position acquisitions [18]; the 'false dyssynchrony' artifact [19, 20] can also be significantly reduced [21]. These favorable features of 4DCT are of particular value in the accurate and precise estimation of LV mechanical activation times, highlighting the potential utility of wide detector 4DCT systems in guiding CRT planning.

In addition to the CMR-derived estimates of LV mechanical activation, we have also previously shown that the 'time to onset of shortening' (TOS) at the proposed implantation site of the LV left lead is a very important feature in predicting CRT response [16]. Thus, the objective of this study was to assess the effect of a newly developed cardiac CT motion correction algorithm called ResyncCT on the computed TOS estimates in a clinical cohort of 25 subjects. ResyncCT has previously been validated using a set of controlled phantom experiments [21]; this study presents new results which focus on the clinical applicability and the effect of ResyncCT on routinely acquired retrospective cardiac 4DCT images in human subjects.

5.2 Methods

5.2.1 Subjects

Twenty-five consecutive subjects that underwent 4DCT exams between January 2018 and July 2021 for the evaluation and planning of transcatheter aortic valve replacement (TAVR) and that were clinically diagnosed as having "normal LV function" were included in this study. The scans were acquired and read by radiologists at the University of California San Diego (UCSD). Neither subject enrolment, image acquisition, image reconstruction, nor clinical diagnosis was modified for the purpose of this particular study; the subjects were scanned and images diagnosed as per routine clinical protocols established at UCSD for pre-TAVR evaluation. The de-identified images of these subjects were retrospectively used in this study in accordance with an IRB approved protocol.

5.2.2 4DCT Imaging and Left Ventricle Segmentation

The 25 subjects were scanned with a 256-detector row scanner (Revolution CT, General Electric Healthcare, Chicago, IL) under an established clinical imaging protocol for TAVR assessment at UCSD. The protocol included retrospective ECG-gated single-heartbeat full cardiac cycle imaging with no x-ray tube current modulation. The 256-detector row scanner has a z-axis coverage of 16 cm, permitting full heart volume imaging from a single table position. The gantry revolution time was 280 ms. The scans were acquired with tube voltages of 80 kVp (n = 2), 100 kVP (n = 21), and 120 kVp (n = 2) and tube currents of 340 mA (n = 2), 440 mA (n = 2), 600 mA (n = 3), 660 mA (n = 2), and 720 mA (n = 16). The images were reconstructed at 70 ms intervals (90 degrees of rotation for a gantry revolution time of 280 ms) using the 'Standard' reconstruction kernel of the Revolution CT into 512 x 512 x 256 voxels. The in-plane pixel

spacings were in the range of [0.31, 0.53] mm with a slice thickness of 0.625 mm for all images.

The reconstructed 4DCT images of each subject exhibited motion artifacts that are dependent on the direction of motion of the endocardial walls with respect to gantry position; these artifacts rotate synchronously with the orientation of the gantry, giving a false impression of dyssynchronous contraction [19]. The motion uncorrected images are referred to hereafter as the uncorrected images. These gantry position induced artifacts make it very difficult to accurately measure the mechanical activation time of regions of the LV because of the uncertainty of endocardial wall position in the images. The uncorrected images were processed with a motion correction algorithm called ResyncCT [21] to yield motion corrected images. ResyncCT is a newly developed cardiac CT motion correction algorithm that leverages the power of conjugate pairs of partial angle reconstruction images for motion estimation and motion compensation. The motion corrected images are referred to hereafter as the ResyncCT images. Figure 5.1 shows an axial CT slice in an example subject with and without motion correction demonstrating the clarification of endocardial wall position in the corrected image.

For each subject, the LV blood volume was segmented from each time frame of the uncorrected and the ResyncCT image series. The segmentation procedure has been previously described in detail [22]. Briefly, the segmentation threshold was determined using Otsu's method [23] and the active contour region growing module of ITK-SNAP v3.8.0 [24] was used to segment the LV blood volume. The volume of the LV for each time frame was computed by summing the segmented 3D voxels. Meshes delineating the LV endocardium were then extracted from the segmented LV volumes.

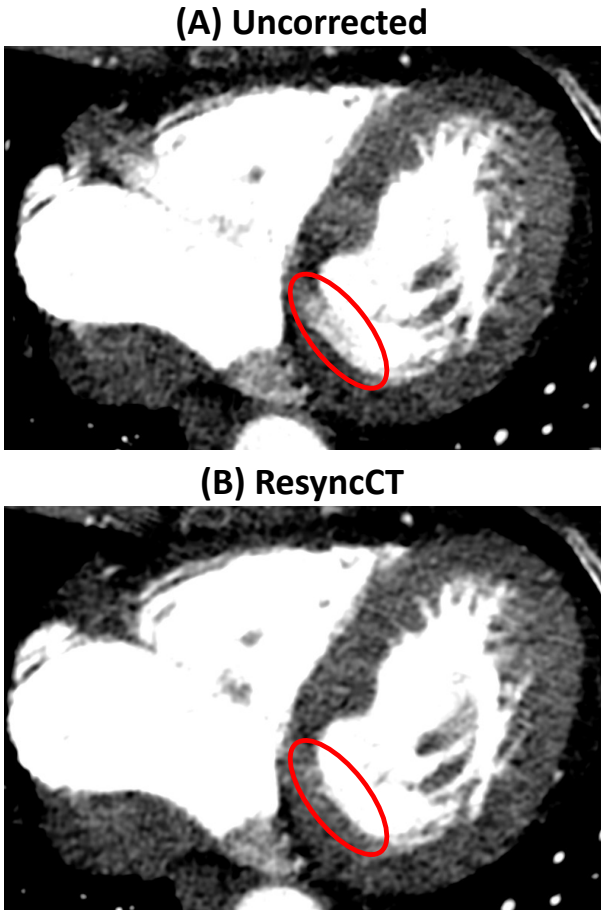

Figure 5.1: Reconstructed axial CT slice in an example subject showing motion artifact. (A) Uncorrected CT image showing pronounced "double-wall" motion artifact highlighted by the red ellipse. (B) ResyncCT image showing significant reduction of the "double-wall" artifact, and clarification of the position of the endocardial wall.

5.2.3 Endocardial Regional Shortening

Endocardial regional shortening (RS_{CT}) [25–27] was estimated by registering the end diastolic LV mesh to each subsequent mesh derived from the other time frames of the cardiac cycle using a point set registration technique [28] and was computed according to the following equation:

$$RS_{\mathrm{CT}}(\nu,t) = \sqrt{\frac{A(\nu,t)}{A(\nu,t=0)}} - 1, \tag{5.1}$$

where $A(\nu,t)$ the area of an endocardial patch ν at time t of the cardiac cycle; time $t = 0$ corresponds to end diastole. The patch ν is defined on the end-diastolic mesh - it is tracked as a "material point" through the subsequent time frames. The average patch size for a normal human LV was 2.6 ± 0.5 mm^2 yielding a high-resolution LV map of regional endocardial shortening.

The high resolution endocardial surface map of $\mathrm{RS_{CT}}$was divided into 72 endocardial segments: 18 in the circumferential direction (1 segment for every 20°) for each of 4 slices from apex to base along the LV long axis [22]; all $\mathrm{RS_{CT}}$values within each segment were averaged to yield a single $\mathrm{RS_{CT}}$value for that segment. This 72-segment model yields a higher spatial sampling of endocardial regional shortening than the traditional AHA 16-segment model [29]; the higher sampling is in agreement with the superior resolution of LV features visible on the 4DCT images [30, 31]. Each segment corresponds to approximately 2 cm^2 of endocardial surface for a normal sized LV. Two 72 segment models were constructed for each subject in this study: 1) derived from the original uncorrected CT images and 2) derived from the ResyncCT images.

5.2.4 Measuring the Mechanical Activation Time: Time to Onset of Shortening (TOS)

The TOS was estimated for all 72 segments of the LV for both the uncorrected and the ResyncCT images. The TOS for a particular segment was calculated as the time at which the $\mathrm{RS_{CT}}$vs time curve for that segment shortened by 10% of its full dynamic range during systolic contraction. We previously investigated estimating mechanical activation times of LV wall motion with 4DCT using controlled phantom experiments [21]. The main results of that

study highlighted that the estimates of activation times are more accurate and precise when measured during the constant motion profile of the LV during systolic contraction, vs. the time of the "pre-stretch peak" which was previously used as the mechanical activation time in tagged MR studies of dyssynchrony [32, 33]. Figure 5.2 illustrates the estimation of the TOS for an example RS_{CT}vs time curve from one LV segment.

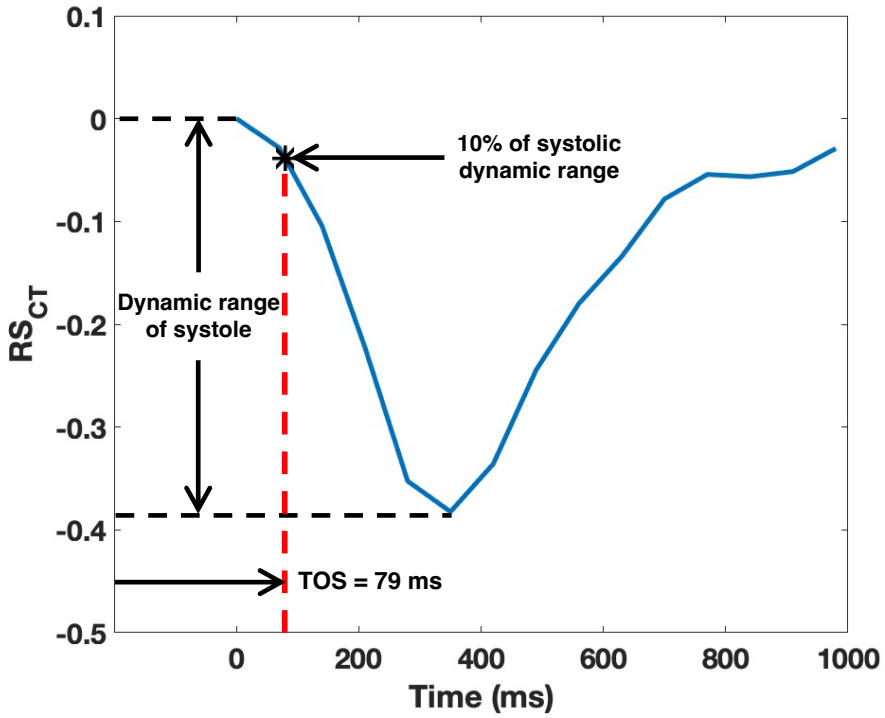

Figure 5.2: Estimation of the time to onset of shortening (TOS) for an example RS_{CT}vs time curve. The TOS has been shown to be the most accurate metric for estimating mechanical activation time. RS_{CT}: endocardial regional shortening.

5.2.5 Significance of Time to Onset of Shortening in Predicting CRT Response

The TOS has previously been shown to be an excellent metric to quantify LV dyssynchrony [7, 8, 34] and is also strongly correlated with CRT response [9–11]. From our previous

Table 5.1: Subject characteristics

N	24	
Age (years)	79 ± 9	
Female, n (%)	10 (42)	
Heartrate (bpm)	67 ± 13	
4DCT-derived EF (%)	Uncorrected	69.8 ± 8
	ResyncCT	69.5 ± 8
4DCT-derived volumes (mL)	EDV	147 ± 57
	ESV	48 ± 32
DLP (mGy · cm)	509 ± 252	

study, it was determined that a shift in TOS ($|\Delta TOS|$) of 35 ms will cause a significant shift in the classification of patients between low, mid, and high probability of CRT response [16]. In this study, the effect of ResyncCT was evaluated by observing the number of LV segments (as % LV surface area) that experienced a change in TOS estimates by greater than |35| ms between the uncorrected and the ResyncCT images for each subject.

5.3 Results

5.3.1 Subject Characteristics

Out of the 25 subjects used in this study, one had to be excluded due to significant calcification around the mitral valve, preventing the precise definition of the mitral valve plane. Ten of the 24 subjects were female (42%), and the average age of the entire cohort was 79 ± 9 years (median: 77 years; interquartile range: 14 years). The mean CT-derived LVEF was 69.8 ± 8% and 69.5 ± 8% for the uncorrected and the ResyncCT images, respectively ($p = 0.88$). Table 5.1 lists the subject characteristics.

5.3.2 False Dyssynchrony

Figure 5.3 highlights the pronounced effect of motion correction with ResyncCT on the position of the LV walls across the cardiac cycle. Figure 5.3A shows axial slices of the ResyncCT-derived images in an example subject for five consecutive time frames of the cardiac cycle. Figures 5.3B and 5.3C show difference images between the consecutive time frames of the uncorrected and the ResyncCT images, respectively. In the uncorrected images, for a particular time frame, walls moving perpendicular to the x-ray beam direction at the time of sampling are updated while the walls moving in a direction parallel to the x-rays are not updated; therefore, pairs of walls are updated only every other time frame in a series of 4DCT images reconstructed at 90°intervals of gantry rotation (70 ms for a gantry rotation time of 280 ms). Figure 5.3C highlights the continuous motion field recovered uniformly over all regions of the LV by ResyncCT.

5.3.3 Effect of ResyncCT on Accuracy of Mechanical Activation Time: Estimates of Time to Onset of Shortening

Figures 5.4A-5.4B show two example subjects and the effect of ResyncCT on their TOS estimates. For each subject, the first row shows the high-resolution bullseye maps of TOS, the second row shows mid-LV short-axis slices for three time frames of the cardiac cycle, and the third row shows difference images of the short-axis slices between the first three time frames. The figures on the left are derived from the uncorrected images and the figures on the right are derived from the ResyncCT images. Figure 5.4A shows a subject whose uncorrected images-derived TOS map has higher values on the anteroseptal wall as compared to those obtained from the ResyncCT images. Due to gantry-induced artifacts, the motion field between time frames t3 and t2 is lost in the uncorrected images as seen in the difference image on the bottom left; however, ResyncCT

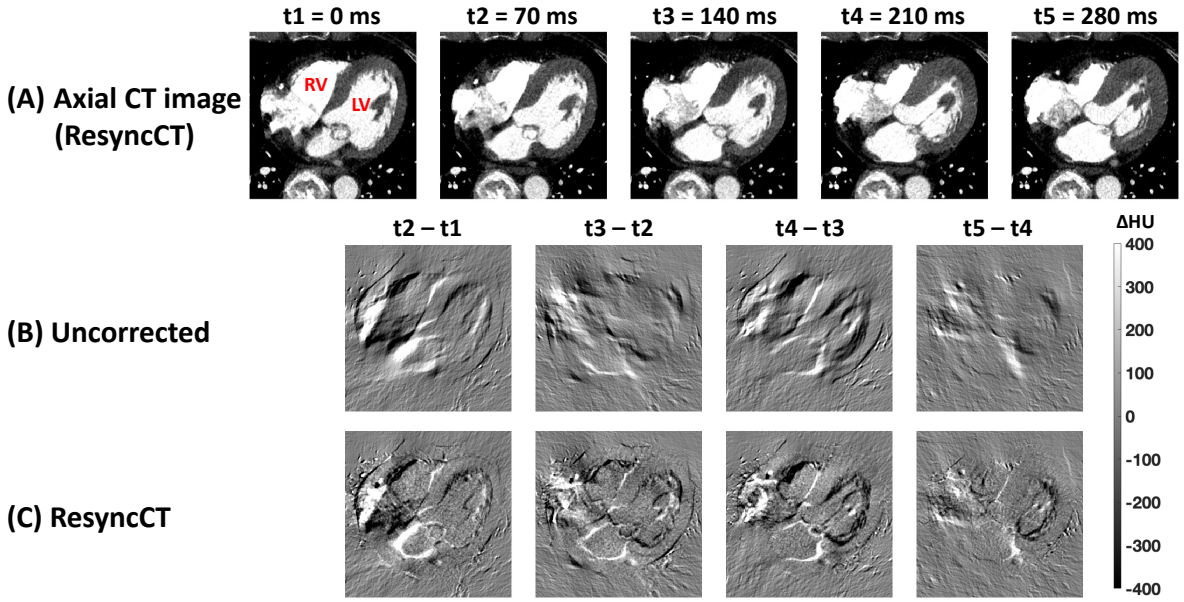

Figure 5.3: False dyssynchrony and recovery of motion field with ResyncCT in an example subject. (A) Axial slices of the ResyncCT-derived images in an example subject for five consecutive time frames across the cardiac cycle. (B-C) Difference images between the consecutive time frames of (B) the uncorrected images (not shown) and (C) the ResyncCT images shown in (A). Pairs of myocardial walls are updated every other time frame in the uncorrected images whereas ResyncCT recovers a continuous motion over all LV regions at each time frame. Note the clarity of the edges, and position of the right coronary artery in the ResyncCT processed images. LV: left ventricle; RV: right ventricle.

recovers this motion field. Figure 5.4B shows a subject with higher TOS values derived from the uncorrected images on the inferolateral wall; again, as seen in the difference image between time frames t3 and t2 of the uncorrected images on the bottom left, the inferolateral wall of the LV is not well localized due to gantry-induced artifacts.

Only one subject had no part of their endocardial surface differ in TOS estimates $\geq |35|$ ms; thus, in 23/24 (96%) subjects, ResyncCT had a significant impact on the TOS map and could potentially reclassify these subjects based on their probability of responding to CRT. Figure 5.5A shows bullseye maps of the difference in TOS estimates between the uncorrected and the ResyncCT images over all 72 endocardial segments for all 24 subjects; virtually all of the patients have substantial changes to the TOS values. Figure 5.5A also highlights the heterogenous subject-

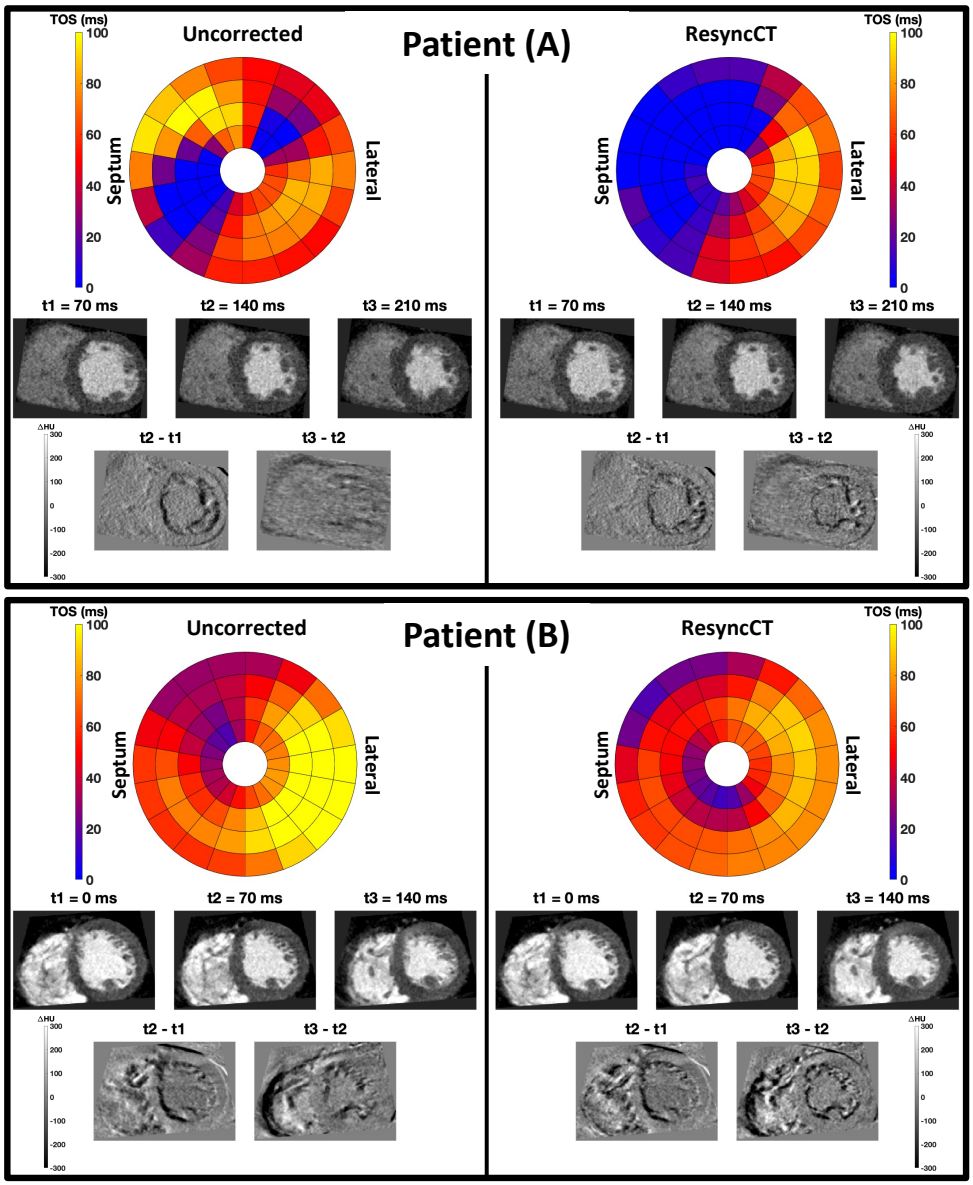

Figure 5.4: Subject specific effects of ResyncCT on the estimation of TOS in two example subjects (A) and (B). The left column gives results from uncorrected images, and the right column are results in the same subject using ResyncCT corrected images. In each column, the first row shows bullseye maps of TOS, the second row shows mid-LV short-axis slices for three time frames of the cardiac cycle, and the last row shows difference images between the first three time frames of the mid-LV short-axis images. TOS: time to onset of shortening. The bullseye plot views the LV from the apex to base.

specific differences in the TOS estimates between the uncorrected and the ResyncCT images; the degree of motion correction achieved depends on the direction of motion of the endocardial walls

with respect to the position of the gantry. Figure 5.5B shows the distribution of the percentage of the LV endocardial surface that differed in TOS estimates $\geq |35|$ ms between the uncorrected and the ResyncCT images. Sixteen subjects (67%) had 7 or more endocardial segments differ in TOS estimates $\geq |35|$ ms; the 7 segment threshold approximately corresponds to one of the standard AHA 16 segments [29], or 10% of the LV endocardial surface (14 cm^2).

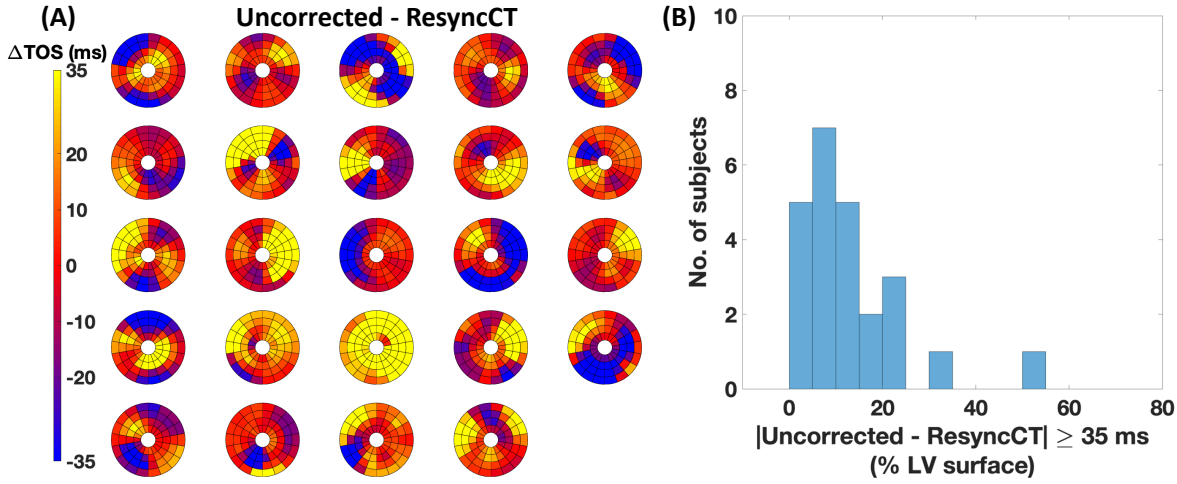

Figure 5.5: Effect of ResyncCT on TOS estimates over the LV. (A) Bullseye maps of the difference in TOS estimates across the entire LV between the uncorrected and the ResyncCT images for all 24 subjects. (B) Histogram showing the number of subjects vs the percentage of LV endocardial surface that differs in TOS estimates $\geq |35|$ ms between the uncorrected and the ResyncCT images. LV: left ventricle; TOS: time to onset of shortening.

5.4 Discussion

In this study, we evaluated the ability of a newly developed cardiac CT motion correction algorithm called ResyncCT to remove heart wall motion artifacts on routinely acquired clinical 4DCT images. The main findings of this study reveal the clinical utility of ResyncCT in minimizing gantry-induced false dyssynchrony artifacts in cardiac 4DCT images; this is especially important when estimating the mechanical activation time of the myocardium as 'times to onset

of shortening' from cardiac 4DCT images of subjects under consideration for CRT. In 23/24 subjects in this study, ResyncCT could have a significant effect in potentially reclassifying the subjects based on their probability of responding to CRT [16]. The TOS is the most prominent feature in determining the probability of CRT response; a change in TOS of greater than 35 ms could significantly change the estimated probability of a subject responding to CRT; thus, the accurate and precise estimation of TOS from 4DCT is essential.

We have previously evaluated the effect of ResyncCT under controlled phantom experiments [21], the results from which highlight the excellent accuracy and precision of ResyncCT-derived TOS estimates of LV wall motion. The work reported here expands that validation of ResyncCT to clinically acquired human 4DCT studies. Another important finding in our previous phantom studies was that the accuracy and precision of the TOS estimates were higher when measured on the constant motion profile of LV wall motion during systole vs. measuring the peak of pre-stretch; previous studies with tagged MRI used the peak of the strain curves to characterize mechanical activation delays [7, 33]. For this reason, the TOS in our study was defined as the time of the cardiac cycle where the RS_{CT}vs time curve reached 10% of its dynamic range during systolic contraction.

This study also highlights the heterogenous effect of "gantry artifact" on the TOS estimates of the 24 subjects; LV orientation, heart rate, LV systolic motion profile (velocity and acceleration), and gantry position with respect to LV wall motion during systole are some of the factors that make the corrections of ResyncCT subject specific. It is impossible to predict the interaction of a patient's heartrate with the gantry orientation, so ResyncCT is needed in case there are profound motion artifacts.

The TOS estimates are derived from RS_{CT}vs time data which has previously been shown

to have very low inter- and intra-observer variability The analysis pipeline used in this study to estimate high-resolution maps of TOS over the entire LV was fully automated, except for the definition of the mitral valve and LVOT planes. The inter- and intra-observer variability of the segmentation procedure, and in turn the variability of the RS_{CT}estimates has previously been shown to be very low [22], making the estimation of TOS from RS_{CT}vs time data to be highly reproducible. Additionally, with advances in deep learning cardiac image segmentation [35, 36], we expect the LV blood pool segmentation to be fully automated in the near future. This will ensure that results are exceptionally reproducible.

While dual-source CT scanners yield images with higher temporal resolution, their limited z-axis coverage of the detectors (4 cm) poses difficulties for full-heart volume imaging of patients with irregular heartbeats and/or arrythmias. The patients must be scanned in helical or "step and shoot" mode over multiple beats which may then yield step-artifacts, often rendering the images unanalyzable for the estimation of timing of mechanical events of the LV. Wider detector scanners (256- or 320-detector rows) with effective motion estimation and motion compensation technologies may be better suited for this application.

5.4.1 Limitations

This study was successful in highlighting the need for subject-specific application of ResyncCT on the estimates of TOS in a cohort of 24 subjects. While the results reveal that ResyncCT can potentially reclassify 96% of the subjects based on their probability of responding to CRT, the study lacks a ground-truth value of TOS to validate the accuracy of these estimates. However, our previous study validating the accuracy and precision of the ResyncCT-derived TOS estimates [16] with ground-truth phantom experiments provides evidence supporting the validity

of the estimates reported in this clinical cohort. The clinical utility of the results reported in this study, together with our previous validation using phantom experiments, motivate future studies to perform a direct comparison of the ResyncCT-derived TOS estimates with either cine CMR or CMR tagging.

All 24 subjects were scanned using the same CT scanner under the same clinical imaging protocol established at the center. The imaging protocol did not include any tube-current modulation across the cardiac cycle. While this was beneficial in estimating TOS values that weren't subject to image quality differences across the cardiac cycle, future studies should investigate the effect of tube-current modulation and ultra-low-dose scan protocols on the computed TOS values.

5.5 Conclusions

A novel cardiac CT motion correction algorithm called ResyncCT was shown to dramatically reduce motion artifacts on the endocardial wall in clinically acquired 4DCT studies. Mechanical activation times evaluated by the time to onset of regional shortening, a parameter shown to be a strong predictor of CRT response, were significantly changed after motion correction with ResyncCT.

Acknowledgements

Research reported in this publication was supported by NHLBI of the National Institutes of Health under award number R01 HL144678. The content is solely the responsibility of the authors and does not necessarily represent the official views of the National Institutes of Health.

This work was done during the term of an Award from the American Heart Association (AHA 20PRE35210261).

Chapter 5 is a reprint of the material: **Ashish Manohar**, James Yang, Jed D. Pack, and Elliot R. McVeigh. "Estimation of left ventricular mechanical activation times from motion-corrected cardiac 4DCT images" *bioRxiv*, DOI:10.1101/2022.04.12.488106, 2022. The dissertation author is the primary author.

5.6 References

1. Prinzen, F. W., Vernooy, K. & Auricchio, A. Cardiac Resynchronization Therapy. *Circulation* **128,** 2407–2418. ISSN: 0009-7322. https://www.ahajournals.org/doi/10.1161/CIRCULATIONAHA.112.000112 (Nov. 2013).

2. Vernooy, K., van Deursen, C. J. M., Strik, M. & Prinzen, F. W. Strategies to improve cardiac resynchronization therapy. *Nature Reviews Cardiology* **11,** 481–493. ISSN: 1759-5002. http://www.nature.com/articles/nrcardio.2014.67 (Aug. 2014).

3. Daubert, J.-C., Saxon, L., Adamson, P. B., Auricchio, A., Berger, R. D., Beshai, J. F., Breithard, O., Brignole, M., Cleland, J., DeLurgio, D. B., Dickstein, K., Exner, D. V., Gold, M., Grimm, R. A., Hayes, D. L., Israel, C., Leclercq, C., Linde, C., Lindenfeld, J., Merkely, B., Mont, L., Murgatroyd, F., Prinzen, F., Saba, S. F., Shinbane, J. S., Singh, J., Tang, A. S., Vardas, P. E., Wilkoff, B. L., Zamorano, J. L., Anand, I., Blomstrom-Lundqvist, C., Boehmer, J. P., Calkins, H., Cazeau, S., Delgado, V., Estes, N. A. M., Haines, D., Kusumoto, F., Leyva, P., Ruschitzka, F., Stevenson, L. W. & Torp-Pedersen, C. T. 2012 EHRA/HRS expert consensus statement on cardiac resynchronization therapy in heart failure: implant and follow-up recommendations and management: A registered branch of the European Society of Cardiology (ESC), and the Heart Rhythm Society; and in col. *Europace* **14,** 1236–1286. ISSN: 1099-5129. https://academic.oup.com/europace/article-lookup/doi/10.1093/europace/eus222 (Sept. 2012).

4. Delgado, V. & Bax, J. J. Assessment of Systolic Dyssynchrony for Cardiac Resynchronization Therapy Is Clinically Useful. *Circulation* **123,** 640–655. ISSN: 0009-7322. https://www.ahajournals.org/doi/10.1161/CIRCULATIONAHA.110.954404 (Feb. 2011).

5. Sung, R. K. & Foster, E. Assessment of Systolic Dyssynchrony for Cardiac Resynchronization Therapy Is Not Clinically Useful. *Circulation* **123,** 656–662. ISSN: 0009-7322. https://www.ahajournals.org/doi/10.1161/CIRCULATIONAHA.110.954420 (Feb. 2011).

6. McVeigh, E. R. & Zerhouni, E. A. Noninvasive measurement of transmural gradients in myocardial strain with MR imaging. *Radiology* **180,** 677–683. ISSN: 0033-8419. http://pubs.rsna.org/doi/10.1148/radiology.180.3.1871278 (Sept. 1991).

7. Wyman, B. T., Hunter, W. C., Prinzen, F. W. & McVeigh, E. R. Mapping propagation of mechanical activation in the paced heart with MRI tagging. *American Journal of Physiology-Heart and Circulatory Physiology* **276,** H881–H891. ISSN: 0363-6135. https://www.physiology.org/doi/10.1152/ajpheart.1999.276.3.H881 (Mar. 1999).

8. Wyman, B. T., Hunter, W. C., Prinzen, F. W., Faris, O. P. & McVeigh, E. R. Effects of single- and biventricular pacing on temporal and spatial dynamics of ventricular contraction. *American Journal of Physiology-Heart and Circulatory Physiology* **282,** H372–H379. ISSN: 0363-6135. https://www.physiology.org/doi/10.1152/ajpheart.2002.282.1.H372 (Jan. 2002).

9. Auger, D. A., Bilchick, K. C., Gonzalez, J. A., Cui, S. X., Holmes, J. W., Kramer, C. M., Salerno, M. & Epstein, F. H. Imaging left-ventricular mechanical activation in heart failure patients using cine DENSE MRI: Validation and implications for cardiac resynchronization therapy. *Journal of Magnetic Resonance Imaging* **46,** 887–896. ISSN: 10531807. http://doi.wiley.com/10.1002/jmri.25613%20https://onlinelibrary.wiley.com/doi/10.1002/jmri.25613 (Sept. 2017).

10. Bilchick, K. C., Kuruvilla, S., Hamirani, Y. S., Ramachandran, R., Clarke, S. A., Parker, K. M., Stukenborg, G. J., Mason, P., Ferguson, J. D., Moorman, J. R., Malhotra, R., Mangrum, J. M., Darby, A. E., DiMarco, J., Holmes, J. W., Salerno, M., Kramer, C. M. & Epstein, F. H. Impact of Mechanical Activation, Scar, and Electrical Timing on Cardiac Resynchronization Therapy Response and Clinical Outcomes. *Journal of the American College of Cardiology* **63,** 1657–1666. ISSN: 07351097. https://linkinghub.elsevier.com/retrieve/pii/S073510971401170X (Apr. 2014).

11. Taylor, R. J., Umar, F., Panting, J. R., Stegemann, B. & Leyva, F. Left ventricular lead position, mechanical activation, and myocardial scar in relation to left ventricular reverse remodeling and clinical outcomes after cardiac resynchronization therapy: A feature-tracking and contrast-enhanced cardiovascular magnetic r. *Heart Rhythm* **13,** 481–489. ISSN: 15475271. https://linkinghub.elsevier.com/retrieve/pii/S1547527115013053 (Feb. 2016).

12. Chen, M. Y., Shanbhag, S. M. & Arai, A. E. Submillisievert Median Radiation Dose for Coronary Angiography with a Second-Generation 320–Detector Row CT Scanner in 107 Consecutive Patients. *Radiology* **267,** 76–85. ISSN: 0033-8419. http://pubs.rsna.org/doi/10.1148/radiol.13122621 (Apr. 2013).

13. Gould, J., Sidhu, B. S., Sieniewicz, B. J., Porter, B., Lee, A. W. C., Razeghi, O., Behar, J. M., Mehta, V., Elliott, M. K., Toth, D., Haberland, U., Razavi, R., Rajani, R., Niederer, S. & Rinaldi, C. A. Feasibility of intraprocedural integration of cardiac CT to guide left ventricular lead implantation for CRT upgrades. *Journal of Cardiovascular Electrophysiology* **32,**

802–812. ISSN: 1045-3873. https://onlinelibrary.wiley.com/doi/10.1111/jce.14896 (Mar. 2021).

14. Truong, Q. A., Szymonifka, J., Picard, M. H., Thai, W.-e., Wai, B., Cheung, J. W., Heist, E. K., Hoffmann, U. & Singh, J. P. Utility of dual-source computed tomography in cardiac resynchronization therapy—DIRECT study. *Heart Rhythm* **15,** 1206–1213. ISSN: 15475271. https://doi.org/10.1016/j.hrthm.2018.03.020%20https://linkinghub.elsevier.com/retrieve/pii/S1547527118302340 (Aug. 2018).

15. Fyenbo, D. B., Sommer, A., Kühl, J. T., Kofoed, K. F., Nørgaard, B. L., Kronborg, M. B., Bouchelouche, K. & Nielsen, J. C. Transmural Myocardial Scar Assessed by Cardiac Computed Tomography. *Journal of Computer Assisted Tomography* **43,** 312–316. ISSN: 0363-8715. http://journals.lww.com/00004728-201903000-00024 (2019).

16. Manohar, A., Colvert, G. M., Yang, J., Chen, Z., Ledesma-Carbayo, M. J., Kronborg, M. B., Sommer, A., Nørgaard, B. L., Nielsen, J. C. & McVeigh, E. R. Prediction of CRT Response Using a Lead Placement Score Derived from 4DCT. *medRxiv,* 2022.03.23.22272846. http://medrxiv.org/content/early/2022/03/24/2022.03.23.22272846.abstract (Mar. 2022).

17. Kyme, A. Z. & Fulton, R. R. Motion estimation and correction in SPECT, PET and CT. *Physics in Medicine & Biology* **66,** 18TR02. ISSN: 0031-9155. https://iopscience.iop.org/article/10.1088/1361-6560/ac093b (Sept. 2021).

18. Kim, S., Chang, Y. & Ra, J. B. Cardiac motion correction based on partial angle reconstructed images in x-ray CT. *Medical Physics* **42,** 2560–2571. ISSN: 00942405. http://doi.wiley.com/10.1118/1.4918580 (Apr. 2015).

19. Kidoh, M., Shen, Z., Suzuki, Y., Ciuffo, L., Ashikaga, H., Fung, G. S. K., Otake, Y., Zimmerman, S. L., Lima, J. A. C., Higuchi, T., Lee, O., Sato, Y., Becker, L. C., Fishman, E. K. & Taguchi, K. *False dyssynchrony: problem with image-based cardiac functional analysis using x-ray computed tomography* in *Medical Imaging 2017: Physics of Medical Imaging* (eds Flohr, T. G., Lo, J. Y. & Gilat Schmidt, T.) (Mar. 2017), 101321U. ISBN: 9781510607095. http://proceedings.spiedigitallibrary.org/proceeding.aspx?doi=10.1117/12.2250257.

20. Contijoch, F., Stayman, J. W. & McVeigh, E. R. The impact of small motion on the visualization of coronary vessels and lesions in cardiac CT: A simulation study. *Medical Physics* **44,** 3512–3524. ISSN: 00942405. http://doi.wiley.com/10.1002/mp.12295 (July 2017).

21. Manohar, A., Pack, J. D., Schluchter, A. J. & McVeigh, E. R. Four-dimensional computed tomography of the left ventricle, Part II: Estimation of mechanical activation times. *Medical Physics.* ISSN: 0094-2405. https://onlinelibrary.wiley.com/doi/10.1002/mp.15550 (Mar. 2022).

22. Colvert, G. M., Manohar, A., Contijoch, F. J., Yang, J., Glynn, J., Blanke, P., Leipsic, J. A. & McVeigh, E. R. Novel 4DCT Method to Measure Regional Left Ventricular Endocardial

Shortening Before and After Transcatheter Mitral Valve Implantation. *Structural Heart* **5,** 410–419. ISSN: 2474-8706. https://doi.org/10.1080/24748706.2021.1934617%20https://www.tandfonline.com/doi/full/10.1080/24748706.2021.1934617 (July 2021).

23. Otsu, N. A Threshold Selection Method from Gray-Level Histograms. *IEEE Transactions on Systems, Man, and Cybernetics* **9,** 62–66. ISSN: 0018-9472. http://ieeexplore.ieee.org/document/4310076/ (Jan. 1979).

24. Yushkevich, P. A., Piven, J., Hazlett, H. C., Smith, R. G., Ho, S., Gee, J. C. & Gerig, G. User-guided 3D active contour segmentation of anatomical structures: Significantly improved efficiency and reliability. *NeuroImage* **31,** 1116–1128. ISSN: 10538119. https://linkinghub.elsevier.com/retrieve/pii/S1053811906000632 (July 2006).

25. McVeigh, E. R., Pourmorteza, A., Guttman, M., Sandfort, V., Contijoch, F., Budhiraja, S., Chen, Z., Bluemke, D. A. & Chen, M. Y. Regional myocardial strain measurements from 4DCT in patients with normal LV function. *Journal of Cardiovascular Computed Tomography* **12,** 372–378. ISSN: 19345925. https://doi.org/10.1016/j.jcct.2018.05.002%20https://linkinghub.elsevier.com/retrieve/pii/S1934592518300923 (Sept. 2018).

26. Contijoch, F. J., Groves, D. W., Chen, Z., Chen, M. Y. & McVeigh, E. R. A novel method for evaluating regional RV function in the adult congenital heart with low-dose CT and SQUEEZ processing. *International Journal of Cardiology* **249,** 461–466. ISSN: 01675273. https://doi.org/10.1016/j.ijcard.2017.08.040%20https://linkinghub.elsevier.com/retrieve/pii/S0167527317334460 (Dec. 2017).

27. Manohar, A., Colvert, G. M., Schluchter, A., Contijoch, F. & McVeigh, E. R. Anthropomorphic left ventricular mesh phantom: a framework to investigate the accuracy of SQUEEZ using Coherent Point Drift for the detection of regional wall motion abnormalities. *Journal of Medical Imaging* **6,** 1. ISSN: 2329-4302. https://www.spiedigitallibrary.org/journals/journal-of-medical-imaging/volume-6/issue-04/045001/Anthropomorphic-left-ventricular-mesh-phantom--a-framework-to-investigate/10.1117/1.JMI.6.4.045001.full (Dec. 2019).

28. Myronenko, A. & Xubo Song. Point Set Registration: Coherent Point Drift. *IEEE Transactions on Pattern Analysis and Machine Intelligence* **32,** 2262–2275. ISSN: 0162-8828. arXiv: 0905.2635. http://arxiv.org/abs/0905.2635%7B%5C%%7D0Ahttp://dx.doi.org/10.1109/TPAMI.2010.46%20http://www.ncbi.nlm.nih.gov/pubmed/20975122%20http://ieeexplore.ieee.org/document/5432191/ (Dec. 2010).

29. Cerqueira, M. D., Weissman, N. J., Dilsizian, V., Jacobs, A. K., Kaul, S., Laskey, W. K., Pennell, D. J., Rumberger, J. A., Ryan, T. & Verani, M. S. Standardized Myocardial Segmentation and Nomenclature for Tomographic Imaging of the Heart. *Circulation* **105,** 539–542. ISSN: 0009-7322. https://www.ahajournals.org/doi/10.1161/hc0402.102975 (Jan. 2002).

30. Cruz-Bastida, J. P., Gomez-Cardona, D., Li, K., Sun, H., Hsieh, J., Szczykutowicz, T. P. & Chen, G.-H. Hi-Res scan mode in clinical MDCT systems: Experimental assessment of spatial resolution performance. *Medical Physics* **43,** 2399–2409. ISSN: 00942405. http://doi.wiley.com/10.1118/1.4946816 (Apr. 2016).

31. Manohar, A., Rossini, L., Colvert, G., Vigneault, D. M., Contijoch, F., Chen, M. Y., del Alamo, J. C. & McVeigh, E. R. Regional dynamics of fractal dimension of the left ventricular endocardium from cine computed tomography images. *Journal of Medical Imaging* **6,** 1. ISSN: 2329-4302. https://www.spiedigitallibrary.org/journals/journal-of-medical-imaging/volume-6/issue-04/046002/Regional-dynamics-of-fractal-dimension-of-the-left-ventricular-endocardium/10.1117/1.JMI.6.4.046002.full (Nov. 2019).

32. Prinzen, F. W., Hunter, W. C., Wyman, B. T. & McVeigh, E. R. Mapping of regional myocardial strain and work during ventricular pacing: experimental study using magnetic resonance imaging tagging. eng. *Journal of the American College of Cardiology* **33,** 1735–1742. ISSN: 07351097. https://linkinghub.elsevier.com/retrieve/pii/S0735109799000686 (May 1999).

33. Faris, O. P., Evans, F. J., Ennis, D. B., Helm, P. A., Taylor, J. L., Chesnick, A. S., Guttman, M. A., Ozturk, C. & McVeigh, E. R. Novel Technique for Cardiac Electromechanical Mapping with Magnetic Resonance Imaging Tagging and an Epicardial Electrode Sock. *Annals of Biomedical Engineering* **31,** 430–440. ISSN: 0090-6964. http://link.springer.com/10.1114/1.1560618 (Apr. 2003).

34. McVeigh, E. R., Prinzen, F. W., Wyman, B. T., Tsitlik, J. E., Halperin, H. R. & Hunter, W. C. Imaging asynchronous mechanical activation of the paced heart with tagged MRI. *Magnetic Resonance in Medicine* **39,** 507–513. ISSN: 07403194. http://doi.wiley.com/10.1002/mrm.1910390402 (Apr. 1998).

35. Chen, C., Qin, C., Qiu, H., Tarroni, G., Duan, J., Bai, W. & Rueckert, D. Deep Learning for Cardiac Image Segmentation: A Review. *Frontiers in Cardiovascular Medicine* **7.** ISSN: 2297-055X. arXiv: 1911.03723. https://www.frontiersin.org/article/10.3389/fcvm.2020.00025/full (Mar. 2020).

36. Vigneault, D. M., Contijoch, F., Bridge, C. P., Lowe, K., Jan, C. & McVeigh, E. R. *M-SiSSR: Regional Endocardial Function Using Multilabel Simultaneous Subdivision Surface Registration* in *Functional Imaging and Modeling of the Heart* (Springer, Cham, 2021), 242–252. https://link.springer.com/10.1007/978-3-030-78710-3%7B%5C_%7D24.

Chapter 6

Conclusions and future work

Advances in 4DCT technology have permitted the acquisition of ultra low dose high resolution full volume cardiac images spanning the entire cardiac cycle within a single heartbeat and from a single table position; no other clinical imaging modality comes close to this capability for cardiac imaging. Despite multiple studies highlighting the importance of regional cardiac function assessment for the better planning and management of disease [1–5], there remains an unmet clinical need for an easy-to-use, easily available, accurate, and reproducible method for assessing regional cardiac function [6]. This dissertation focused on understanding, improving, and demonstrating the ability of 4DCT to yield high spatio-temporal resolution estimates of regional cardiac function from a very simple and reproducible scanning procedure; this is a significant advantage over echocardiography and CMR, especially as these reproducible estimates are now obtained from ultra-low dose images. This dissertation has established a foundation for future work to implement the developed methods in larger independent clinical cohorts and randomized controlled trials to fully investigate the potential benefit of 4DCT in the management of cardiac disease.

6.1 Conlusions of our studies

In the second chapter of this dissertation "*Spatial resolution of regional cardiac function assessment with 4DCT*", we developed an anthropomorphically accurate LV phantom with programmed regional wall motion abnormalities of varying sizes and severities. The phantom was used to obtain guidance on the smallest size of wall motion abnormalities that can be accurately estimated with 4DCT. The results reported in this chapter highlighted that 4DCT can accurately detect (to within ±5% error) endocardial regions of dysfunction greater than 19 mm in diameter, with the threshold for detection lying between 14 and 19 mm.

The third chapter "*Temporal resolution of estimating timing of LV mechanics with 4DCT*" broadens our understanding of the temporal resolution of 4DCT, with a special focus on the 'false dyssynchrony' artifact. This artifact has not been investigated in depth previously, and impedes the accurate and reproducible estimation of the timing of LV mechanics with 4DCT. Using an anthropomorphically accurate dyssynchronous LV phantom that served as ground-truth, we demonstrated that 4DCT images processed with the ResyncCT motion correction algorithm yields estimates of the timing of LV mechanics with significantly improved accuracy and precision. This work was foundational in highlighting the potential utility of 4DCT in estimating the timing of mechanical events of interest of the LV for CRT guidance.

The fourth chapter "*Prediction of CRT response using a lead placement score defined using 4DCT-derived features of LV mechanics*" utilizes the methods developed in chapters 2 and 3 on a clinical cohort of 82 subjects who underwent CRT. These subjects had 4DCT scans acquired pre- and post-CRT implantation; thus, permitting very precise measurements of regional changes in LV function. A model called the *lead placement score* to predict CRT response was developed using features of LV mechanics derived from the pre-CRT scans of the subjects. The

lead placement score model was effective in reclassifying 25% of the subjects into low-probability of response, 25% into high probability of response, and the remaining 50% with a probability of response that was unchanged from the pretest probability. The promising results reported in this work highlight the potential utility of 4DCT in the optimal planning and management of patients under consideration for CRT.

In the fifth chapter of this dissertation "*Clinical utility of motion-corrected cardiac 4DCT images in the estimation of left ventricular mechanical activation times*", we investigated the effect of the newly developed cardiac motion correction algorithm called ResyncCT on the estimation of LV mechanical activation times in a cohort of 24 subjects with routinely acquired clinical cardiac 4DCT images. ResyncCT had a pronounced effect on the timing estimates of LV mechanics; 96% of the subjects used in the study could potentially be reclassified based on their estimated probabilities of responding to CRT. Additionally, the differences in the timing estimates between the ResyncCT and motion uncorrected images were heterogeneous and subject-specific. The work reported in this chapter highlights the potential clinical utility of motion corrected 4DCT images in estimating timing of mechanical events of interest in the LV with 4DCT.

6.2 Potential future work

A major concern with the increased use of 4DCT for disease planning and management is the increase in exposure to ionizing radiation on a societal level. Significant efforts have been focused on improving 4DCT imaging technologies that enable the acquisition of full 3D volumes of the heart across the cardiac cycle with as little radiation dose as possible; current full 3D images of the heart for a full R-R cycle are routinely obtained with < 3 mSv dose [7, 8].

However, low dose implies low image quality. The accuracy and precision of the regional cardiac function estimates derived from the methods developed in this dissertation need to be thoroughly investigated in the context of low dose imaging. Using an accurate noise emulation tool, a series of low dose images could be simulated. The accuracy and precision limits of the regional strain estimates can then be determined as a function of lowering tube current. Additionally, guidance may then be obtained for the optimal tube current and voltage settings as a function of patient size for imaging with the lowest radiation dose possible, but with sufficient image quality for regional function assessment.

The *lead placement score* is a promising metric for predicting patient response to CRT. It was defined using only a few features of LV mechanics derived from the pre-CRT scans of the subjects. The 4DCT scans contain an *abundance* of information; just the RS_{CT}vs time data for a single subject has 90 segments with 20 time points in each segment. Hence, future work could explore using more advanced models to extract the dense functional information from the 4DCT datasets for predicting CRT response. Additionally, post-CRT 4DCT scans are available in the existing subject cohort of 82 subjects. Information derived from these scans could potentially be used to provide mechanistic explanations of the underlying processes behind LV remodeling and reverse remodeling; this could have significant implications in better understanding CRT response as a whole. Similar strategies could be used for other treatments as well such as TAVR and TMVI to not only predict LV response, but to also understand the mechanisms governing them.

The methods developed in this dissertation take advantage of the region of the cardiac 4DCT images with the highest contrast: the boundary between the LV endocardium and the blood pool. This significantly improves the reproducibility of the regional cardiac function es-

timates over other methods that utilize endo- and epicardial contours. However, as with any endocardium-based method, there are "blind-spots" at the papillary muscle insertion points. Deep learning networks could be developed to approximate the best 2D surface to "cover" the insertion points.

Lastly, this dissertation broadens our general understanding of the ability of 4DCT to derive high spatio-temporal resolution estimates of regional cardiac function and demonstrates its potential utility in clinical cohorts of subjects. Future work could apply the developed methods to larger independent cohorts followed by randomized controlled trials to fully investigate the efficacy of 4DCT in the planning and management of cardiac disease.

6.3 References

1. Amundsen, B. H., Helle-Valle, T., Edvardsen, T., Torp, H., Crosby, J., Lyseggen, E., Støylen, A., Ihlen, H., Lima, J. A., Smiseth, O. A. & Slørdahl, S. A. Noninvasive Myocardial Strain Measurement by Speckle Tracking Echocardiography. *Journal of the American College of Cardiology* **47,** 789–793. ISSN: 07351097. http://dx.doi.org/10.1016/j.jacc.2005.10.040%20https://linkinghub.elsevier.com/retrieve/pii/S0735109705027506 (Feb. 2006).

2. Moore, C., McVeigh, E. & Zerhouni, E. Noninvasive Measurement of Three-Dimensional Myocardial Deformation with Tagged Magnetic Resonance Imaging During Graded Local Ischemia. *Journal of Cardiovascular Magnetic Resonance* **1,** 207–222. ISSN: 1097-6647. arXiv: NIHMS150003. http://www.informaworld.com/openurl?genre=article%7B%5C&%7Ddoi=10.3109/10976649909088333%7B%5C&%7Dmagic=crossref%7B%5C%%7D7C%7B%5C%%7D7CD404A21C5BB053405B1A640AFFD44AE3 (July 1999).

3. Thavendiranathan, P., Poulin, F., Lim, K.-D., Plana, J. C., Woo, A. & Marwick, T. H. Use of Myocardial Strain Imaging by Echocardiography for the Early Detection of Cardiotoxicity in Patients During and After Cancer Chemotherapy. *Journal of the American College of Cardiology* **63,** 2751–2768. ISSN: 07351097. http://dx.doi.org/10.1016/j.jacc.2014.01.073%20https://linkinghub.elsevier.com/retrieve/pii/S073510971401660X (July 2014).

4. Prinzen, F. W., Hunter, W. C., Wyman, B. T. & McVeigh, E. R. Mapping of regional myocardial strain and work during ventricular pacing: experimental study using magnetic resonance imaging tagging. eng. *Journal of the American College of Cardiology* **33,** 1735–1742.

ISSN: 07351097. https://linkinghub.elsevier.com/retrieve/pii/S0735109799000686 (May 1999).

5. Leclercq, C., Faris, O., Tunin, R., Johnson, J., Kato, R., Evans, F., Spinelli, J., Halperin, H., McVeigh, E. & Kass, D. A. Systolic Improvement and Mechanical Resynchronization Does Not Require Electrical Synchrony in the Dilated Failing Heart With Left Bundle-Branch Block. *Circulation* **106,** 1760–1763. ISSN: 0009-7322. https://www.ahajournals.org/doi/10.1161/01.CIR.0000035037.11968.5C (Oct. 2002).

6. Abraham, T. & Nishimura, R. Myocardial strain: can we finally measure contractility?Editorials published in Journal of the American College of Cardiologyreflect the views of the authors and do not necessarily represent the views of JACCor the American College of Cardiology. *Journal of the American College of Cardiology* **37,** 731–734. ISSN: 07351097. http://dx.doi.org/10.1016/S0735-1097(00)01173-6%20https://linkinghub.elsevier.com/retrieve/pii/S0735109700011736 (Mar. 2001).

7. Chen, M. Y., Shanbhag, S. M. & Arai, A. E. Submillisievert Median Radiation Dose for Coronary Angiography with a Second-Generation 320–Detector Row CT Scanner in 107 Consecutive Patients. *Radiology* **267,** 76–85. ISSN: 0033-8419. http://pubs.rsna.org/doi/10.1148/radiol.13122621 (Apr. 2013).

8. Contijoch, F. J., Groves, D. W., Chen, Z., Chen, M. Y. & McVeigh, E. R. A novel method for evaluating regional RV function in the adult congenital heart with low-dose CT and SQUEEZ processing. *International Journal of Cardiology* **249,** 461–466. ISSN: 01675273. https://doi.org/10.1016/j.ijcard.2017.08.040%20https://linkinghub.elsevier.com/retrieve/pii/S0167527317334460 (Dec. 2017).

Appendix A

Spatial resolution of regional cardiac function assessment with 4DCT - Supplementary Information

A.1 Definition of dysfunctional patch as a 2D sigmoid surface

We defined our regions of dysfunction to be sigmoid in shape to simulate a smooth transition from the core of the dysfunctional region to the normal functioning endocardial tissue. The sigmoid function was defined as:

$$G(u,v) = \sqrt{\frac{a}{1+e^{-b\cdot u}}} \times \sqrt{\frac{a}{1+e^{-b\cdot v}}} \tag{A.1}$$

where a is the user defined % reduction in normal strain, b is the slope of the sigmoid function, and (u,v) are the planar coordinates defining a 71 x 71 grid from -3 to 4 in each direction; each

user defined dysfunctional patch was normalized to this (u, v) grid. For the work reported in this paper, we fixed $b = 1.25$ and a took on either 70% or 40% for simulating hypokinesia and subtle hypokinesia respectively.

To apply this smooth transition in strain, we parameterized the mesh points belonging to the dysfunctional patch in 3D space from $p(x, y, z)$ to surface coordinates $s(l, z)$. By doing so, each point in the dysfunctional patch was given an index location based on its distance l along the endocardial surface from the user-input center of the dysfunctional patch and also on its slice location z relative to that of the patch center. Figure A.1 shows three views of a user defined dysfunctional patch of the endocardium of radius 25 mm.

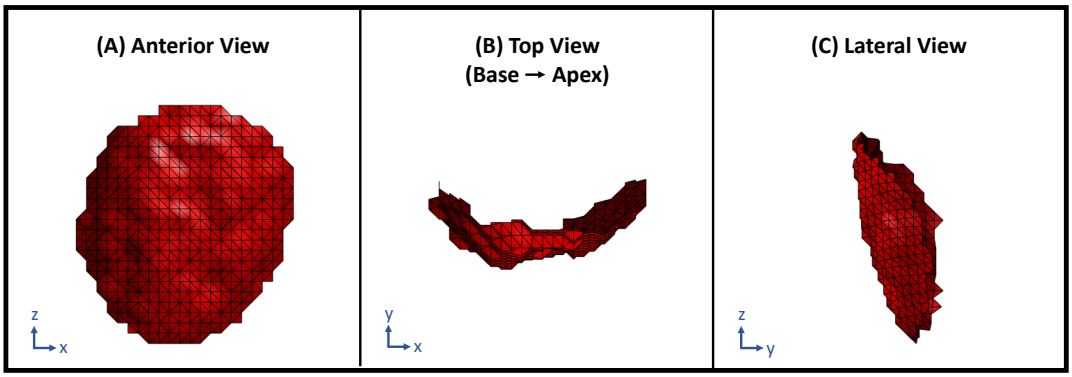

Figure A.1: User defined LV endocardial patch of radius 25 mm to simulate regional dysfunction. (A) Anterior view of the patch with the septum to the left and the lateral wall to the right. (B) Top view of the patch looking from the base down into the apex with the inferior wall at 12 o'clock, lateral wall at 3, anterior wall at 6, and the septum at 9. (C) Lateral view of the patch with the anterior wall to the left and the inferior wall to the right. LV:left ventricle

The parameterization was performed in a slice-by-slice fashion; the number of rows in the 2D sigmoid matched the number of z slices in the dysfunctional patch. In this manner, each point on the dysfunctional patch was assigned a corresponding strain reduction factor defined by the sigmoid function. Points on slices closer to that of the user-defined center received a higher strain reduction than points farther away in z. Similarly, points in a particular slice closer to

the user defined patch center along the surface in the circumferential direction received a higher strain reduction than points lying farther away. Figure A.2A shows a single slice of points on the dysfunctional patch with the user-input patch center shown in red and Fig. A.2B shows the 2D sigmoid function with a smooth transition from 70% reduction in strain at the center to ∼0% at the peripheral regions. The strain reduction factor assigned to each point in the dysfunctional patch was then multiplied with the ϵ_{zz} and the ϵ_{cc} components in Eq. 2.3 to create the desired region of dysfunction.

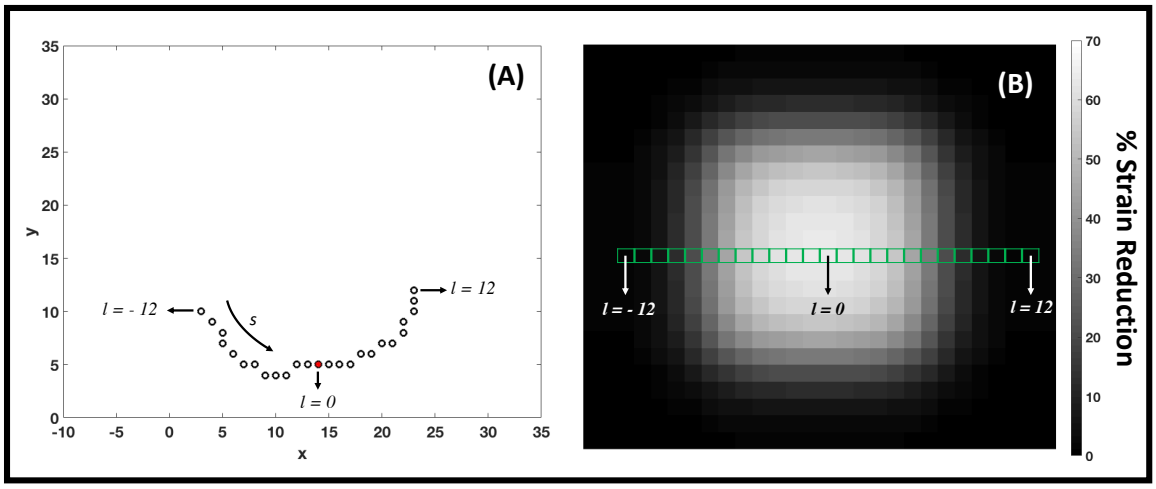

Figure A.2: Application of 2D sigmoid function to ensure smooth transition in strain between the core of the dysfunctional region and the normal functioning endocardium. (A) Top view of a single z slice of points looking from the base down towards the apex with the inferior wall at 12 o'clock, lateral wall at 3, anterior wall at 6, and the septum at 9. The black circles represent points on the endocardial surface belonging to the dysfunctional patch with the user-input patch center highlighted in red. (B) 2D sigmoid function showing a smooth transition in strain from a peak 70% reduction at the core to no strain reduction at the peripheral regions. Each z slice of the dysfunctional patch corresponds to a row of the sigmoid function. When measured along the endocardial surface, points within a slice closer to the user-defined patch center received a higher reduction in strain than points lying farther away.

A.2 Frequency response estimation of the applied low-pass mesh filter: Comparison with the 'Standard' reconstruction kernel of a clinical GE Revolution CT scanner

The low-pass filter, described in Sec. 2.2.3, was applied on the analytically displaced end systolic mesh points to simulate the natural endocardial texture change that occurs during systole. The texture change is a result of features collapsing during systole and the inability of the scanner to resolve these fine features due to its finite resolution (point-spread function). The filter required two user input parameters, the smoothing weight α and the number of iterations n. These values were chosen such that the modulation transfer function (MTF) of the filter was similar to that of the 'Standard' reconstruction kernel of a 256 detector-row clinical scanner (Revolution CT, General Electric Medical Systems, Wisconsin). The Revolution CT was chosen for comparison purposes for the following two reasons: 1) the MTF of the 'Standard' reconstruction kernel of this scanner has been measured previously [1] and 2) it was the scanner available to us at the time to perform our own independent measurement of the MTF.

The experimental measurement of the MTF of the scanner was performed in a manner similar to that outlined by Cruz-Bastida et al., 2016 [1]. A titanium bead of 0.25 mm in diameter was placed at the isocenter of the scanner and reconstructed (reconstruction diameter: 50 mm; kernel: Standard) at with pixel spacings of 0.097 mm in x and y, with a slice thickness of 0.625 mm in z. Eight images with independent noise were acquired (tube current: 270 mA; kVp: 120 kV; gantry revolution time: 280 ms) and the MTF was measured by computing the discrete Fourier transform of the point spread function, obtained by averaging the 8 independent images of the bead. The estimated MTF was in good agreement with that measured by Cruz-Bastida

et al., as seen in Fig. A.3.

The MTF of the low-pass filter, with the chosen values of $\alpha = 0.4$ and $n = 4$, was measured by creating 1000 images of 256 x 256 pixels of uniformly distributed white noise. A mesh was extracted with the defined 256 x 256 grid as the x and y coordinates and the connectivity matrix was obtained using the Delaunay triangulation algorithm. The intensity of the white noise at each pixel location was added as the z coordinate to the corresponding mesh point. The low-pass filter was independently applied to each of the 1000 meshes generated and the output of the filter in each case was converted back to an image by transferring the smoothed z values to pixel intensities at their corresponding locations on the image grid. The MTF was estimated by averaging the discrete Fourier transform of the 1000 filtered images. Figure A.3 shows the MTF of the filter overlaid with the MTF of the scanner.

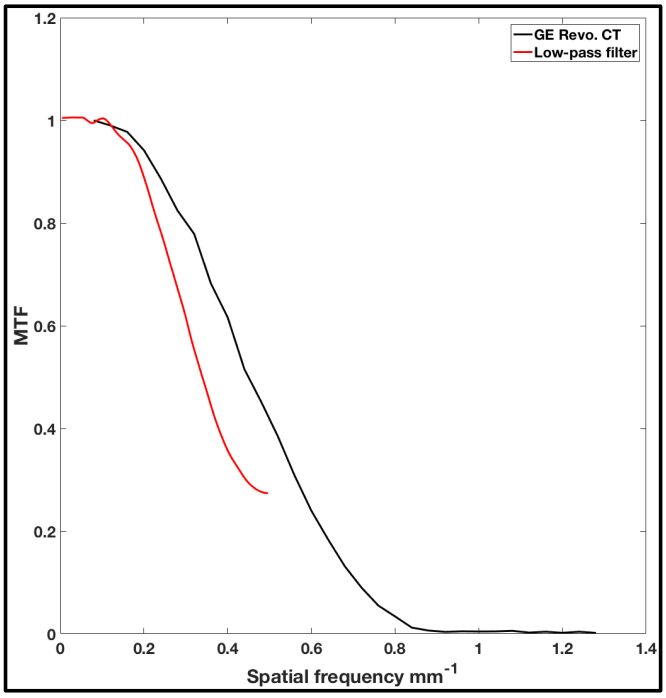

Figure A.3: Modulation transfer function (MTF) of the GE Revolution CT 'Standard' reconstruction kernel (black) and the low-pass mesh filter (red) applied on the analytically derived end systolic meshes.

A.3 Estimating confidence intervals for endocardial edge position

Noise was added to the (x, y, z) coordinates of the analytically derived end systolic meshes prior to application of the registration algorithm for the following two reasons:

1. to break the 'analytical coherence' of mesh features between end diastole and end systole
2. to simulate the natural variability in endocardial position due to CT noise

The level of added noise was chosen within the range of the root-mean-square variance in 3D endocardial position as determined from Sec. A.3.3.

A.3.1 Algorithm for Estimating Variability in Edge Location

If a stationary object was scanned in a CT scanner and independent images of the object were reconstructed with no view sharing, each reconstructed image would have independent noise, causing a degree of variability in the edge estimates. The method proposed to calculate the variability in edge location is outlined below:

1. obtain multiple images $N(> 10)$, each with independent noise
2. segment the object in each image
3. sum all segmented images of the object
4. calculate the number of pixels (voxels in 3D), T, in the transition range of the summed image (transition range defined by $[1, N-1]$)
5. detect the mean object from the summed image (defined by the object with pixel values $\geq \frac{N}{2}$)

6. calculate the perimeter (area in 3D) P of the edge of the mean object

7. edge variability $V = \frac{T}{P}$

The edge variability V is an estimate of the size of the uncertainty region within which the edge may be detected. It has the unit of length.

A.3.2 Validation of Algorithm Proposed in Sec. A.3.1

The proposed method outlined in Sec. A.3.1 was validated by simulating a square with a programmed region of uncertainty within which the edge maybe detected under the influence of noise. The programmed ground-truth uncertainty was compared with the estimate obtained from the algorithm outlined in Sec. A.3.1

From a clinical scan of a human LV (tube current: 530; kVp: 80 kV; gantry revolution time: 280 ms; reconstruction diameter: 200 mm; kernel: Standard; contrast agent: Visipaque 320 mg/ml, GE Healthcare, Chicago IL; contrast delivery: intravenous), an estimate of the gradient of the endocardial edge was determined for use in our simulation. The mean (μ) and standard deviation (σ) of HU within the contrast enhanced LV blood pool was measured to be 600 and 56 respectively and the user selected threshold for LV blood segmentation was set at 300 HU; thus 300–2σ = 188 defines the HU limit for a 95% certainty in classification of the contrast enhanced blood pool from the myocardium. By setting the appropriate window level (300 HU) and window width ($4\sigma = 224$ HU), it was observed that the HU transitioned from the blood pool to the myocardium over $\sim$2 mm for a 95% certainty in classification of each region. The edge gradient was spatially dependent; the gradient was more gradual near the papillary muscles and sharper at the base.

In an image of 512 x 512 pixels, a centrally located square object of side length 255 pixels

with a uniform pixel intensity of 580 was created. The background of the image had a uniform intensity of 100. The intensity values were chosen to simulate that of the blood contrast agent in the LV (580 HU) and the myocardium (100 HU). For our simulation, the edge gradient from the square object to the background was linearly defined over 5 pixels (2.5 mm at 0.5 mm in-plane pixel spacing); this enabled the edge gradient to be symmetric about a mean edge at a HU value of 340. The object (Fig. A.4A) and a zoomed in view of the edge (Fig. A.4B) are shown in Fig. A.4.

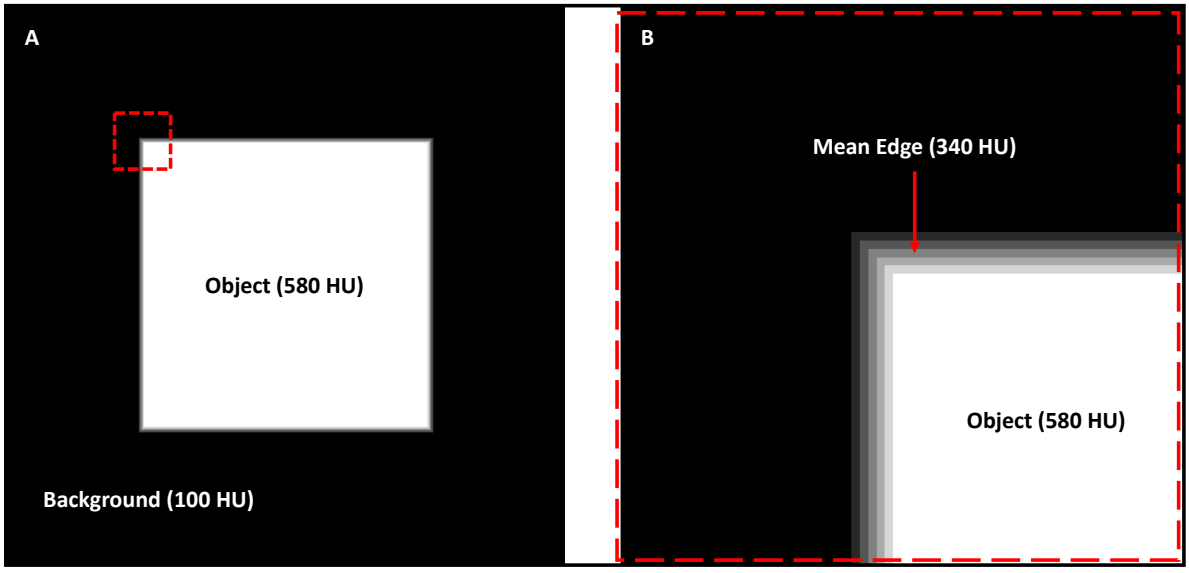

Figure A.4: Simulation of precision estimation in endocardial edge detection. (A) Image of 512 x 512 pixels with a background intensity of 100 units (to simulate the myocardium HU) and a centrally located square object of size 255 x 255 pixels having a uniform intensity of 580 units (to simulate the blood contrast agent HU in the LV). The edge of the square object is defined by a linear gradient in intensity from the background to the object, occurring over a length of 5 pixels. (B) Zoomed in view of the object's edge, corresponding to the dashed red box in (A), highlighting the gradient and the mean edge.

For a 95% certainty in classification of both the background and the square object, a uniform distribution of random noise in the range of $\pm 2\sigma(\pm 2 \times 56)$, as determined from the clinical scan mentioned above, was added across the entire 512 x 512 image. The process was

repeated 100 (N) times, yielding 100 images with independent noise and for each case, the square object was segmented by applying a threshold of 340 HU. For the above defined noise level and edge gradient, the programmed region of uncertainty in edge location was 3 pixels, and the measured estimate using the algorithm outlined in Sec. A.3.1 was 3.02 pixels.

As a second iteration of validation, with all other parameters kept constant, the edge gradient defining the transition in HU between the object and the background was changed to 11 pixels (5.5 mm at 0.5 mm in-plane pixel spacing), which was representative of the edge gradient near the papillary muscles in our sample clinical LV scan. Again, 100 instances of independent noise were added to the image and the square object was segmented in each case by applying a threshold of 340 HU. The programmed region of uncertainty in edge location was 5 pixels, and the measured estimate using our algorithm was 4.99 pixels. In both simulations performed above, the estimates of variability in edge location obtained from the algorithm outlined in Sec. A.3.1 were in good agreement with the programmed ground-truth region of uncertainty in edge location.

A.3.3 Precision Estimation of Edge Detection under Different Imaging Protocols

The end diastolic phase of a human LV endocardium derived from a clinical cardiac CT scan was 3D printed using a Formlabs 2 stereolithography printer (Formlabs Inc., Massachusetts) and the LV cavity was filled with an iodinated non-ionic radiocontrast agent (10% by volume solution of Visipaque 320, GE Healthcare, Chicago IL). The 3D printing material, which is a proprietary photopolymer resin (Formlabs Clear FLGPCL04), and the 10% iodinated contrast solution had HU values of 100 ± 9 and 502 ± 4 respectively. The printed phantom was imaged

under 50 mA (9 mAs), 200 mA (36 mAs), and 400 mA (73 mAs) x-ray tube current settings (100 kVp; small focal spot) and for each tube current setting, 14 3D volumes were acquired and reconstructed (reconstruction diameter: 200 mm; kernel: Standard) with no view sharing such that each image had independent noise. The signal to noise ratios within a region of the LV blood pool for the three x-ray tube currents were measured to be 7.7 ± 0.2, 10.3 ± 0.9, and 12 ± 1.3. Precision estimates of edge location were obtained for each tube current setting using the algorithm outlined in Sec. A.3.1.

Figure A.5 shows an axial slice of the phantom for each of the three tube current settings. The phantom was positioned in the scanner upright; hence, the axial views shown in Fig. A.5 do not correspond to traditional axial views of a clinical scan with the heart in its native orientation. The variability V in the location of the edge was estimated using the algorithm outlined in Sec. A.3.1 to be 1.65, 0.9, and 0.65 mm (3.3, 1.8, and 1.3 pixels) for the 50, 200, and 400 mA tube currents, respectively. Additionally, Fig. A.6 shows three regions of an axial slice of the summation image (image obtained by adding the 14 independent LV segmentations) for each tube current setting (regions correspond to the dashed red, blue, and yellow boxes in Fig. A.5). Line segments were drawn perpendicular to the endocardial surface that began at the high intensity region (pixel value = 14) and ended at the low intensity region (pixel value = 0), determined by visual inspection. The lengths of the line segments were used to quantify edge variability. These estimates agreed with the ones obtained using the algorithm outlined in Sec. A.3.1.

The level of noise added to our analytically displaced end systolic mesh points (x, y, z) prior to the registration process was calculated from the precision estimates obtained above. The variability V for each tube current setting was divided by 2 to obtain an estimate of the variation about a 'mean'. For example, for the 50 mA tube current setting, the edge had an uncertainty

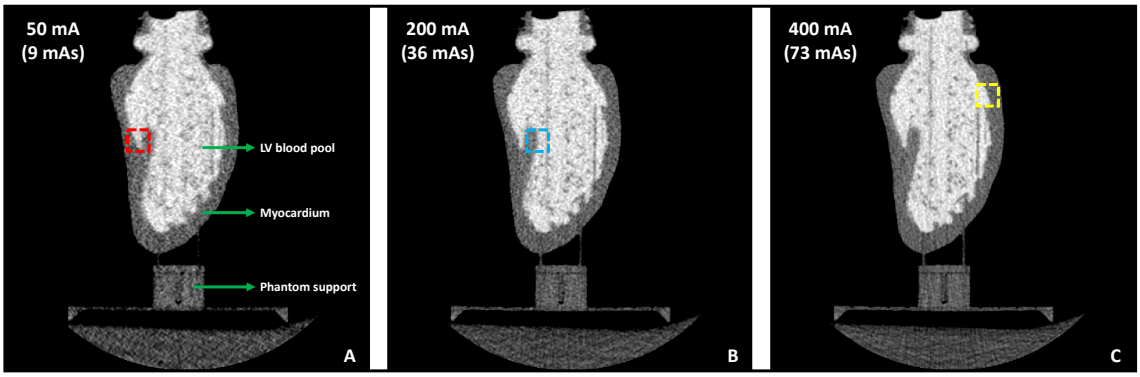

Figure A.5: Axial slices of a 3D printed end diastolic human LV phantom imaged under different tube current settings. (A) 50 mA. (B) 200 mA. (C) 400 mA. For each tube current setting, the peak voltage was set to 100 kVp with a small focal spot size. The phantom was positioned in the scanner upright, hence these axial slices do not correspond to the axial slices of a clinical scan with the heart in its native orientation The dashed red, blue, and yellow boxes highlight the regions shown in the dashed boxes of the corresponding colors in Fig. A.5

region of 1.65 mm; assuming the mean edge lies in the middle of this uncertainty region, the edge can be detected over a region of ± 0.83 mm. Similarly, for the 200 and 400 mA tube current settings, the regions of uncertainty were ± 0.45 mm and ± 0.33 mm, respectively. Therefore, a mean value of ± 0.6 mm was added as noise to the end systolic mesh points to simulate the uncertainty in endocardial edge location.

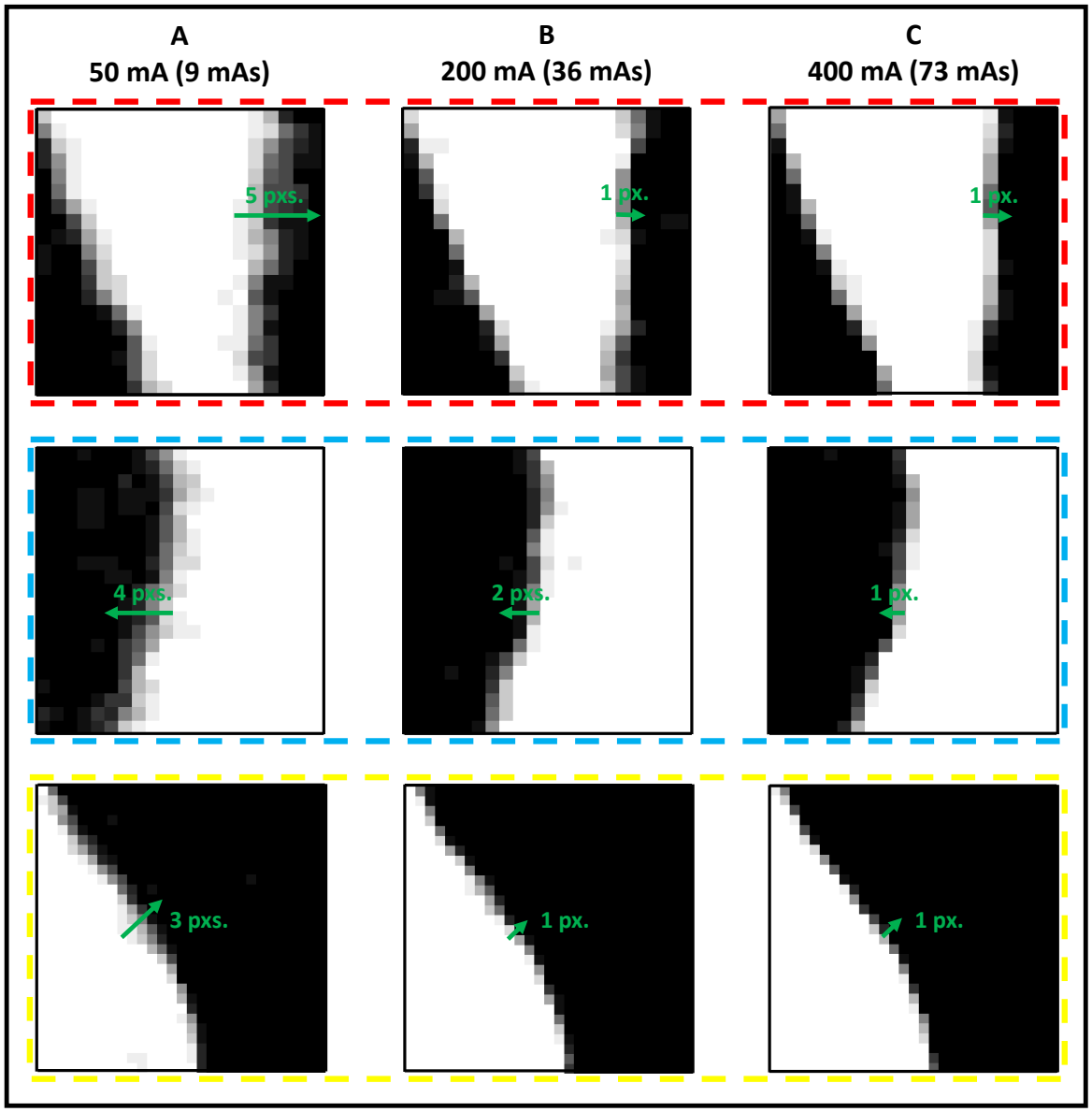

Figure A.6: Variability in endocardial edge location at three highlighted zones of the segmented LV for different tube current settings. (A) 50 mA. (B) 200 mA. (C) 400 mA. The location of each zone is shown by the dashed boxes of the corresponding colors in Fig. A.5. The images are of the summation volume obtained by adding the 14 independent segmentations of the LV blood pool for each tube current setting. White pixels are of intensity 14, black pixels are 0, and values in-between are represented by the various shades of gray. Line segments (in green) drawn perpendicular to the endocardial surface serve as visual aids for measuring the variability in edge locations.

A.4 References

1. Cruz-Bastida, J. P., Gomez-Cardona, D., Li, K., Sun, H., Hsieh, J., Szczykutowicz, T. P. & Chen, G.-H. Hi-Res scan mode in clinical MDCT systems: Experimental assessment of spatial resolution performance. *Medical Physics* **43,** 2399–2409. ISSN: 00942405. `http://doi.wiley.com/10.1118/1.4946816` (Apr. 2016).

Appendix B

Temporal resolution of estimating timing of LV mechanics with 4DCT - Supplementary Information

The generation of highly detailed anthropomorphically accurate 4DCT images with motion artifact using 3D printed models is one of the novel contributions of this manuscript. We demonstrate that "stop-motion" animation can be used to dramatically increases the space of anthropomorphic detailed shapes that can be tested with actual clinical scanners. Each "stop-motion" scan of the deformed phantom has independent noise and blurring associated with the particular instantiation of CT sampling and reconstruction. This is very difficult to simulate in detail without using proprietary information about the reconstruction algorithm and noise sources on the particular CT scanner. Synthesizing a sinogram from interpolation of discrete static phases enabled us to: 1) utilize the potential of 3D printing to create detailed highly accu-

rate models of the heart at different cardiac phases, and 2) simulate continuous cardiac motion from measured scanner raw data of the 3D printed phases. The synthesis of a dynamic sinogram from static phases helps overcomes some of the limitations of CT simulators and existing cardiac motion phantoms (e.g. Shelley dynamic cardiac phantom) with limited spatial features.

We performed computer simulations to demonstrate that the 26 phases used to synthesize a dynamic sinogram were sufficient to generate the expected wall motion artifacts seen clinically; these wall motion artifacts ("double-wall" and "stationary-wall") are the root cause for errors in the estimation of mechanical activation times of wall motion using 4DCT. The details of the simulation are provided below.

Stereolithography (STL) files containing triangular meshes of the dyssynchronous phantom that sampled the simulated cardiac cycle in both 26 (original sampling rate) and 260 phases (up sampled by a factor of 10) were created. CT projection data for these in-silico phantoms were generated using the Catsim simulation tool [1]. Dynamic sinograms were then synthesized from the projection data of the 26 and the 260 phases using view blending, as described in Chapter 3, Sec. 3.2.3. The synthesized dynamic sinogram derived from using 260 phases most closely represented a truly dynamic sinogram.

Images were reconstructed from these synthesized sinograms at a phase of the cardiac cycle with significant wall motion (217 ms; mid systole) and then compared with the image reconstructed from the static sinogram at the same phase. The first row of Fig. B.1 shows, from left to right, reconstructed images at 217 ms of the cardiac cycle derived from: the synthesized dynamic sinogram using 26 phases, the static sinogram, and the synthesized dynamic sinogram using 260 phases. The second row of Fig. B.1 shows difference images between the static image and the images derived from the sinograms synthesized using 26 and 260 phases, respectively.

The third row shows the difference between the images reconstructed from the 26 and the 260 phases derived sinograms. This figure highlights the small differences in the errors of endocardial boundary positions between the 26 and the 260 phases derived sinograms; these errors are extremely small compared to the "double-wall" and the "stationary-wall" artifacts which adversely affect the estimation of mechanical activation times in images with motion artifact.

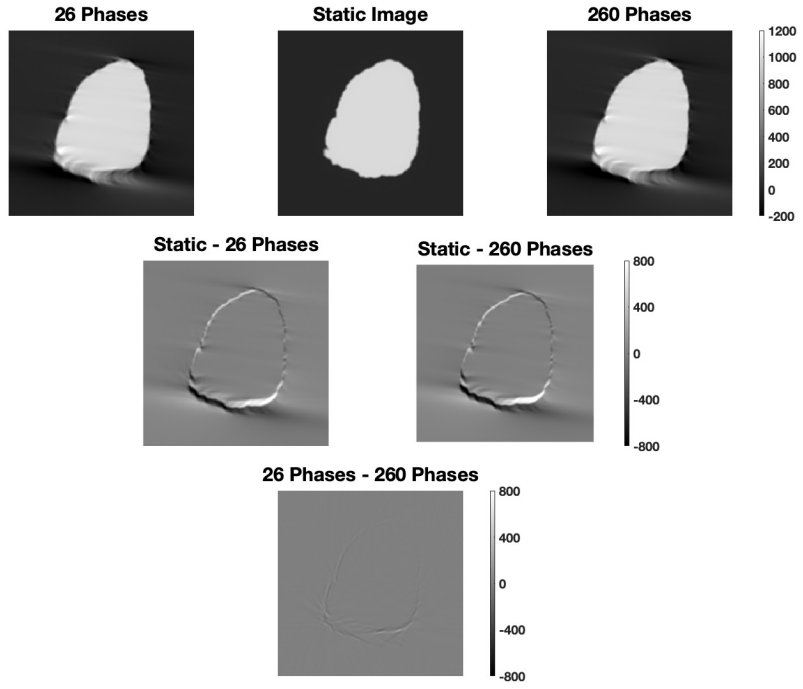

Figure B.1: (Top-row) Images reconstructed at 217 ms of the cardiac cycle from sinograms synthesized using 26 phases, the static 217 ms phase, and 260 phases from left to right, respectively. (Middle-row) Difference images between the static image and the 26 and the 260 phases derived images, respectively. (Bottom-row) Difference image between the 26 and the 260 phases derived images.

Figure B.2 plots line profiles of the endocardial boundary at the locations of the lateral wall (yellow line) and septal wall (green line) m-mode lines. The three line profiles are those derived from the images reconstructed using the 26 phases sinogram (dash-dotted black line), the 260 phases sinogram (dotted blue line), and the static sinogram (solid red). The Otsu threshold for edge detection is shown by the dashed horizontal line in magenta. Figure B.2

highlights the differences in edge location between images reconstructed from the 26 and the 260 phases sinograms. These differences, being imperceptibly small, do not affect the estimation of mechanical activation times; errors in the estimation of wall position are primarily due to larger "double-wall" and "stationary-wall" artifacts. Both the 26 phase model and the 260 phase model estimate this artifactual displacement correctly.

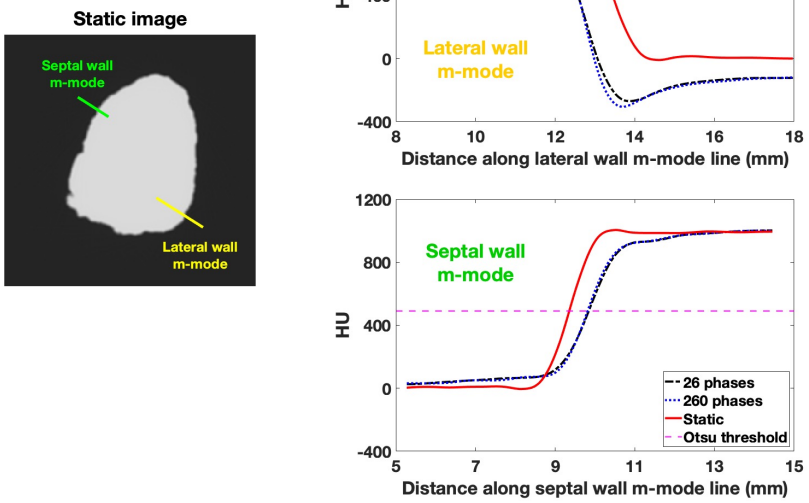

Figure B.2: (Central-left) Image reconstructed from the static sinogram, showing the lateral wall (yellow) and the septal wall (green) m-mode lines. (Top-right) Endocardial line profiles at the lateral wall m-mode location. (Bottom-right) Endocardial line profiles at the septal wall m-mode location. The three line profiles are derived from images reconstructed using the 26 (dash-dotted black line), the static (solid red), and the 260 phases sinograms (dotted blue). The horizontal dashed magenta line represents the optimal threshold for blood-volume segmentation as determined using Otsu's method.

B.1 References

1. De Man, B., Basu, S., Chandra, N., Dunham, B., Edic, P., Iatrou, M., McOlash, S., Sainath, P., Shaughnessy, C., Tower, B. & Williams, E. *CatSim: a new computer assisted tomography simulation environment* in *Medical Imaging 2007: Physics of Medical Imaging* (eds Hsieh, J. & Flynn, M. J.) **6510** (Mar. 2007), 65102G. ISBN: 081946628X. `http://proceedings.spiedigitallibrary.org/proceeding.aspx?doi=10.1117/12.710713`.

Appendix C

Prediction of CRT response using a lead placement score defined using 4DCT-derived features of LV mechanics - Supplementary Information

We performed a multivariable analysis including many clinical predictors of CRT response as a reference to compare the performance of the 4DCT-defined LPS model. The clinical features included were:

- QRS durartion

- Hemoglobin concentration
- Mid-RV diameter measured with echocardiography
- Tricuspid annular plane systolic excursion
- Sex
- Presence of ischemic cardiomyopathy
- Presence of prior myocardial infarction
- Presence of coronary artery bypass graft
- Presence of atrial fibrillation

These features were used to train and define an independent SVM model for CRT response prediction in a manner similar to that outlined in Chapter 4, Sec. 4.2.6; we refer to this model as the 'clinical' model. Additionally, another SVM model was independently trained and defined using both the set of clinical features listed above as well as the set of 4DCT-derived features of LV mechanics; we refer to this model as the 'clinical + 4DCT' model. The performances of the above two models were then compared with the performance of the LPS model defined using just the 4DCT-derived features of LV mechanics, referred to as the '4DCT' model.

Figure C.1 shows the ROC curves for the three models. The AUCs of the models were 78%, 87%, and 89% for the clinical, 4DCT, and clinical + 4DCT models, respectively. The addition of clinical features improved the performance of the 4DCT model by 2% AUC, whereas the addition of 4DCT-derived features improved the performance of the clinical model by 11% AUC.

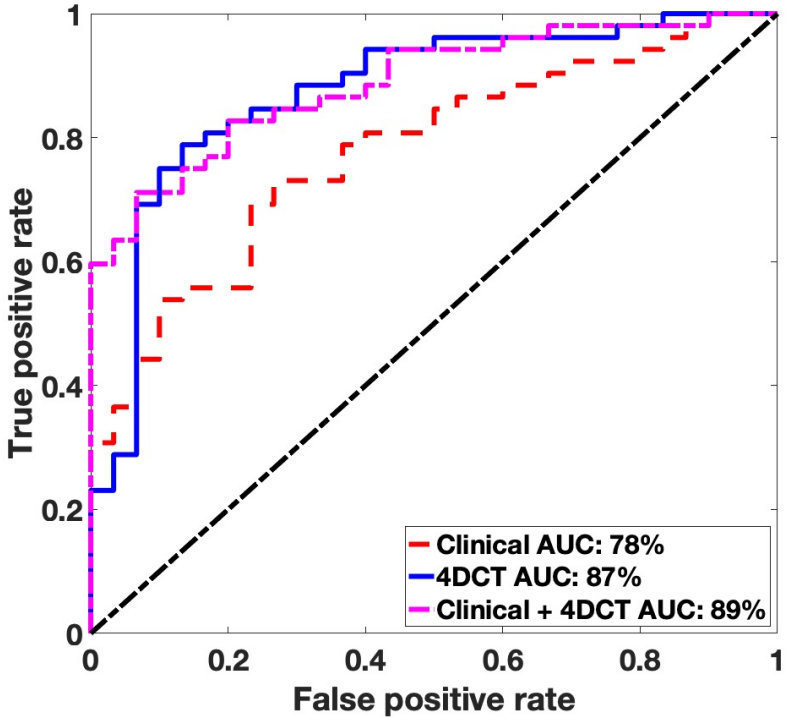

Figure C.1: ROC curves for three different CRT response prediction models using: 1) only clinical features (dashed red), 2) only 4DCT-derived features (solid blue), and 3) both 4DCT and clinical features together (doted magenta).